Department of Applied Physics

University of Granada

Doctoral Thesis

Nanoparticle deposits formed at driven contact lines

Authoress:
Carmen Lucía
Moraila-Martínez

Supervisors:
Dr. Miguel A.
Cabrerizo-Vílchez
Dr. Miguel A.
Rodríguez-Valverde

July 2, 2012

Editor: Editorial de la Universidad de Granada
Autor: Carmen Lucía Moraila Martínez
D.L.: GR 374-2013
ISBN: 978-84-9028-331-8

Contents

Acknowledgments

This work was supported by the "Ministerio Español de Ciencia e Innovación" (project MAT2011-23339) and the "Junta de Andalucía" (projects P07-FQM-02517, P08-FQM-4325 and P09-FQM-4698). We thank to Javier Montes, Miguel A. Fernndez, Yadira Snchez and Jos Antonio Martn for the help and support during the experimental work. Also, we are very grateful to Dr. Juan Antonio Holgado-Terriza, programmer of the software Contacto© and Dinaten© used for contact angle measurements.

Motivation

Drying of colloidal suspensions appears in many applications such as coatings (paints, ink printing, paving)(1), colloidal assembly/templating (2), discrimination of particles with different size (3) even medical diagnostics (4). *Complex* liquids, namely suspensions of solid particles, polymeric dispersions, emulsions.., and *simple* liquids behave in different way at interfacial regions. The formation of stains at the periphery of drying drops of any colloidal dispersion (see Figure 1) is known as the "coffee stain effect" or "coffee ring effect" (5–7). This effect is daily observed: dishwasher stains on drinking glasses, red wine stains on textiles... Currently, the study of deposits formation with mesoscopic particle suspensions upon drying conditions is an emerging topic with 1409 articles indexed in Web of Science (source: WoK) and 118000 results in Google.

Controlling the distribution of solute during drying is vital in many industrial and scientific processes. For example, paint manufacturers use a variety of additives to ensure that the pigment is evenly dispersed and remains so during drying (8). Spreading and drying of ink droplets ejected from nozzles onto substrates is crucial for the inkjet deposition technologies (9, 10). For research purposes, drying of drops is also used to deposit uniformly biological entities onto a substrate such as bacteria (11, 12) or DNA molecules (13, 14). Segregation effects are undesirable in all these cases. Otherwise, the "coffee ring effect" can be also fruitful.

After drying of pure water drops, the observation of short-lived nanoscopic structures on surfaces exposed to air usually reveals the surface uncleanness due to adventitious substances (15, 16). An innovative approach for medical diagnostics is based on the comparison of the patterns of dried drops of biological liquids of people with different diseases (17–19) with regard

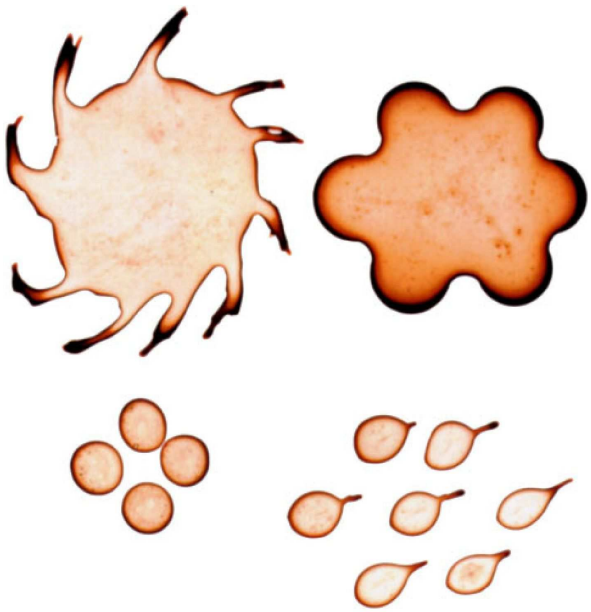

Figure 1: Stains left by drying drops of coffee. It is worth to highlight how the stains are much darker at highly curved regions.

to people in healthy conditions. However, this strategy has drawbacks such as the subjective estimate of the patterns and the difficult standardization of experiments (Figure 2).

Micrometer- to millimeter-sized 2-D and 3-D arrays of colloidal particles can be fabricated by capillary flow- and evaporative flux-driven assembly on patterned surfaces (20–23). The drying of a sessile drop of a colloidal suspension on a surface is a simple nanoassembly strategy. As the drop dries, the triple line serves as a template and directs the formation of the resulting colloidal crystal (24). However, the control of the features of the colloidal crystal formed inside drying drops can be quite difficult (25–29).

Several authors have proposed different strategies for inhibition of "coffee stain effect", i.e. the formation of central spots or uniform deposits, based on Marangoni flow (30, 31), particle aspect ratio (32), electrowetting (33), capillary force near the contact line (34), pinning-depinning events at the contact line (35) and low frequency vibration (36). The transition from ring-like to uniform deposits is also likely influenced by particle surface changes, surface roughness, particle wettabillity... Recently, Bhardwaj et al. (37) reported that the pH of the solution of the drop also influence the final deposit pattern. The transition between different patterns is explained by considering how the electrostatic and van der Waals forces modify the particle deposition process.

Desiccation of colloidal suspensions is governed by the coupling between hydrodynamics, heat and mass transfer and wetting. It is not always clear what the mechanisms of formation for the different deposits are. Besides, although the time scale of the process is extremely long,

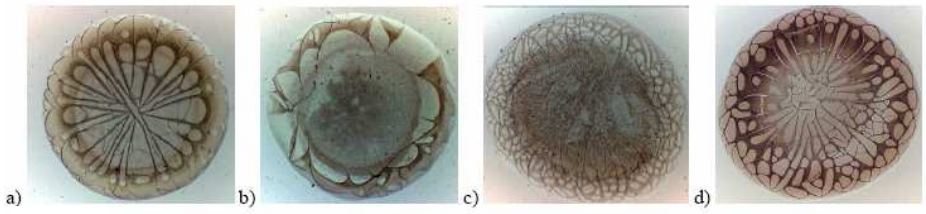

Figure 2: Dried drops of blood serum: a) Practically healthy person. b), c), d) Persons with different kinds of diseases.

it is not clear how to treat such a nonequilibrium situation. A better understanding of the driving mechanisms of the drying of colloidal suspension drops would improve the productivity and competitiveness of the concerning industries.

In order to produce well-ordered structures via evaporation, it is essential to control the evaporation flux, solute concentration, interaction between the solute and the substrate, etc (38). The reproducibility of experiments with evaporating sessile drops on substrates, even using pure liquids, is very poor. Rate of liquid loss during drop evaporation strongly depends on the experiment conditions (drop volume, temperature, humidity). Further, an evaporating drop can remain static or very slowly recedes on the solid surface. Due to the long-time scale dynamics, the evaporating drop may be trapped at the first local energy minimum that is encountered due to contact angle hysteresis of the substrate. The obscure contact line dynamics, the competition of inwards and outwards flows within the drop and the increasing concentration of particles in the bulk may hinder the actual mechanisms that lead or mitigate the ring formation. For this reason, the analysis of dried drops of colloidal suspensions is typically performed only after the complete drying.

Colloidal patterning using drying colloidal suspensions is greatly ruled by contact line dynamics. For instance, the mechanism of colloidal self-assembly and the coating quality (homogeneity, thickness) produced with the dip-coating technique[a] turn out to vary strongly depending on the dynamics of receding contact lines (see Figure 3). This may become very critical in industrial applications such as immersion lithography (39, 40).

In this work, we propose standardize the contact line dynamics of sessile drops upon evaporation-like conditions but without any significant convective flows within the drop. This way, special attention was addressed to receding contact lines. As reported in literature, driven contact lines also enable the formation of particle deposits (41–44). Our methodology allows examining separately the impact of contact line dynamics and the properties of the nanoparticle suspensions

[a] Dip coating is widely used in many industrial processes to deposit thin films on substrates. In the dip coating technique, a substrate is dipped into a liquid solution and next, it is withdrawn from the solution at a controlled speed.

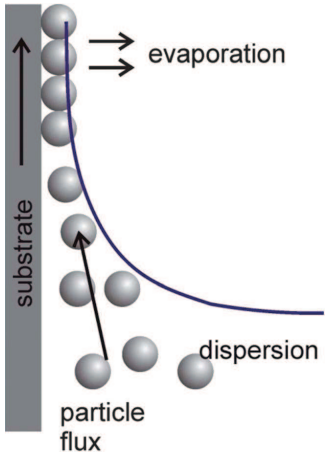

Figure 3: Vertical deposition of particles by evaporation and by vertically lifting of the substrate.

(bulk concentration, surface electric charge, wettability). We probed the arrangement of nanoparticles at driven contact lines, with low capillary numbers and at time scales shorter than during evaporation. Unlike typical commercial curtain coating, we operated in the quasi-static regime of contact line motion where the viscous effects are excluded ($Ca \ll 10^{-4}$). In this scenario, the observed contact angle was speed-independent.

The present dissertation is essentially arranged in two parts in order to explore separately the behaviour of receding contact lines with pure liquids (part I) and complex liquids (part II), namely nanoparticle aqueous suspensions. With a variable rate of withdrawal of liquid, we controlled the dynamics of receding contact lines of millimeter-sized drops ($\sim 100\mu$l). Following this approach, we were able to emulate the first stages of drop evaporation, but at shorter times. We monitored the contact line dynamics of shrinking drops containing nanoparticles to identify stick-slip events. We analyzed the effect of several parameters such as wettability contrast between particle and substrate, particle concentration, particle size and electrostatic interactions (particle-particle and substrate-particle) on the formation and morphology of the nanoparticle ring-like deposits. Special attention was addressed to the effect of pinning time on the formation of particle deposits. As far as we know, this is the first work devoted to study the role of the particle-particle and substrate-particle interactions on the deposits formation without macroscopic evaporation.

Part I

Receding contact lines of pure liquids

CHAPTER 1

Theoretical framework

Receding contact lines of pure liquids

1.1 Wetting

A liquid drop spreads on a solid surface up to cover a particular area, in prejudice of the surrounding liquid vapour, driven by the solid-liquid intermolecular interactions (see Figure 1.1). This interfacial phenomenon is known as *wetting* and the affinity of a solid surface to be wetted by a given liquid is referred to as *wettability* (45, 46). Currently, wetting is ubiquitous in many emerging disciplines such as self-cleaning surfaces, microfluidics, micro- and nanoelectromechanical systems, etc.

Just observing Nature, we find that liquids do not wet equally all solids. Wettability of a solid-liquid-vapour system can be quantified from the *contact angle*, which is defined as the angle formed between the tangent unit to the liquid-vapour interface and the tangent to the solid-liquid interface at the three-phase contact line (see Figure 1.2). Marmur (47) suggested to use the terms *hygrophilic* and *hygrophobic* (from the Greek prefix hygro- that means liquid) to describe in general low-contact angle and high-contact angle surfaces. These terms can prevent the need for using

multiple adjectives such as hydrophilic/oleophilic/lyophilic or hydrophobic/oleophobic/lyophobic. We highly recommend the reading of the book chapter "On the Origins of Water Wetting Terminology" (48) where Vogler documents the history of the use of the terms hydrophilic and hydrophobic and stresses how their idiomatic use has been destructive.

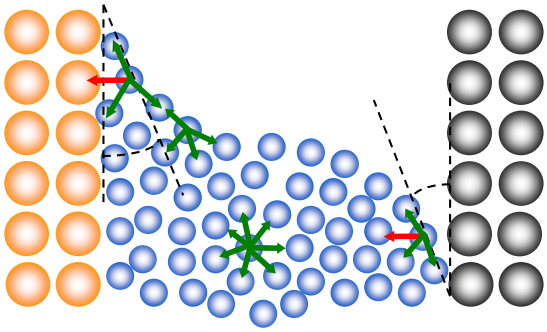

Figure 1.1: Cohesion and adhesion forces. The green arrows represent the intermolecular forces due to the liquid cohesion and the red arrows are the forces originated by the solid-liquid adhesion. For sake of simplification, the forces of the vapour molecules are assumed negligible.

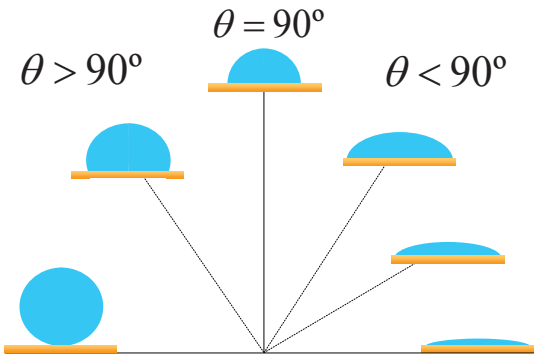

Figure 1.2: Concept of wettability and its interpretation in terms of contact angle.

1.1.1 Young equation

The mechanical equilibrium condition of a solid-liquid-vapour system (49), i.e. the balance of interfacial forces[a], is:

$$\cos\theta = \frac{\gamma_{SV} - \gamma_{SL}}{\gamma_{LV}} \tag{1.1}$$

where γ_{SV}, γ_{SL} and γ_{LV} are the concerning interfacial tensions at each interface (solid-vapour, solid-liquid and liquid-vapour, respectively) and θ is the contact angle of a stable configuration

[a] Actually, it is the balance of the horizontal components of the interfacial forces

of the system (Figure 1.3). The condition (1.1), incorrectly referred to as the Young equation[b], is locally fulfilled provided that the three-phase or triple contact line is free to move, without constraints.

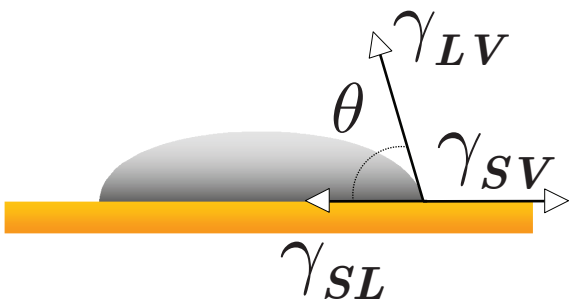

Figure 1.3: Contact angle and interfacial tensions of a sessile drop placed on a solid surface.

The thermodynamic equilibrium[c] condition or the Young equation of a solid-liquid-vapour system, i.e. the (local) minimum[d] energy condition, is:

$$\cos\theta_Y = \frac{\sigma_{SV} - \sigma_{SL}}{\sigma_{LV}} \tag{1.2}$$

where $\sigma_{\alpha\beta}$ are the concerning specific interfacial energies associated to each interface ($\alpha\beta = LV, SL, SV$) and θ_Y is the *Young contact angle* (Figure 1.4). If the Young-Laplace equation[e] describes the shape of the liquid-vapour interface (49), the Young equation rises as its "natural" boundary condition due to the solid phase contact.

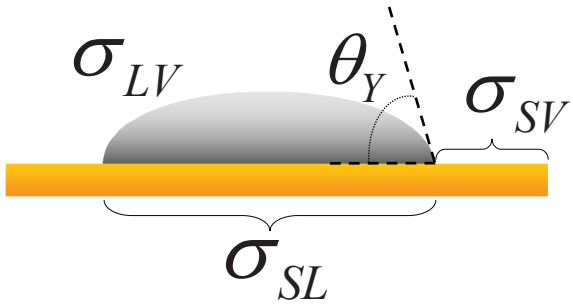

Figure 1.4: Young contact angle and interfacial energies of a sessile drop placed on a solid surface.

[b] Although Thomas Young originally formulated his famous equation from mechanistic arguments (50)

[c] Mechanical, chemical and thermal equilibria

[d] In fact, the Young equation arises from the extreme condition of the free energy

[e] The Young−Laplace equation is indistinctly interpreted either as the mechanical or thermodynamic equilibrium condition for most liquid−fluid interfaces (isotropic phases) due to the fast molecules diffusion between phases (i.e. chemical equilibrium)

A solid-liquid-vapour system can be mechanically stable but far from the thermodynamic equilibrium because of the absence of diffusion equilibrium at common solid-liquid interfaces (51, 52). Both thermodynamic and mechanical equilibrium conditions (1.1-1.2) will coincide just on an *ideal* solid surface: smooth, chemically homogeneous, chemically inert and rigid surface; where the solid interfacial tensions numerically coincide with the respective specific interfacial energies. Hence, on moderately rigid solids and at experimental time scales, a mechanical equilibrium configuration is usually realized at the three-phase line rather than a global thermodynamic equilibrium state (53). However, microscopic and molecular-scale deformations can occur on the solid surface to relax the unresolved vertical component of the liquid-vapour interfacial tension. Thermodynamic equilibrium state will be truly attained when the whole solid-liquid interface is accordingly deformed, as the Young modulus of the material, at very long times (even billions of year!). This sceneario illustrates the well-known creeping flow of the matter[f]. In conclusion, though the Young contact angle is conceptually accessible, it is experimentally inaccessible. Thus, the contact angle obtained experimentally is denominated *observable contact angle* and is a macroscopic angle[g].

The determination of the Young contact angle, θ_Y, i.e. the thermodynamic equilibrium contact angle of an ideal solid surface, is important for the characterization of solid-liquid interfacial systems (surface energetics). The Young contact angle is closely related to the concerning specific interfacial energies (material properties) through the Young equation (1.2). But, as above pointed out, the Young angle is experimentally inaccessible and besides, the observable contact angle can take multiple values due to the non-ideal features of nearly all solid surfaces (55, 56).

Surfaces of most practical materials are chemically heterogeneous (different functional groups, contaminations, mixtures of different solids, etc) and rough (texture, asperities, etc). These properties produce variability in contact angle, such as *contact angle multiplicity* (57) and *contact angle hysteresis* (58). Even on well-prepared solid surfaces, variability in contact angle is the norm, not the exception[h]. Thus, the experimental reproducibility of contact angle becomes difficult. There are many methods that have been developed to measure contact angles. However, there is still a controversy about the reliability and the reproducibility of the observable contact angles. For example, measurements reported from independent laboratories using different methods, for the same solid-liquid system, indicate a discrepancy of about 5° (59). Given the large differences found among measurement methods, it is important to report contact angle data always together with its detailed measurement method.

[f] "Everything flows, nothing stands still"- Heracletus (BC 500-440)(54). In fact, any solid surface evolves in time during wetting through chemical reactions, molecular rearrangement or elastic responses. According to the response time, measuring time-scale will determine the inertness and stiffness of solid surface in practical terms.

[g] Typically, the Rayleigh criterium limits the resolution of optical imaging systems to approximately half the wavelength of light (5.5–7.5μm)

[h] "God made the bulk; surfaces were invented by the devil"-Wolfgang Pauli (April 25, 1900 - December 15, 1958)

1.1.2 Contact angle hysteresis

The *configuration* (contact radius and observable contact angle) that adopts a sessile drop on a real surface depends on the way of its formation/deposition. When the observable contact angle is a function of the previous history (see Figure 1.5), then Contact Angle Hysteresis (CAH) occurs (60–62). While the relationship between surface tensions and the contact angle was established by Thomas Young in 1805, the existence of contact angle hysteresis was firstly reported by Lord Rayleigh in 1890 (Philosophical Magazine, xxx. pp. 285 298, 456 475, 1890). However, his observations remained almost unnoticed.

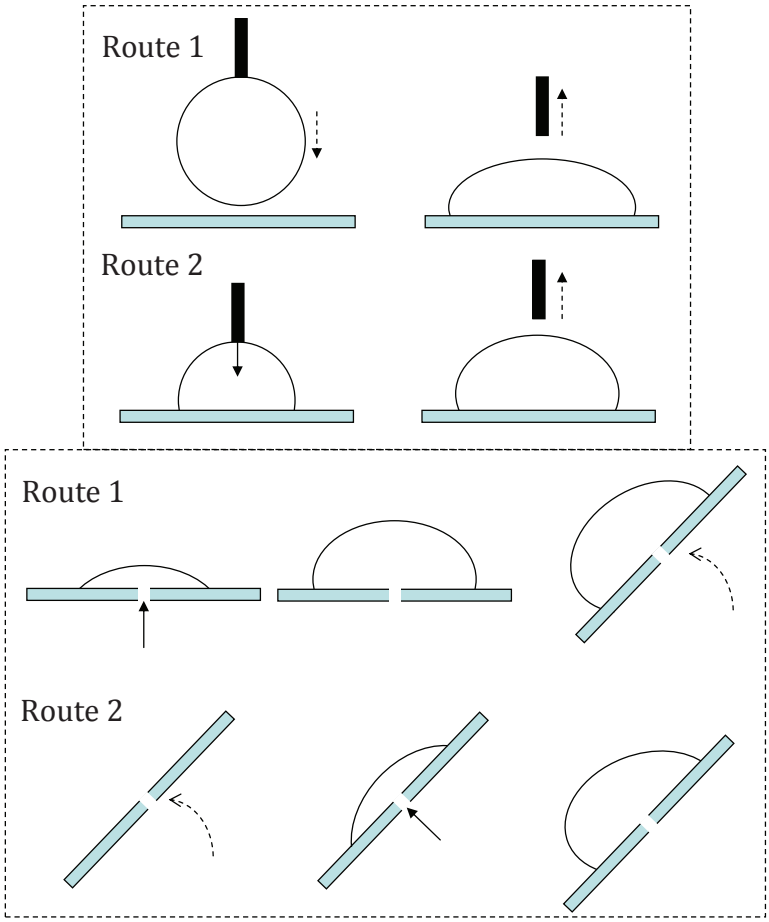

Figure 1.5: Dependence of contact angle on the drop formation/placement.

Time delays, such as those that happen in viscoelastic materials, or mechanical instabilities due to adhesion (see Appendix A) can induce CAH. The presence of topographic and/or chemical defects on solid surfaces is assumed to be the most probable origin of CAH (63–65), although this assumption should be verified for each system. Heterogeneity and roughness do not cause CAH in every case. Infinitely long stripes or asperities, that are oriented normal to the contact line,

do not induce CAH (57). There is no macroscopic hysteresis when the characteristic dimensions of heterogeneity or roughness features fall below about 0.1 μm (66, 67). Further, CAH can occur due to the kinetics of the solid-liquid interaction such as sorption of liquid by the solid, liquid penetration into the solid, retention of liquid molecules on the solid surface and surface reorganization. Anyhow, CAH is an indicator of the imperfection degree of the substrates and it is a characteristic of all materials used in surface engineering. Attempts to understand CAH phenomena began many years ago (60, 62, 68–70), although it is not fully understood yet.

A typical free energy curve of a solid-liquid-vapour system, where the surface is smooth but chemically heterogeneous, is shown in Figure 1.6. Instead of a unique energy minimum, there are multiple local minima, which are referred to as metastable equilibrium configurations or *metastates* (71, 72). The system can occupy one of several local energy minima and its history determines the minimum actually occupied. In a metastable configuration, there is a balance between the forces acting on the system, but this does not mean that the system is in complete thermodynamic equilibrium. Metastability means that the condition of minimum energy can be fulfilled locally for several configurations, although the true thermodynamic equilibrium configuration corresponds to the global energy minimum or most-stable configuration (see Figure 1.7). The Young equation (1.2) is necessary condition for the global equilibrium, but it is not sufficient condition. This means that the Young equation is associated to whatever metastate of a solid-liquid-vapour system (local minima), aside from to the global equilibrium configuration (global minimum). A drop remains in a metastable configuration if it does not possess the energy (thermal fluctuations, vibrational energy...)(55) needed for overcoming the barrier between the state and the next one. This barrier represents a local maximum energy and it is referred to as unstable equilibrium configuration because the drop is susceptible to fall into lower-energy states with only slight interaction.

For a given solid-liquid-vapour system and a fixed volume, three distinctive metastates (observable angles) can be identified in the free energy curve (Figure 1.6). The thermodynamically meaningful contact angle, associated to the global minimum energy, is θ_{eq} the equilibrium contact angle. Further, there are two other phenomenological angles of great importance due to their reproducibility: the maximum contact angle symbolized as θ_a (advancing contact angle), and the minimum contact angle, θ_r (receding contact angle). The difference $\theta_a - \theta_r$ measures the range of CAH. The advancing contact angle provides information about the most hygrophobic domain of the substrate and the receding contact angle, the most hygrophilic domain. Measurements of θ_a and θ_r are accomplished from the *incipient* relative movement of advancing and receding contact lines, respectively (73–75).

The most stable contact angle or equilibrium contact angle is determined by the balance of interfacial forces along the entire contact line (or else by the global minimization of free energy) from among all attainable configurations (triple lines) of a given thermodynamic state. Consequently, this angle is an observable quantity closely related to solid interfacial tensions (intensive

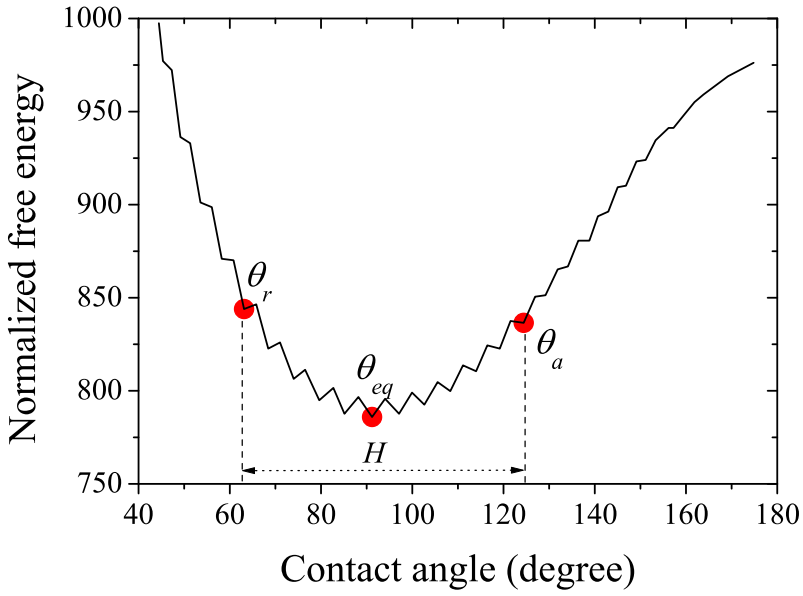

Figure 1.6: Dimensionless free energy on function of the observable contact angle for a fixed drop volume. It should be notice that the number of metastates is a function of the volume; more specifically, there exist more metastates for larger volumes (60).

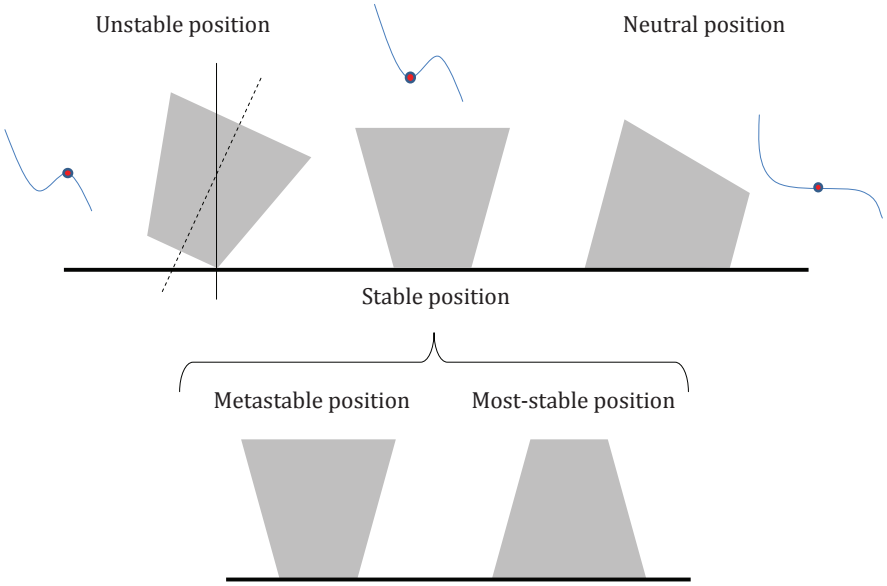

Figure 1.7: Illustration of the concepts of unstable, stable, metastable and most-stable configurations using the mechanical stability of a truncated cone.

properties) although it usually further depends on the system size (extensive property). Otherwise, unless very particular conditions, the equilibrium contact angle is hardly experimentally accessible (76, 77). Equilibrium contact angle becomes an effective, unlocated angle but associated univocally to the concerning thermodynamic state.

1.1.3 Receding contact angle

Advancing contact angles are usually employed to evaluate solid surface energies (45, 78). However, Cwikel et al. (79) reported significant differences in the value of surface energy as the contact angle used. A wide number of publications (80–84) have emphasized the significance of the receding contact angles in characterizing the interaction between the liquid and the solid phases. For instance, an evaporating sessile drop begins to move back when the receding contact angle is just reached (80). In superhydrophobic surfaces, the geometry of the posts determines the receding contact angle at which the drop starts to move and hence, the depinning transition is primarily controlled by the receding contact line (81, 82). In coating industry, the adhesion work is the work per unit of area that should be made on a solid-liquid system to detach the liquid from the solid surface (83). Hence, the effectiveness of a protective agent on a certain smooth substrate is better understood by considering the receding contact angle rather than the advancing contact angle (84).

When the observable contact angle is a function of the previous history of system, then contact angle hysteresis occurs (see Figure 1.5). Owing to contact angle hysteresis, contact angle strongly depends on the measuring conditions (55, 74, 85): technique, solid surface quality, liquid purity, size and creation of the liquid-vapor interface. We are able to control the quality of the solid sample and the liquid, the drop volume, but the drop formation should be also standardized if we intend to compare meaningful values of contact angle. For instance, drop evaporation dramatically depends on the dispensation of liquid (80, 86). Moreover, the pressure applied to a drop in the dispensing step can have significant impact on the contact angle results of superhydrophobic surfaces (87). It is well known that a sessile drop carefully placed with a handheld pipette can result in a contact angle somewhere between advancing and receding (79). The contact angle that a sessile drop adopts as a result of its placement on a surface can be quite different as the way to form the drop (handheld placed drop, captive sessile drop, drop formed from below the surface, etc.) due to contact angle hysteresis (88, 89). These disparities are particularly significant for receding contact angles (74, 75).

It is widely accepted that advancing contact angle and receding contact angle are the observable (macroscopic) angles at incipiently moving contact lines. But, the observation of the incipient motion of contact lines may be very complicated. Hence, advancing and receding angles are often measured at moving contact lines, i.e. they are actually *dynamic* contact angles

(85). However, dynamics of the contact line can dictate, at some extent, the measured values of contact angle (90). Low-rate dynamic contact angle measurement (91) is a well-established method to probe the wetting behavior of solid surfaces from the quasi-static motion of steadily growing/shrinking drops. From our long-standing experience in low-rate dynamic contact angle experiments, we observed that, unlike the advancing contact angle, the receding contact angle on different solid surfaces was apparently zero or decreased continuously as the drop volume was reduced. Due to the different density of metastates on the free-energy curve (see Figure 1.6), advancing drops usually attain a well-defined metastable configuration whereas receding drops can attain one of many metastable configurations separated by small energy barriers (92). For this reason, receding contact angle is especially difficult to reproduce experimentally because it is very susceptible to ambient vibrations (55, 92) and besides, it is limited by the initial drop volume.

Surface restructuring could explain the CAH found in smooth and rigid polymer surfaces (93). Moving a liquid drop interface over a previously wetted surface (receding) as opposed to a previously dry surface (advancing) could induce molecular rearrangement of the functional groups on the solid surface (94). In these cases, receding contact angles are usually caused by physical processes such as sorption of liquid by the solid, liquid penetration into the solid, retention of liquid molecules on the solid surface, and reorganization of polymer chains due to contact with a liquid (see Figure 1.8). Due to such processes, the polymer film becomes less hydrophobic than the original polymer surface. In this case, receding angle represents a solid with changed energetics. But, this hydrophilisation is not permanent because, after the drop removal on the surface, the hydrophilic groups are still mobile and they tend to move into the polymer which becomes hydrophobic again (i.e. the surface is able to recover its initial state).

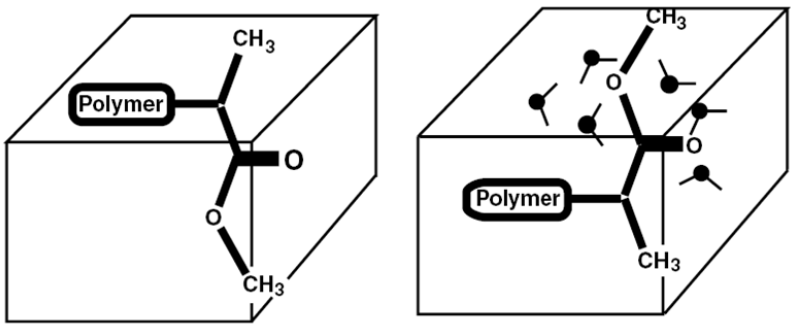

Figure 1.8: Surface groups oriented at the surface of a polymer can reorient in response to changes in the local environment to minimize the free energy at the interface.

In practice, the receding contact angle is apparently zero when the contact line does not retract macroscopically (as we can see in Figure 2.2). This can be limited by typical optical resolution. Furthermore, small contact angles (below 20°) do not enable an accurate determination with sessile drop. But if the initial volume of drop is not enough to reproduce the receding mode, then

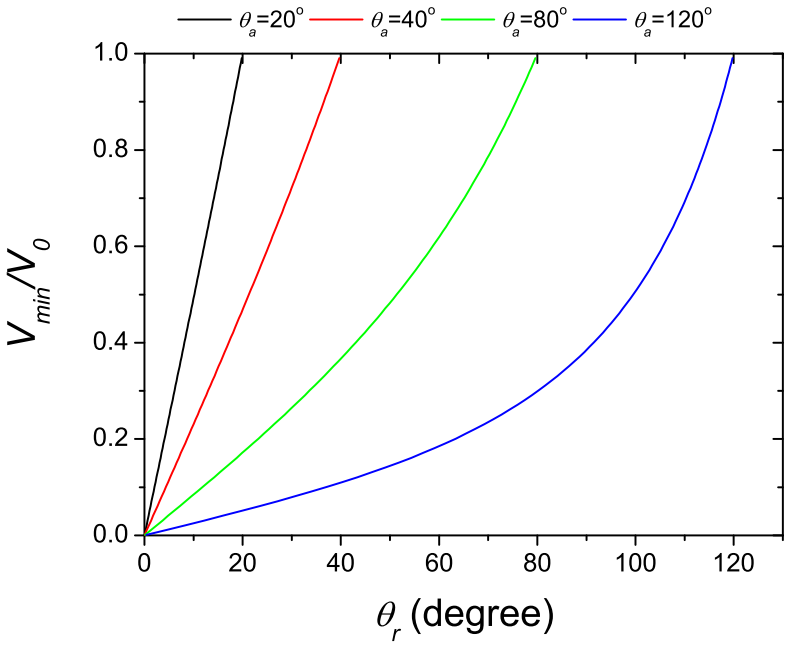

Figure 1.9: Minimum volume of a spherical drop, normalized by the initial volume, as function of the receding contact angle for different values of advancing angle.

the receding contact angle will be apparently zero as well.

Let be a spherical drop with a volume V_0 and a contact angle θ_a. This drop needs a minimum volume V_{min} to reach the receding angle θ_r:

$$\frac{V_{min}}{V_0} = \frac{8 - 9\cos\theta_r + \cos(3\theta_r)}{8 - 9\cos\theta_a + \cos(3\theta_a)} \frac{\sin^3\theta_a}{\sin^3\theta_r} \tag{1.3}$$

This is illustrated in Figure 1.9. Greater difference $\theta_a - \theta_r$, lower value of V_{min}. This trend is magnified for large values of θ_a. For this reason, we will employ large drops in our experiments. Moreover, it is well known that the large drops are most susceptible to ambient vibrations, which tend to relax the drops towards different configurations due to the small relative height of the energy barriers separating them (see Figure 1.6).

1.1.4 Contact line dynamics

Spontaneous motion of sessile drop (i.e. spreading) is solely dictated by the energy difference between a given non-equilibrium configuration and a final statically stable configuration. Unfortunately, setting a partially wetting drop in motion requires non-negligible forces because the contact angle hysteresis generates a force opposing the motion.

Forced motion

Applying an external driving force is usually a convenient way to probe the physics for non ideal surfaces and it is sometimes the only possible way to investigate them when more direct methods are not available. Unlike spontaneous wetting, *forced wetting* allows mapping on purpose certain configurations of the system. Forced wetting can be accomplished by dipping/rising vertically the solid in/from the liquid, tilting the solid surface or changing the drop volume by direct liquid addition/withdrawal (73–75). All these experimental approaches intentionally produce a "slow" variation in the solid-liquid area (wetted area) through the relative movement of contact line, driven by vertical push/pull forces, gravity or volume variations, accordingly.

If a sessile drop is slowly forced to advance or recede on the surface, the drop reacts like a spring in order to *reach* the new equilibrium state[i]. Dissipation can occurs either at the contact line (due to CAH) and/or in the bulk (viscous dissipation). Upon hydrodynamic conditions, the observable contact angle is known as *dynamic* contact angle because it changes as a function of contact line velocity (inertia regime). Further, the opposing viscous force increases as the speed. An advancing contact line persists to arbitrarily high speeds but a receding contact line vanishes at a critical speed set by the competition between viscous and surface tension forces.

In forced wetting, capillary force attempts to reduce the wetted area of the drop but has to work against the inertia and viscosity of the liquid. Capillary forces dominate over shear and inertial forces when the velocities of moving contact lines are considerably low. The Capillary Number is defined as:

$$Ca = \frac{\eta v_{cl}}{\gamma_{LV}} \tag{1.4}$$

where η is the liquid viscosity and v_{cl}, the contact line speed. For contact line speeds lower than 200 μm/s, Ca is always less than 10^{-5}, and deviation from the Laplace-shape is expected to occur at distances in the order of microns, which are well below the typical optical resolution (about 10 μm)(55). Thus, we assure that the drop shape is not disturbed by Hydrodynamics. In this work, we will focus on the capillary-driven regime of forced wetting where the interface shape far away from the contact line will be quasi-static, i.e. speed-independent.

Stick/slip phenomena

The existence of boundaries between surface domains of different chemistry or elevation can cause several observable effects on the three-phase contact line, such as corrugation (57) and "pinning" (95, 96), depending on the measuring scale used. Pinning or canthotaxis (97) occurs when

[i] It is worth pointing out that in forced wetting, the system is continuously changing its thermodynamic state (e.g. through the drop volume) and thereby, in general the equilibrium contact angle will depend on the solid-liquid area (see Figure A.7)

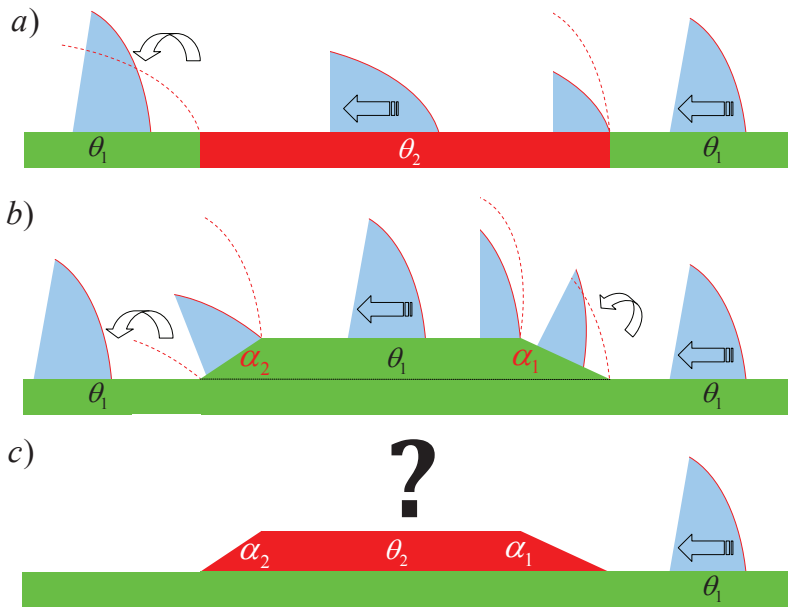

Figure 1.10: (a) Stick-slip behaviour of a sessile drop on a smooth heterogeneous surface ($\theta_1 > \theta_2$). (b) Stick-slip behaviour of a sessile drop on a rough homogeneous surface ($\theta_1 > \alpha_1, \alpha_2$). (c) Complex stick-slip behaviour of a sessile drop on a rough heterogeneous surface.

the contact line is constrained entirely or locally and as a result the system configurations are geometrically limited. It should be notice that a pinned drop attains a metastable configuration, no necessarily the global energy minimum, although with the contact line constrained. For this reason, the contact angles of constrained drops should be excluded from the interpretation in terms of surface energetics.

When the contact line is moving over a solid, there are often points that remain pinned, then suddenly the contact line jumps to a new position. This phenomenon is related to the presence of aspereties and/or chemical domains on the surface, and it is referred to as "stick/slip" process in analogy to "dry" mechanical friction (98, 99). Alike to mechanical friction, the stick or pinning behaviour is a consequence of the opposition that presents a surface to the movement of the liquid front. However, the occurrence of a single stick is not a macroscopic evidence of CAH (see Section A.4). One of the uncertainty sources in the measure of contact angle is the own stick/slip phenomenon (100). The prediction of the motion of a contact line subjected to stick-slip events can become very hard (see Figure 1.10).

As explained in Appendix A for adhesion hysteresis, CAH requires two conditions: the existence of multiple local minima in the system free energy (71, 101), and the dependence of the location and the number of these metastates on the system size (98). If the external conditions do not change, the drop will indefinitely remain in an arbitrary local energy minimum it may initially

occupy (see Section 1.1.2). A way to force the system to evolve is to change the drop volume (see Section 2.2). Varying the volume distorts the energy profile, eventually transforming the initial minimum into an inflection point (see Figure A.7). At that moment, the system loses stability and makes a spontaneous jump to the nearest local minimum. During the jump, the energy of the system suddenly decreases. Some energy is thus irreversibly dissipated as heat. It is worth pointing out that, unlike a stick event, the occurrence of a jump implies the existence of CAH and viceversa (58).

1.2 Freely evaporating drops

Drop evaporation plays a vital role in various engineering fields, such as air/fuel-premixing, (biological) crystal growth, painting and inkjet printing. Evaporation of sessile drops was described many years ago (102, 103). On the contrary, some underlying principles of the dynamic process of evaporation have been recently published (104). Drop evaporation occurs even in the case where the ambient vapor pressure equals the saturation vapor pressure above a flat liquid vapor interface. A drop has a curved surface and as described by Kelvin's equation (105), the vapor pressure of a curved liquid surface is higher than the saturation vapor pressure (106). Hence, evaporation of drops is really avoided upon oversaturation conditions (106).

Due to the drop shape (hydrophilicity/hydrophobicity character of the substrate), the evaporation rate at the contact line can be very different. This rate will become maximum for hydrophilic substrates and minimum for hydrophobic substrates. The probability of escape of an evaporating molecule is affected by the curvature of its point of departure (see Fig. 1.11). A random walk initiated at the apex of a flattened drop results in the molecule being reabsorbed. Instead, if the drop is rounded, the molecule gets to escape from the apex. However, on a hydrophilic surface, the same random walk initiated from the three-phase contact line allows the evaporating molecule to escape due to the high local curvature. On a hydrophobic surface, since the flux vector points out towards the solid surface at the contact line, the evaporating molecule cannot get away from the drop surface. This demonstrates why the evaporation rate is larger at the edge of wetting drops ("wedge effect") than at the apex. Just the opposite argument is applicable to non-wetting drops.

When the evaporative flux of liquid is relatively constant across the drop or moderately enhanced at the contact line (hydrophilic surfaces), an outward flow develops in the liquid in order to maintain the drop shape (imposed by the liquid surface tension and gravity). Conversely, if evaporation primarily occurs at the center of the droplet (hydrophobic surfaces), then the liquid flows toward the center of the drop. Evaporation also produces a decrease of the temperature within the drop, which leads to both a heat flux from the substrate into the drop, and to Marangoni effects

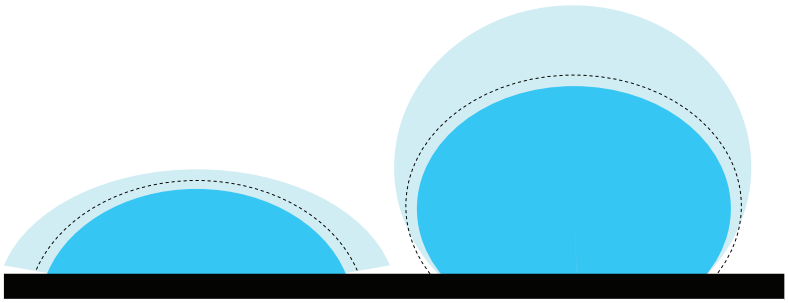

Figure 1.11: Evaporation rate of two sessile drops placed on a hydrophilic surface (left) and on a hydrophobic surface (right). The region around the free surface of each drop illustrates the intensity of the local evaporation rate. The dashed lines represent the situation of uniform evaporation rate if the probability of escape of an evaporating molecule were constant.

(flows driven by surface tension gradients) if the temperature within the drop is not uniform.

Generally, the evaporation of sessile drops occurs in two distinct modes: at a constant contact radius and decreasing contact angle and next, at a constant contact angle and decreasing contact radius (see Figure 1.12). The constant contact angle mode has been reported in a few instances, such as water drop evaporation on PTFE where the initial contact angle is greater than 90. During the evaporation of a sessile drop, the triple contact line of the drop can be "pinned" to the surface, due to CAH. This pinning prevents the drop from receding and so, the drop contact radius remains constant. Just before the backward movement of contact line, a receding contact angle is hold. Rigorously, receding contact angle occurs when the three-phase contact line is incipiently moving on solid surfaces. In practice, the reproducibility of experiments with evaporating drops is very poor (see Figure 1.13). Kinetics of evaporating drop is very long since evaporating drops undergo a minimum rate of liquid loss. Furthermore, there is a strong influence on the receding contact angle value from the rate of liquid removal from the drop. When an evaporating drop recedes very slowly, it may be trapped at the first local energy minimum that is encountered (see Section 1.1.3).

It is known that the evaporation time is proportional to the initial drop volume. For the case of drop evaporation in saturated vapor and constant contact angle, it has also been reported that the liquid-vapour area, A_{LV}, decreases linearly with time (104, 107). If a sessile drop is slowly shrinking with constant contact angle, the following rule should be hold neglecting thermal and Marangoni effects:

$$\frac{dA_{LV}}{dt} = \frac{dA_{SL}}{dt}\cos\theta_r \tag{1.5}$$

where A_{SL} is the solid-liquid area and θ_r, the receding contact angle. From Eq. 1.5, if $A_{LV} \propto (t_p - t)$ then $r_c^2 \propto (t_p - t)$, as well. The time t_p (pinning time) stands for the transition time between the fixed contact line mode and the constant contact angle mode. For spherical drops, the volume scales with contact radius as $V \propto r_c^3$ (see Appendix B). If this scaling applies to

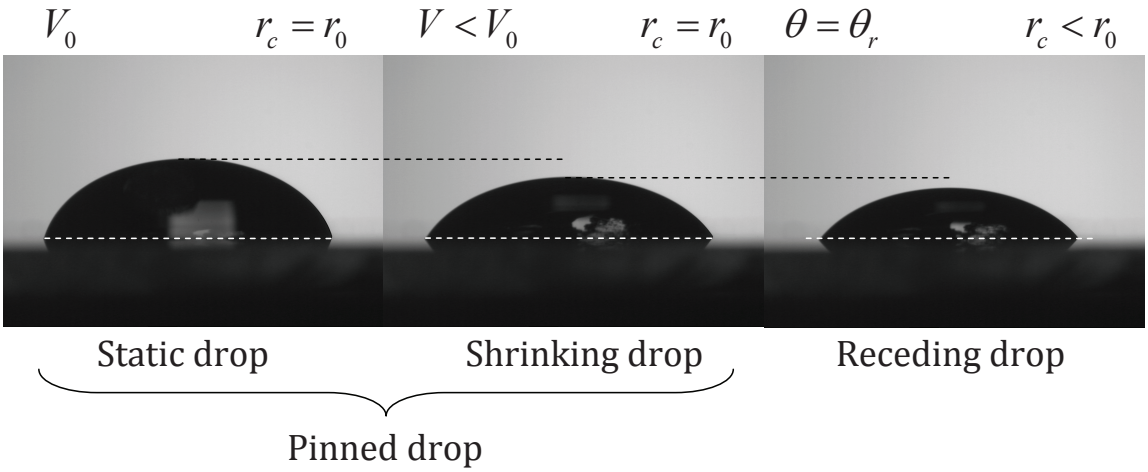

Figure 1.12: Evolution of an evaporating sessile drop. Initially, the sessile drop with a volume V_0 is static and it holds an arbitrary value of contact angle due to the drop formation/placement (CAH). Next, due to the loss of liquid, the drop height and contact angle slowly decrease whereas the contact line is pinned. Once the receding contact angle is reached, the drop begins to move back with a fixed contact angle. Usually, when the drop volume is small, there is a fast final stage where contact angle and contact radius decrease at once.

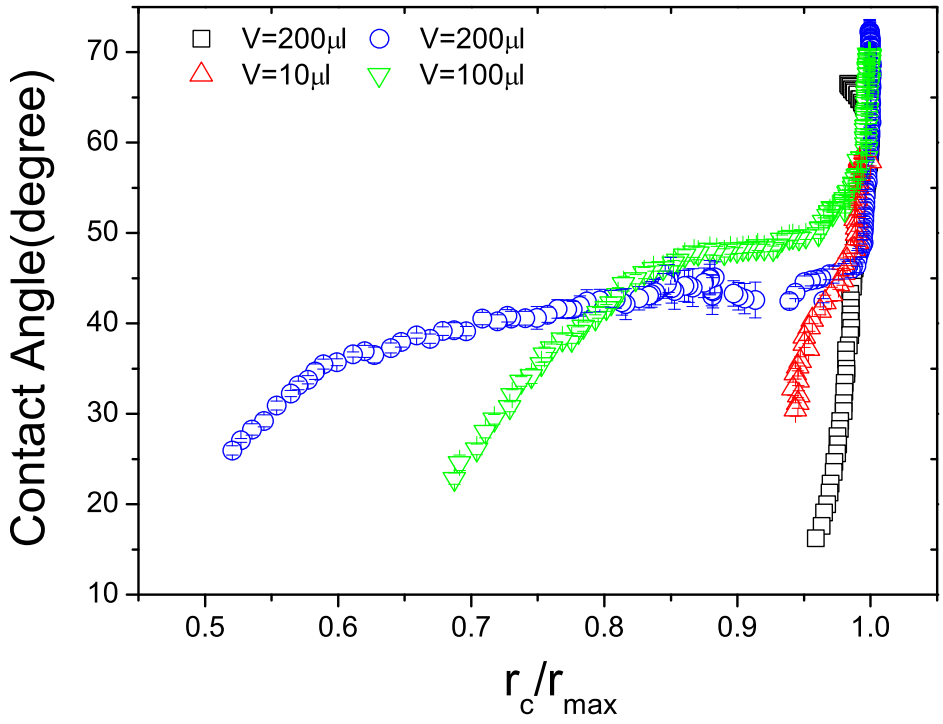

Figure 1.13: Contact line dynamics of freely evaporating drops of Milli-Q water on PMMA substrates. It should be notice the poor reproducibility of the measurements.

gravity-flattened drops, we predict that $V \propto (t_p - t)^{3/2}$ for the constant contact angle mode of drop evaporation. In fact, this result agrees with the evaporation rate of a receding drop (104):

$$-\frac{dV}{dt} \propto \sqrt{t_p - t} \tag{1.6}$$

whereas the loss rate of volume for a sessile drop with fixed contact line is:

$$-\frac{dV}{dt} = const. \tag{1.7}$$

CHAPTER 2

Materials and techniques

Receding contact lines of pure liquids

2.1 Materials

We employed six polymers (2mm-thick sheets, CQ grade, Goodfellow©) and commercially pure (unalloyed) titanium (ASTM grade 2-Manfredi©). We selected these materials by their different wettability response. The titanium surfaces were finely polished but the polymer surfaces were analyzed as received except for PTFE, which was further subjected to a heat pressing treatment. The roughness values of each surface are summarized in Table 2.1. The roughness was measured with a white light confocal microscope (PLμ, Sensofar©-Tech S.L.) using a 50x objective (196.7x196.7 μm^2).

The polymers were cut as square pieces (1.5 cm x 1.5 cm) and the titanium as discs (1.6 cm in diameter). A hole of 1 mm diameter was drilled on each sample. Before each experiment, the surfaces were cleaned ultrasonically in a detergent solution for 10 min, followed by ultrasonic rinsing in Milli-Q water. Next, the samples were immersed in ethanol (analytical grade, Sharlau Chemie, Spain) and sonicated for 10 min. Finally, the samples were immersed in Milli-Q water

and sonicated again for 10 min. The cleaning procedure described was employed for most of the polymers except for the PMMA that was immersed in hexane (analytical grade, Sharlau Chemie, Spain) instead of ethanol, which is known to be a poor solvent to PMMA.

Acronym	Material	R_a(nm)	RMS(nm)
PMMA	Poly(methyl methacrylate)	34	41
PS	Polystyrene	11	18
PET	Poly(ethylene terephtalate)	12	18
PTFE	Poly(tetrafluoroethylene)	1208	1558
hp-PTFE	Heat-pressed PTFE	110	150
PC	Polycarbonate	14	19
uPVC	Unplastified poly(vinyl chloride)	13	18
Ti	Titanium	15	18

Table 2.1: Arithmetic height (R_a) and root-mean-squared height (RMS) of the surfaces used in this work. These parameters illustrate the roughness degree of each surface.

Occasionally, for certain polymers, the receding angles decrease with time due to irreversible molecular rearrangements occurring at solid-liquid interfaces after they come into contact (see Figure 1.8). This proves that the receding angles depend on the contact time between solid and liquid. However, at higher rates of motion, receding contact angles become time-independent, indicating that water molecules do not find the opportunity to modify the polymer film significantly (108).

2.2 Low-rate dynamic contact angle technique

Low-rate dynamic contact angle measurements are based on forced wetting (see Section 1.1.4). In this technique, the observable contact angles of growing/shrinking sessile drops or captive bubbles are measured (93). The meniscus volume (liquid or air) is *steadily* changed from *below*[a] the surface with a motor-driven syringe. The advancing and receding contact angle measurements are performed, respectively, by an increase or decrease in the drop volume (inversely for air bubble). A scheme of this mechanism is shown in Figure 2.1.

The role of the volume variation is just to force the system to pass from one local energy minimum to the next, until it reaches the advancing/receding metastate. The sequence of energy minima visited is the only important feature, and time plays no role. Through this mechanism, the system probes progressively larger regions of surface. The strategy of pumping liquid from below the surface was pioneered by Oliver et al. (109) because of its potential for avoiding drop

[a] In order to facilitate the experimental procedure, a hole in the solid surface (0.5-1 mm diameter) is required

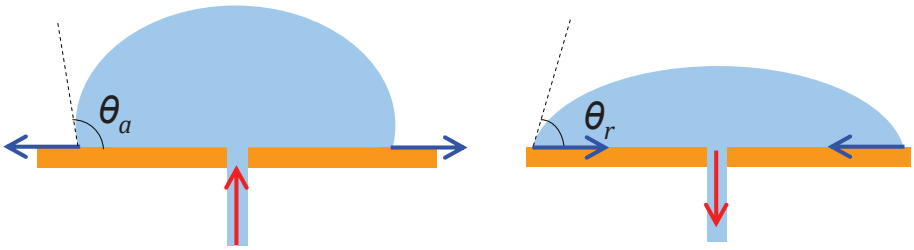

Figure 2.1: Low-rate dynamic contact angle technique.

vibrations and for measuring true advancing contact angles without disturbing the drop profile. Further, low-rate dynamic contact angle technique allows to examine the drop size effect on the observable contact angle.

Commonly, low-rate dynamic contact angle measurements are achieved with a continuous linear variation of drop volume, i.e. a Constant Flow Rate (CFR). It should be noted than a linear rate of change in the drop volume does not correspond to a linear rate of motion of the drop front. Figure 2.2 illustrates a typical result obtained from a low-rate dynamic contact angle experiment. As shown in such figure, three traces are obtained as a function of time: (a) volume, (b) three-phase contact radius, and (c) contact angle. These graphs are divided into domains by means of vertical lines for analysis. The first segment ranges from the beginning of the experiment to the time when the advancing mode is reached, the next domain goes from the advancing mode point till the moment when the motor is stopped. Then a relaxing time follows. The next region initiates when the motor is switched and covers up to the attainment of the reverse mode and the liquid was started to flow back into the syringe, this part represents the transition from advancing to receding contact angles, i.e. the period in which the three-phase line is stationary (this is a pinning mode). This mode is characterized by a constant radius, and a rapid decrease in the contact angle, such pattern continues until it reaches a point at which the periphery recedes, i.e. the beginning of the receding domain.

It is known that contact line dynamics dictates the measured values of contact angle. Some authors have reported (59, 80) that the main problem in the disagreement of the advancing and receding contact angles obtained with low-rate dynamic contact angle technique for the same solid-liquid system are the variable rates of growing/shrinking of drop.

2.3 Experimental set-up for contact angle measurements

The experimental set-up used for the contact angle measurements is shown in Figure 2.3. In this technique, a small hole was drilled in the substrate sample and a tube was connected to

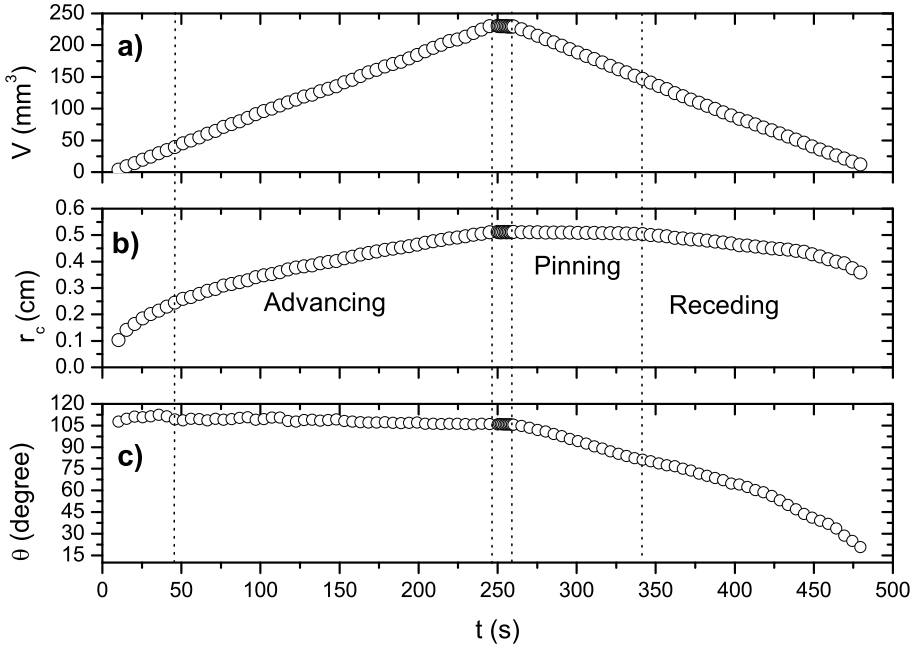

Figure 2.2: A typical low-rate dynamic contact angle experiment of Milli-Q water on a rough PTFE surface: (a) volume, (b) three-phase contact radius, and (c) contact angle

this hole beneath the substrate. The drop volume was then changed by removing liquid to a initial drop by means of the tube connected to a motorized micrometer syringe (Hamilton© PSD3). In our experiments, we used standard resolutions (1000 or 2000 increments for full stroke), accordingly. We used a 250μl-Hamilton© syringe and Milli-Q water as probe liquid. Due to the drop dimensions, a microscope (Leica© Apo-Zoom) was coupled to a SONY© CCD (Charge Couple Device) camera. The interface is light-contrast illuminated using a plane and homogeneous light source (Dolan Jenner QVABL). The video image signal was digitalized with a video card connected (Data Translation DT3155) to a PC. Once the image was digitalized, the detection process provided a set of points that represented the drop profile. Drop profiles were analyzed with the Axisymmetric Drop Shape Analysis-Profile (ADSA-P) technique (73). With this approach, all the drop parameters such as contact angle, contact radius, area, volume and surface tension were extracted. The maximum volume of drop was chosen 220 μl. The purpose of choosing relatively large drops was to avoid any possible line tension effects on the measured contact angles and to assure the observation of receding contact angle (see Section 1.1.3). The experiments were achieved at (21-24$\pm$1)°C and 40-55% RH. Each experiment performed on the same sample was repeated five times to obtain reasonable statistics.

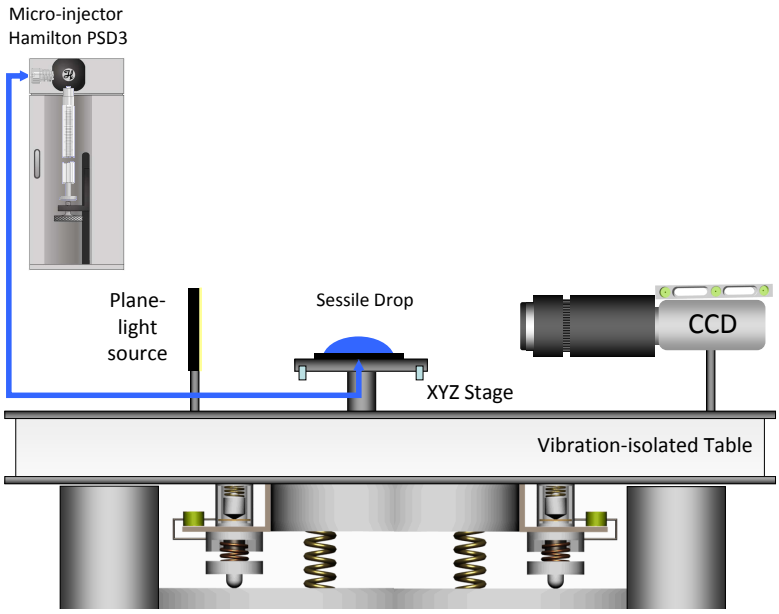

Figure 2.3: Experimental set-up for contact angle measurements.

	Contact radius	**Flow rate**	**Drop volume**
Spherical drop	$\sim t$	Quadratic	$\propto t^3$
Gravity-distorted drop	$\sim t$	Non-linear	$\propto t^{3\alpha}$
"Pancake" drop	$\sim t$	Linear	$\propto t^2$

Table 2.2: Volumetric flow rate devoted to produce the steady motion of contact line according to the drop shape. The volume-contact radius scalings of spherical drop is $V \propto r_c^3$ and of "pancake" drop, $V \propto r_c^2$ (see Appendix B

2.4 Sessile drops with steadily-driven contact line

Low-rate dynamic contact angle experiments with sessile drops are usually performed from the steady variation of drop volume (Constant Flow Rate-CFR, $V \propto t$), from below the surface, using a motor-driven microsyringe (93). In order to achieve the steady motion of three-phase contact lines, we employed a quadratic volumetric flow rate (Quadratic Flow Rate-QFR, $V \propto t^3$). We focused on the capillary-driven regime where the interface shape far away from the contact line (order of microns) was quasi-static, i.e. speed-independent. For an arbitrary sessile drop, flattened by gravity, the scaling exponent between volume and contact radius depends on the drop shape, varying its value between 2 (spherical drop) and 3 ("pancake" drop). This behavior is summarized in Table 2.2 and detailed in Appendix . However, in this work we used the volume-contact radius scaling of spherical drops to reproduce steadily moving contact lines (see Table 2.2). In Section 2.4.2, we described the implementation of the QFR method, which was validated with gravity-distorted drops ($\sim 100 - 200\mu$l).

The rate employed in the CFR method was 1 μl/s, such as in typical experiments of low-rate dynamic contact angle. The maximum volume of drop was 120 μl. We chose relatively large drops to avoid any possible line tension effects (110) on the measured contact angles and to assure the observation of receding contact angle from a geometrical point of view. Moreover, it is well known that the large drops are most susceptible to ambient vibrations, which tend to relax the drops towards different configurations due to the small relative height of the energy barriers separating them. An initial drop of approximately 20 μl was carefully injected, covering the hole in the surface. This "seed" drop ensured that the drop axisymmetrically grew in the center of the image field when the liquid was supplied. The typical values of relaxation time of drop due to inertia and viscous effects were $<$0.05 s and 0.4-0.7 μs, respectively. The capillary-driven regime using a non-linear volume variation was guaranteed because the time lapsed between each addition/removal of liquid was greater than 0.05 s.

In the typical low-rate dynamic contact angle experiments, we observed that roughly the half volume of initial drop was "wasted" until the contact line began to recede. In order to optimize the receding contact angle measurement, we created static drops of fixed volume but different contact angle. This was performed as the following procedure: we injected at CFR an initial amount of water, V_0, and next, we sucked another amount, ΔV, at the same flow rate until to reach the target volume V ($= V_0 - \Delta V$) but with the three-phase contact line fixed. By changing the values V_0 and ΔV deliberately, we were able to modify the observable contact angle, within the hysteresis range, from the advancing contact angle to the receding contact angle. Once the drop was formed, we measured the static contact angle. Finally, we performed the withdrawal of water at QFR to produce the uniform receding motion of the shrinking drop (see Figure 2.4).

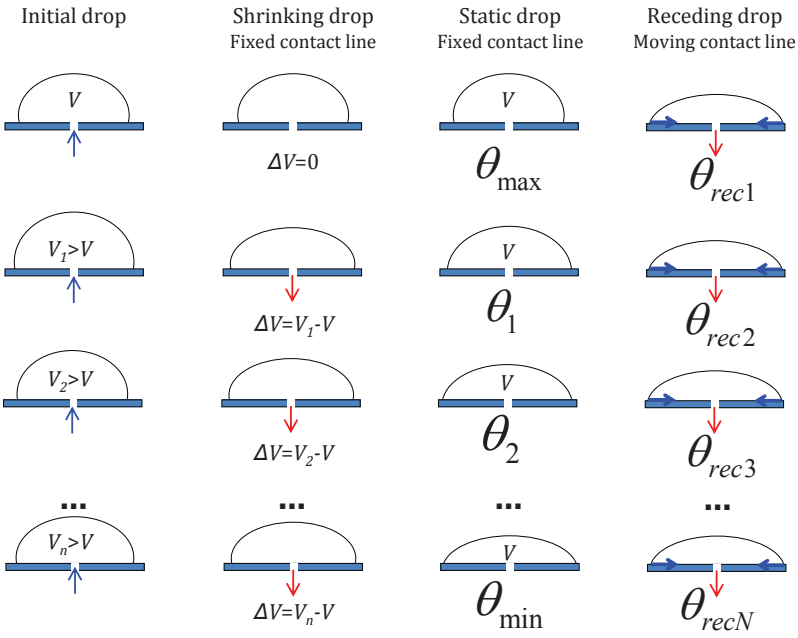

Figure 2.4: Methodology followed to form static drops with fixed volume but different contact angle, before the receding mode.

2.4.1 Statistical correlation

A statistical correlation analysis was performed on each contact angle data (73) obtained with the CFR and QFR methods, separately. To obtain the mean advancing/receding contact angle, we chose just the range where the contact angle was uncorrelated with time, i.e. the time-independent contact angles. When time plays no role in capillary-driven forced wetting, the plot of contact angle as a function of the three-phase contact radius becomes helpful. This way, the quality of the surface (asperities, chemical patches) can be observed indirectly through the measured contact angles.

2.4.2 Implementation of the Quadratic Flow Rate method

A continuous function, such as the drop volume in low-rate dynamic contact angle experiments, can be discretized following three methods: uniform x-axis intervals, uniform y-axis intervals and uniform slope values (see Figure 2.5). Obviously, greater number of discrete spans, minor differences between strategies. The best solution is the third one because it captures the curvature information of the function. To change the drop volume as a given law, with a small number of steps, the slope sampling and the horizontal sampling require very low values of flow rate. Instead, we chose the discontinuous variation of drop volume in time at increasing/decreasing motor speeds (constant volume variation) due to the limitations of stepper-motor-driven syringe

pumps (i.e. minimum speed). This way, we were able to control the volumetric flow rate of injection and retraction of the liquid. We divided each growing/shrinking mode into small liquid additions/withdrawals, which were reproduced at CFR following the cubic law $V \propto t^3$. Hence, the QFR experiment was performed from a sequence of CFR experiments with the same volume variation (6.65 μl for 120 μl-drops and 4.65 μl for 75 μl-drops) but different elapsed time (0.4-7.1 μl/s). We acquired at least one image immediately after each CFR step.

The algorithm used to perform the QFR is described as follows. Firstly, we choose the maximum volume of liquid exchanged with the drop, $V_{\max}$, which is limited by the microsyringe volume and the microinjector resolution, next the amount of liquid exchanged for a CFR process, ΔV, which is limited by the number of CFR processes, $n = \frac{V_{\max}}{\Delta V}$, and finally, the length of the overall process, $t_{\max}$, which is limited by the maximum full stroke time of the microinjector. Hence, if we intend that the drop volume scales as the following cubic law:

$$V(t) = V_0 + V_{\max}\left(\frac{t}{t_{\max}}\right)^3 \tag{2.1}$$

where V_0 stands for the initial drop volume, then each CFR process should take long:

$$\Delta t_i^+ = \left(i^{\frac{1}{3}} - (i-1)^{\frac{1}{3}}\right)\left(\frac{\Delta V}{V_{\max}}\right)^{\frac{1}{3}} t_{\max} \tag{2.2}$$

at a flow rate:

$$\dot{V}_i^+ = \frac{\Delta V}{\Delta t_i} = \frac{1}{i^{\frac{1}{3}} - (i-1)^{\frac{1}{3}}} \frac{(V_{\max})^{\frac{1}{3}} (\Delta V)^{\frac{2}{3}}}{t_{\max}} \tag{2.3}$$

where i varies from 1 up to n (typically 15) and the superscript $(+)$ refers to liquid addition. The variation of drop volume will obey the cubic law (Eq. 2.1) better as the value of n increases. However, special care should be taken because once the number of CFR processes, n, and the maximum time, $t_{\max}$, are fixed, the values of flow rate (Eq. 2.3) might be repeated due to the numerical rounding imposed by the digital driver of the microinjector.

The QFR method for steadily-receding drops was designed as follows:

$$\Delta t_i^- = \Delta t_{n-i+1}^+ \tag{2.4}$$

and:

$$\dot{V}_i^- = \dot{V}_{n-i+1}^+ \tag{2.5}$$

where the superscript (-) refers to liquid removal. For this case, the drop volume was accordingly changed as the cubic law:

$$V(t) = V_0 + V_{\max}\left(1 - \frac{t}{t_{\max}}\right)^3 \tag{2.6}$$

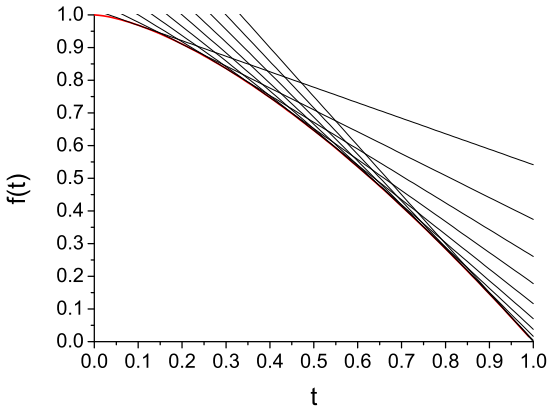

(a)

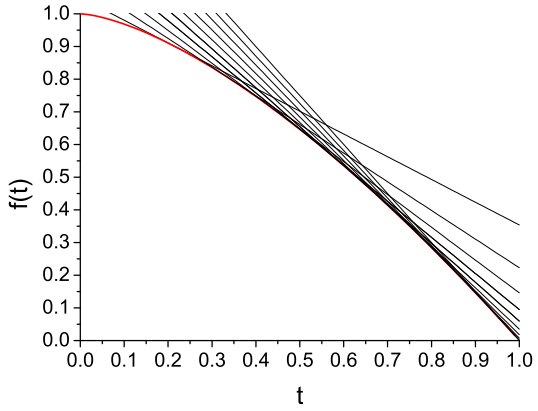

(b)

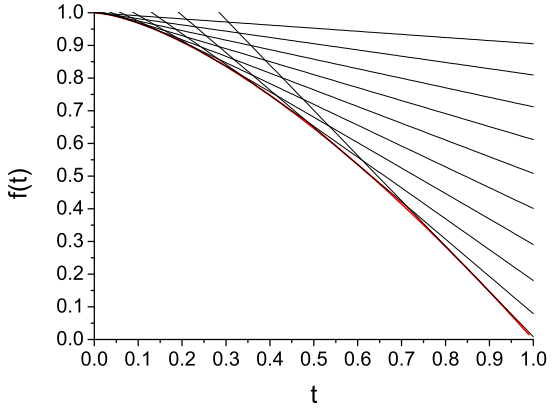

(c)

Figure 2.5: Discretization of a nonlinear continuous function in: (a) uniform x-axis intervals, (b) uniform y-axis intervals and (c) uniform slope values.

	Flow rate	Liquid-vapor area	Contact radius	Contact angle
Static shrinking drop	Quadratic	–	$\propto (t_p - t)^2$	$> \theta_r$
Receding shrinking drop	Square-root	$\propto (t_p - t)$	$\propto \sqrt{t_p - t}$	θ_r

Table 2.3: Contact line dynamics as the volumetric flow rate imposed during the Controlled Shrinking Sessile Drop method.

which is the corresponding "mirror-like" law to Eq. 2.1.

This volume variation produced very consecutive withdrawals of liquid at the beginning of the process. This way, Eq. 2.6 enabled that the system reached a stable configuration during the motion of contact line, as shown in Figure 3.2, rather than be trapped at the first attainable metastable configuration.

2.5 Controlled Shrinking Sessile Drop

We intend to mimic the contact line dynamics of evaporating sessile drops at shorter timescale (600-900 s), without significant macroevaporation. We will focus on receding contact lines of large sessile drops ($120 - 220 \mu l$). Although uniformly moving contact lines hold constant contact angles, the reciprocal is not true, as happens with receding evaporating drops. With a variable rate of withdrawal of liquid (see Sections 2.2 and 2.4), we are able to control the speed of the receding contact line and thus, to emulate the main stages of drop evaporation (see Section 1.2). Unlike what happens during drop evaporation, we avoided that the forced motion of drop were too slow because the system would have time to relax to an arbitrary metastable configuration at each instant.

In our *Controlled Shrinking Sessile Drop* (CSSD) method, we propose to reproduce the contact line dynamics under evaporation-like conditions as Table 2.3. The first stage of drop evaporation (constant contact radius) is better imitated at QFR rather than at CFR, following the law:

$$V(t) = V_0 + V_{\max}\left(1 - \frac{t}{t_p}\right)^3 \tag{2.7}$$

where t_p is the pinning time. Eq. 2.7 adequately reproduces the pinning behaviour of the evaporating drop. This standardizes the impeding motion of the drop on the substrate, giving reproducible receding contact angles. The next stage at constant contact angle (i.e. linearly decreasing liquid-vapor area) is described as the law:

$$V(t) = V_0 + V_{\max} - V_{\max}\left(\frac{t}{t_p} - 1\right)^{\frac{3}{2}}\left(\frac{t_t}{t_p} - 1\right)^{-\frac{3}{2}} \tag{2.8}$$

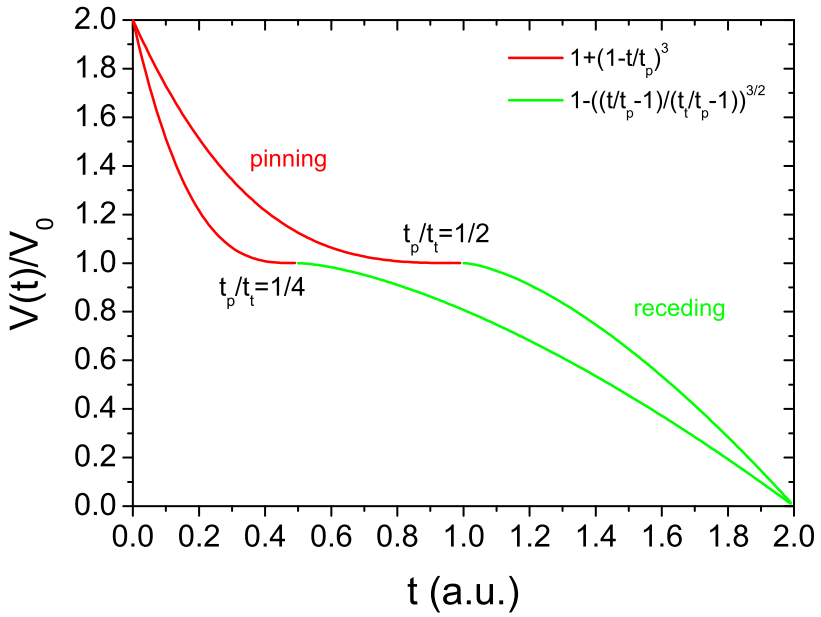

Figure 2.6: Drop volume in terms of time in CSSD experiments. The time t_p symbolizes the pinning time and the time t_t, the length of the process.

where t_t is the total time. Eq. 2.8 is valid for $t > t_p$ and it connects to Eq. 2.7 at $t = t_p$. Finally, drop volume in terms of time in a CSSD experiment is illustrated in Figure 2.6. The CSSD method is able to reproduce the final mixed stage of evaporating drops.

If the hole drilled in the substrate is small enough[b], the height decrease of shrinking drops causes a capillary flow from the bulk solution to the contact line in order to maintain the drop shape. This flow acts as the convective capillary flow of freely-evaporating drops, but at different timescale. Since the liquid is suctioned from the bulk, the flux distribution reproduced is apparently different to the flux generated within a freely evaporating drop. However, the CSSD method standardizes the internal flow in shrinking drops because the flux distribution imposed is the same for all experiments.

The CSSD methodology requires small liquid volumes (microliter range) and small samples of substrate. This enables a better control of the measuring conditions (temperature, casual pollution) and saving of solute. Moreover, drops have minor vibrational susceptibility from the environment that menisci formed in contact to substrates immersed into vessels (milliliter range): less volume, greater resonance frequency. Although some authors (102, 111) utilize a chamber to isolate the drop from its environment, it has been found that virtually there is no difference between the measured contact angles with or without a cuvette. This wat, the CSSD experiments are performed in open air conditions (22^{o}C and 55% RH) with Milli-Q water o buffered water,

[b]In typical CSSD experiments, the hole represents less of the 9% of the distance covered by the receding drops

accordingly.

CHAPTER 3

Results and Discussion

Receding contact lines of pure liquids

In this chapter we illustrate the dependence of the receding contact angle of sessile drops on the dynamics of the three-phase contact line (in the very low capillary number regime) and on the drop placement on the solid surface. As happens in the Wilhelmy balance (74), we explored the response of water drops with steadily moving contact lines on surfaces of polymer and metal oxide. The contact lines were uniformly driven using a non-linear variation of drop volume (108). We monitored receding water drops with equal initial volume but different static contact angle on the same surface. This procedure allowed us to scan the contact angle hysteresis range up to the minimum observable value of contact angle.

3.1 The effect of contact line dynamics and drop formation

In Figure 2.2, we can observe an advancing mode apparently well defined, whereas the receding angle is continuously decreasing. In these cases, receding angles are often estimated from the dynamic contact angle extrapolated to zero velocity. However, this approach is called into question

due to the own CAH: observable contact angle is a function of the previous history of the system.

3.1.1 Comparison between Constant Flow Rate and Quadratic Flow Rate

We measured the low-rate dynamic contact angles of Milli-Q water on the same polymer surfaces, using the conventional method of volume variation (CFR) and our proposal (QFR) (see Figure 3.1a for the water-PMMA system). In Figure 3.1b, we plot the evolution of the contact radius of growing and shrinking drops produced by the CFR method and the QFR method on a PMMA surface. The QFR method produced a steady motion of the contact line over a large surface region. The last five points of the receding contact radius in Figure 3.1b are not meaningful because the instantaneous suction (each point) was so slow and the drop volume was not so large ($< 30\mu$l) that the drop energy was not enough to attain the lower receding contact angle. This will be illustrated in Figure 3.2, where the last five points (inverted triangles) of receding contact angle reveal a relaxation (approx. 1°) compared to the stable value of contact angle.

In Table 3.1, we collect the values of speed and capillary number of the advancing and receding contact lines reproduced with the QFR method for the water-PMMA system. The speed of the three-phase contact line was constant, despite the fact that it was simply controlled by manipulating the drop volume. The small values of capillary number illustrate that the drop shape was governed by surface tension and gravity rather than hydrodynamics. Also, it is worth to highlight that the QFR method, proposed for spherical drops (see Table 2.2), worked satisfactorily even for drops with contact radii nearly twice greater than the capillary length. This proved that the effect of gravity force on the driven contact line was vanishingly small.

Mode	v_{cl} **(μm/s)**	Ca	R^2
Advancing	87.2±1.7	1.2x10^{-6}	0.99224
Receding	-92.6±1.7	1.3x10^{-6}	0.99078

Table 3.1: Values of speed and capillary number of the advancing and receding contact lines reproduced with the QFR method for the water-PMMA system. The values of squared-correlation coefficient R^2 of each linear regression $r_c - t$ prove the steady motion.

Since time plays no role in capillary-driven forced wetting, the representation of contact angles as a function of the three-phase contact radius becomes helpful. The quality of the surface can be observed indirectly in the measured contact angles. If a solid surface is not very smooth then irregular and inconsistent contact angle values will be seen as a function of the three-phase contact radius. When the measured contact angles are mostly constant as a function of surface location, the mean contact angle for a specific rate of advancing/receding can be obtained by averaging the contact angles.

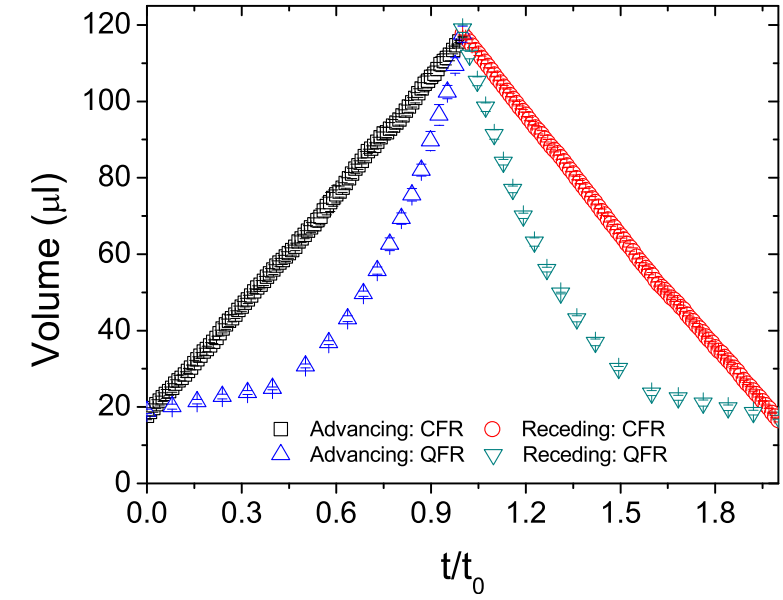

(a)

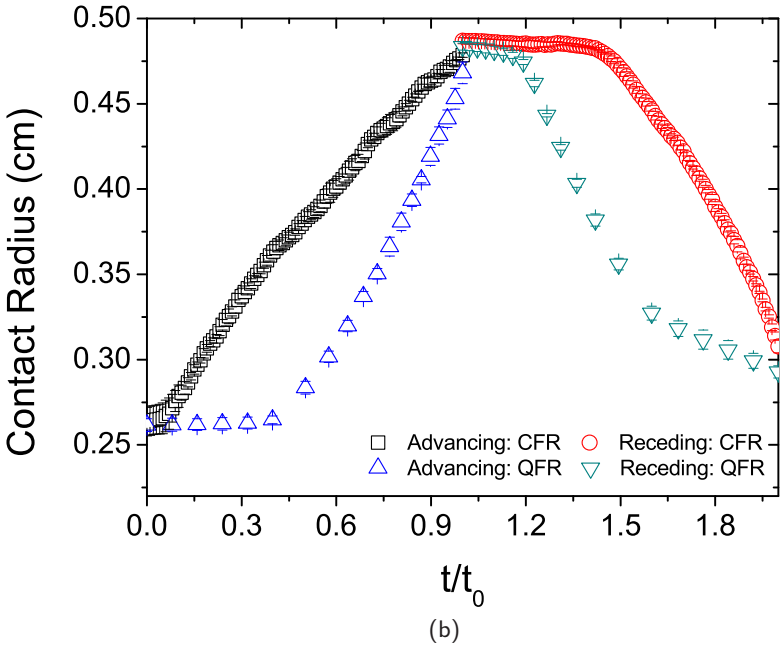

(b)

Figure 3.1: (a) Drop volume and (b) contact radius as function of dimensionless time (for drop growing and shrinking modes), at constant flow rate (CFR) and at quadratic flow rate (QFR) for the water-PMMA system. The symbol t_0 stands for the length of each process performed at CFR (100s) or QFR (40s).

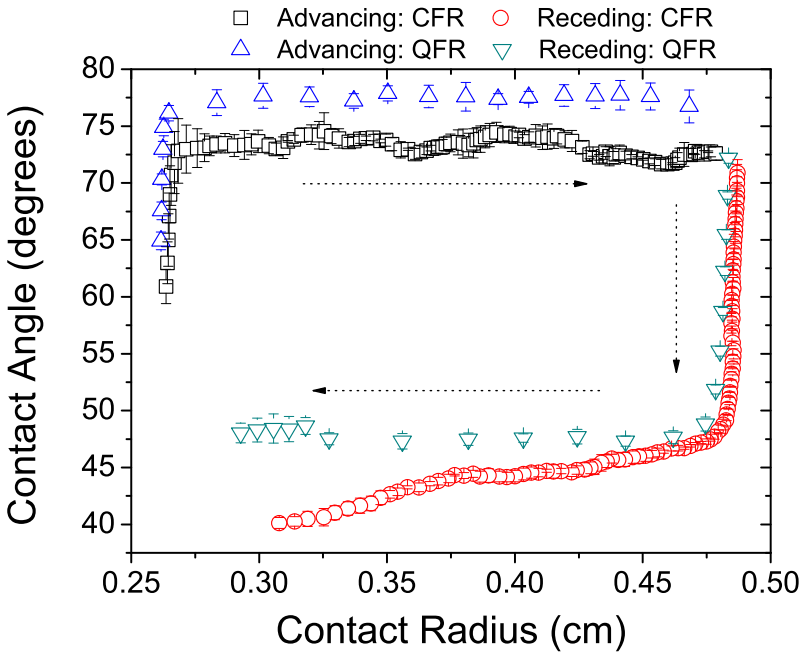

Figure 3.2: Contact angle as function of contact radius (in advancing and receding modes), at constant flow rate (CFR) and at quadratic flow rate (QFR), for the water-PMMA system. It should be noted that the data correspond to mean values and the error bars, to the standard deviations. The gray arrows indicate how the experiment was carried out. The QFR method provided the following values: $\theta_a = 78 \pm 2^\circ$ and $\theta_r = 48 \pm 2^\circ$.

In Figure 3.2, we represent the results for the low-rate dynamic contact angles of Milli-Q water on the PMMA surfaces, using both the CFR and QFR methods. Both methods were sufficiently accurate (see the error bars shown in Figure 3.2), since the experimental uncertainty was small in comparison with the observed contact angle. The time-independent contact angles in advancing mode reproduced with the CFR method were just those ones for which the contact line speed was constant (linear correlation between contact radius and time). However, we found that the receding contact angle decreased continuously as time. As several authors have pointed out (108, 112), this might suggest that the receding contact angle was zero or that kinetic effects due to liquid penetration and/or surface swelling were significant. Instead, the QFR method stabilized the receding contact angle from the same point where the contact line began noticeably to move back with the CFR method. The values of advancing and receding contact angles measured with the QFR method were mostly uncorrelated with time during the uniform motion of the contact line.

If we examine in detail the contact radius for the CFR method in Figure 3.1b, the contact line motion was not uniform. This involved a kinetic energy change that could significantly relax the system towards other metastable configurations different to the advancing one. Hence, the advancing contact angle measured with the CFR method was lower than the value provided by the QFR method. However, the fast changes of volume inside the drop (far away from the contact line) imposed by the QFR method and the use of large drop volumes enabled to overcome the energy barriers caused by roughness or chemical heterogeneity of the solid surface. This behaviour was most significant for receding contact angles (see Section 3.1.2).

Figure 3.3 presents the results of advancing and receding contact angles obtained with the CFR and QFR methods on different polymer surfaces (see Table 2.1). The mean values plotted in Figure 3.3 are statistically meaningful because they were computed from time-independent angles. In all cases, using the QFR method, the advancing contact angle was greater than the advancing contact angle obtained with the CFR method (see Figure 3.3a). The receding contact angle was mostly lower using the QFR method (see Figure 3.3b), except for the PMMA surface. The response of the system with the CFR or QFR methods depended on the free energy landscape of the system (distribution of metastates) and/or the susceptibility of the polymer to swell (time of contact with the liquid). Hence, for the water-PMMA system, the differences in the receding contact angle obtained with the CFR and QFR methods were not significant. Otherwise, the water-PET system behaved very differently. It is worth mentioning that the QFR experiments for advancing or receding mode took shorter than the CFR experiments (40s and 100s, respectively). The contact time between liquid and polymer might play a fundamental role in the observed values of receding contact angle (113). However, we also carried out QFR experiments on rough titanium surfaces and we were able to measure stable low values of receding contact angle (see Figure 3.7).

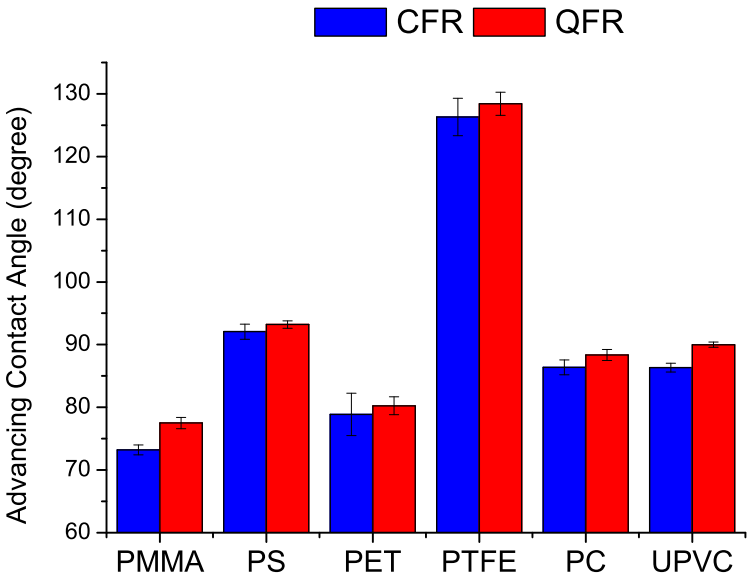

(a)

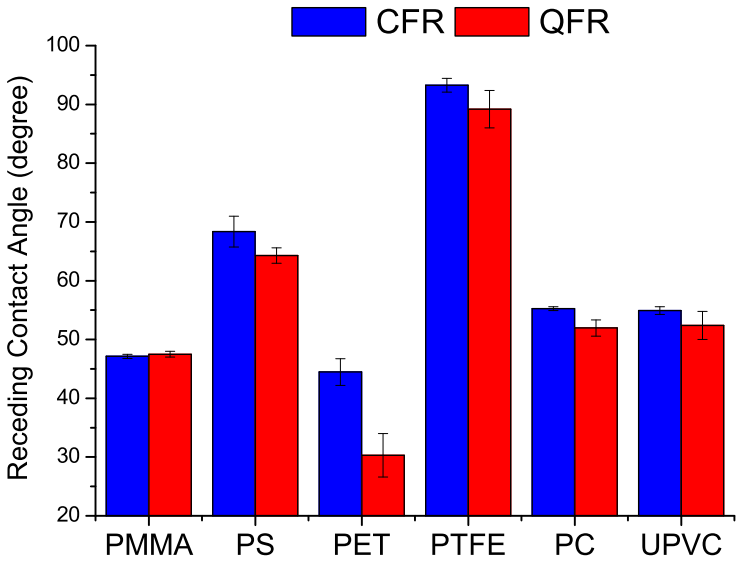

(b)

Figure 3.3: (a) Advancing and (b) receding contact angles measured on different polymers using the CFR and QFR methods.

The QFR method produced the steady motion of the contact line over a larger surface distance (≥ 1 mm) than the CFR method (see Figure 3.5), except for the PC surface in receding mode. The behaviour observed for the PC surface might be due to irreversible molecular rearrangements occurring at the solid-liquid interface after they came into contact (108, 112). In this particular case, the receding angle may depend on the contact time between solid and liquid. It is worth to point out that the distance traveled by an advancing drop at uniform motion was greater than the distance described by a receding drop, except for the PMMA and PTFE surfaces. In fact, the maximum distance covered by receding contact lines with the QFR method was found over the PMMA surface, for which the receding contact angle agreed with the value provided by the CFR method. Using the QFR method, we generally measured more representative values of advancing and receding contact angles, because they were averaged over a greater area of the solid surfaces.

3.1.2 Forced wetting, really?

Low-rate dynamic contact angle measurements are based on forced wetting, where a liquid drop is forced to attain one of the singular metastable configurations within the contact angle hysteresis range. In order to confirm that the QFR method really produced forced wetting, a water drop placed on a PMMA surface was firstly forced to move on and then stopped (see Figure 3.4a). As the drop volume increased, the three-phase contact line advanced. When the motor was suddenly stopped, the low-rate dynamic contact angle decreased (relaxation) up to a static value (see Figure 3.4b). In the receding mode, a water drop was previously formed, next it was forced to move back and, finally stopped. After the motor was stopped, the low-rate dynamic contact angle increased (relaxation) up to a static value.

The relaxation observed in Figure 3.4b confirms that the contact angle measured with the QFR method was not a statically *stable* contact angle (namely, the contact angle at zero velocity of the three-phase contact line) (73). Varying the drop volume at QFR ensured that the observable contact angle were the advancing or receding contact angle because the drop was deliberately forced to attain a limit advancing or receding configuration (72), respectively. When a drop recedes very slowly, such as an evaporating drop, it may be trapped at the first local energy minimum that is encountered (80, 86). In contrast, the QFR method properly provided energy enough to the drop to overcome the multiple energy barriers of the system and to attain the concerning metastable configuration (advancing or receding).

The energy supplied to the drop using the QFR method was mostly employed to keep the contact line speed and to attain the corresponding forced configuration of the system (114). In receding mode, the large initial drop and the decelerated withdrawal of liquid enabled that the system reached and kept the practical metastable configuration of lower contact angle during the contact line motion.

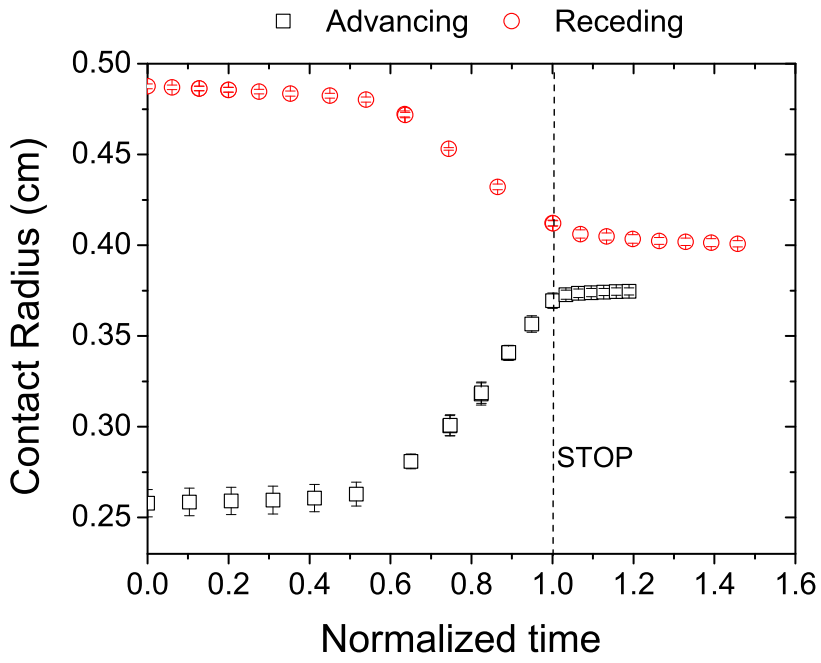

(a)

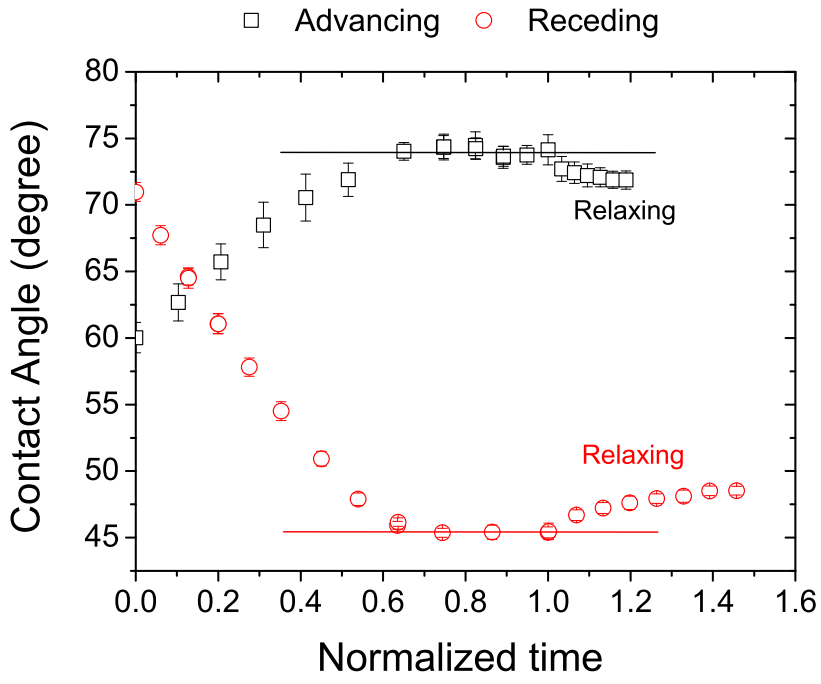

(b)

Figure 3.4: Contact radius (a) and contact angle (b) versus the normalized time for an advancing/receding drop before and after the motor stop, for the water-PMMA system.

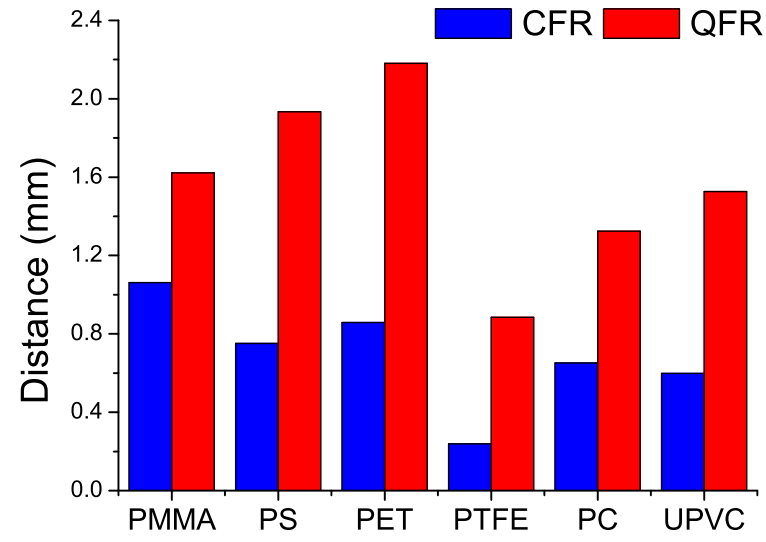

(a)

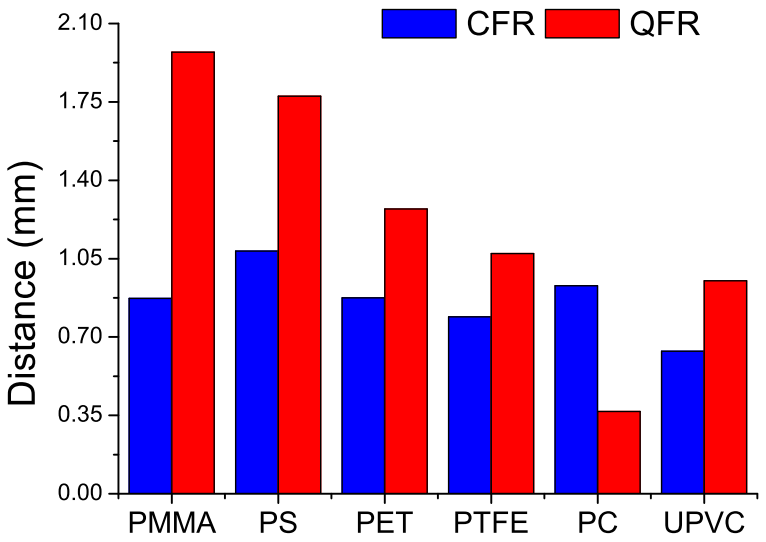

(b)

Figure 3.5: Distance covered by the contact line during the advancing mode (a) and the receding mode (b) with the CFR and QFR methods, separately. The distance was measured over those surface regions where there was no time-contact angle correlation.

3.1.3 Effect of contact line speed on the receding contact angle

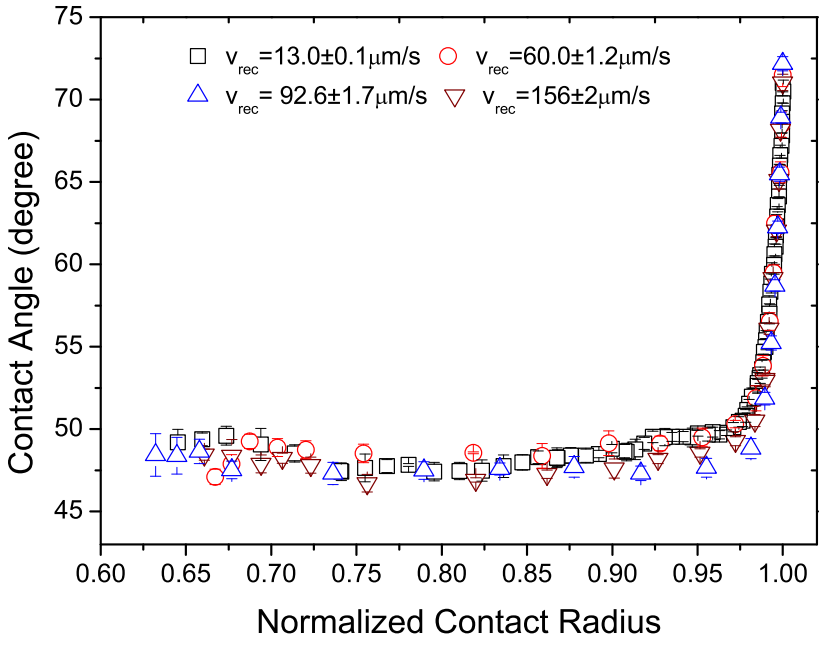

Figure 3.6: Observable contact angle of a shrinking drop (driven at QFR) in terms of the normalized contact radius at different values of contact line speed for the water-PMMA system.

Different causes are proposed in the literature to account for contact angle hysteresis. The most controversial source has been the rate of motion of the three-phase contact line. Some researchers (115, 116) assure that the advancing and receding contact angles significantly depend on this rate. Hence, advancing and receding angles are often estimated from the dynamic contact angle extrapolated to zero velocity. However, Tavana and Neumann (108) found that hydrodynamic effects do not affect the contact angles if the dynamic viscosity of the liquid is well below 10 cP. Hence, advancing and receding contact angles of low viscous liquids (such as water) do not depend on the rate of motion of the three-phase contact line up to 10 mm/min.

In order to study the effect of contact line speed on receding contact angle, we measured low-rate dynamic contact angles on PMMA surfaces using the QFR method at three different receding speeds: 13, 60, 92 and 156 μm/s. From Figure 3.6, no significant variation in receding contact angle was observed provided that the contact line moved at speeds below 160 μm/s, as reported by Tavana and Neumann. This finding validates the QFR method in low-rate dynamic contact angle experiments.

3.1.4 Receding contact angle on rough titanium surfaces

Texturization of surfaces is usually advantageous in biomaterial engineering. The biocompatible properties of a material substrate are closely related to the adsorption of certain proteins. For the evaluation of protein adsorption to a biomaterial, the receding contact angle may be more appropriate for quantifying the properties of the implant surface when it is exposed to an aqueous environment. However, several authors (117, 118) reported the zero value for receding contact angle on rough titanium surfaces.

We etched titanium surfaces with a solution of hydrofluoric acid (Panreac©) at 10% (v/v) for 180 s. This way, the roughness of titanium surfaces was maximized with $R_a = 0.15\mu m$. We performed six experiments of shrinking water drop at QFR on an etched titanium surface (see Figure 3.7). Unlike the CFR method, the QFR method enabled to measure non-zero receding contact angles ($\theta_r = 23.2 \pm 0.7°$) for the rough titanium surface. The high momentum drops driven by the QFR method were able to overcome the multiple metastable configurations, due to the physical barriers of the rough surface, up to attain a stable contact angle.

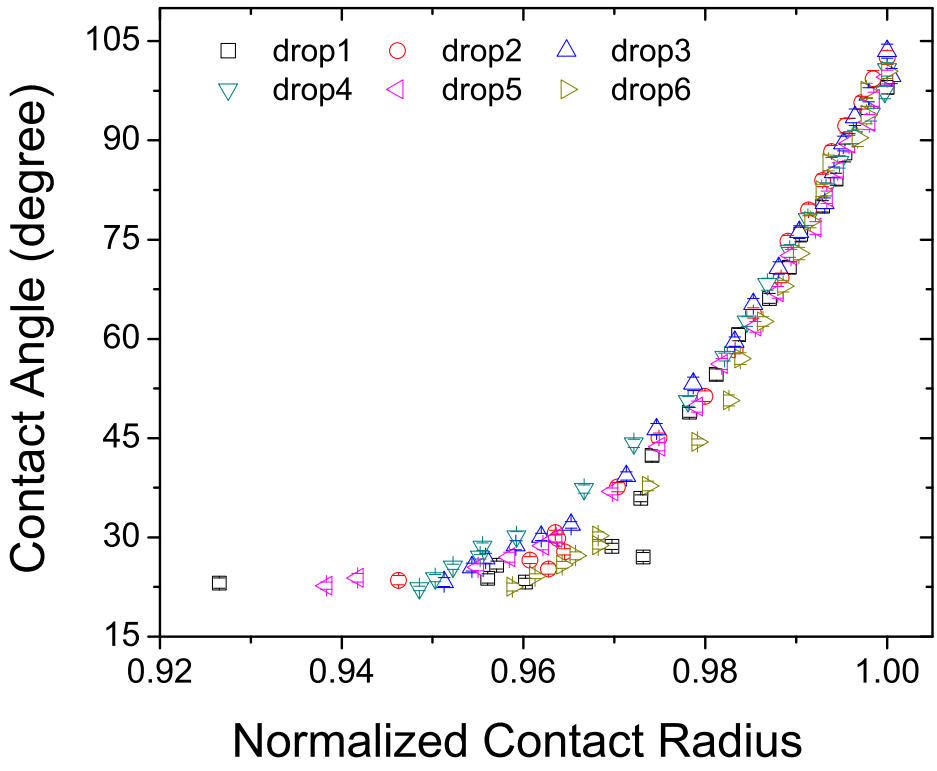

Figure 3.7: Observable contact angle of a shrinking drop (driven at QFR) in terms of the normalized contact radius on an acid-etched titanium surface ($R_a = 0.15\mu m$). No kinetic hysteresis was found.

3.1.5 Dependence of the receding contact angle on the drop formation

The liquid dispensation may be dramatic for receding contact angle measurements. It is known that the drop placement on the surface usually determines the resulting motion of contact line and so, the observed contact angle (87–89). We measured with distilled water the receding contact angle of polymer surfaces (PMMA, PC, PTFE and hp-PTFE) and titanium surfaces, using the QFR method. As described in Section 2.4, we probed the contact angle hysteresis of the system forming initial drops with the same volume but different static contact angle. In order to check the volume dependence of receding contact angle, we performed experiments with two initial drop volumes: 75 μl and 120 μl. We illustrate in Figure 3.8 the shrinking drop experiment for the water-PMMA system. As the static contact angle decreased, we required to remove less volume of water to the drop for the receding motion but the receding contact angle for the water-PMMA system unexpectedly decreased. The surface region scanned by the receding drop was larger as the static contact angle decreased.

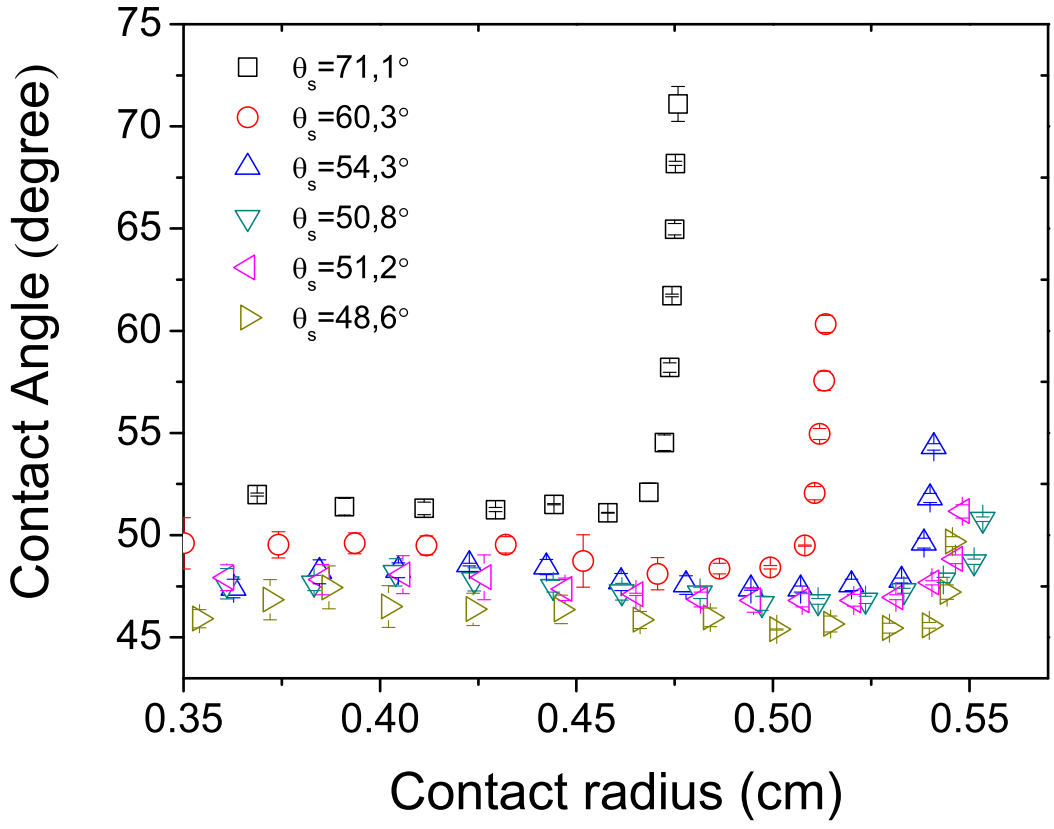

Figure 3.8: Observable contact angle of a shrinking drop (driven at QFR) in terms of the contact radius with different static contact angle for the water-PMMA system. The initial drop volume was 120 μl. As expected, the initial contact radius increased as the static contact angle decreased. These results were obtained with the QFR method.

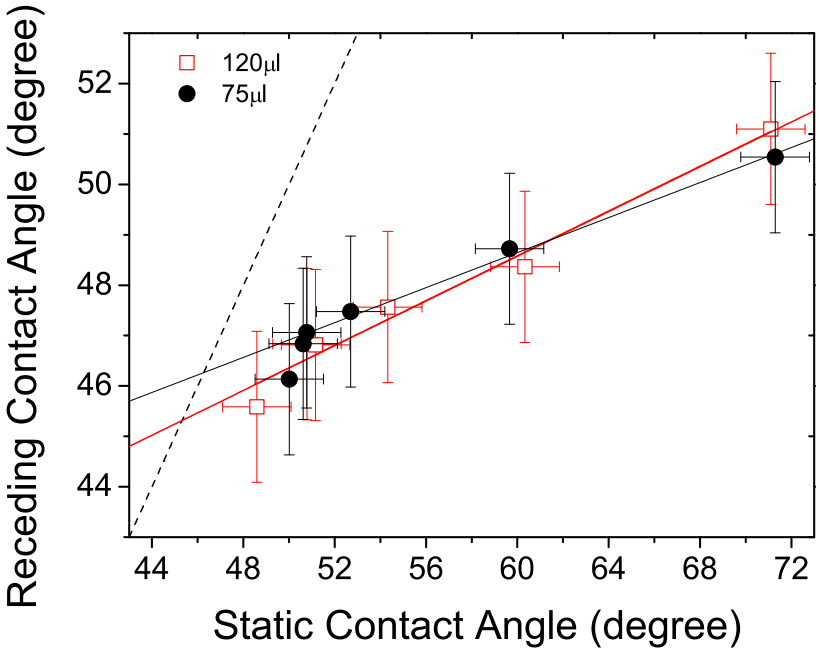

(a)

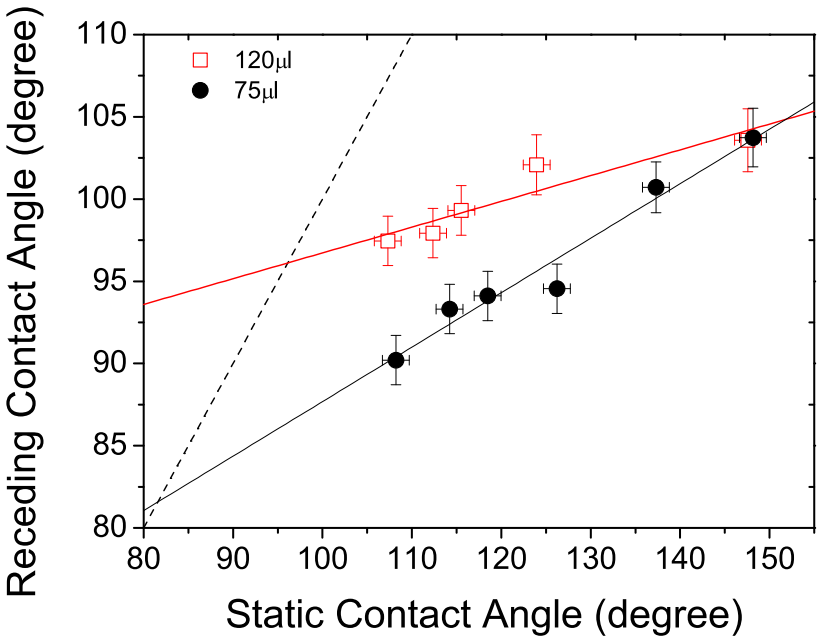

(b)

Figure 3.9: Receding contact angle in terms of the static contact angle for (a) the water-PMMA system and (b) the water-PTFE system. The open symbols correspond to an initial drop of 120 μl and the solid symbols, to an initial drop of 75 μl. The dashed line is the straight line $y = x$. The intersection between this line and the best-fit straight line provided the MRCA value.

Surface	MRCA-120μl(°)	MRCA-75μl(°)	R^2	RCA
PMMA	45.3±2.4	46.2±1.1	0.966/0.991	$\propto$SCA
PTFE	96±9	82±10	0.827/0.954	$\propto$SCA
hp-PTFE	97.9±2.2	94.3±1.5	0.539/0.683	Const.
PC	56.9±0.4	58.9±1.5	0.992/0.743	$\propto$SCA/Const.
Ti	26.0±1.5	-	0.762/	Const.

Table 3.2: Minimum Receding Contact Angle (MRCA) values of the surfaces used. The low receding contact angle of the titanium surface was only observed with 120 μl-drops. In absence of linear correlation, measured from the squared correlation coefficient R^2, the MRCA was estimated as the mean value over all observed receding contact angles. RCA=Receding Contact Angle. SCA=Static Contact Angle.

We plotted the values of receding contact angle in terms of the static contact angle for the two drop volumes studied (see Figure 3.9). We observed an apparent linear dependence between receding contact angle and static contact angle. According to the linear correlation level, we found two behaviours: a constant value of receding contact angle regardless of the static contact angle (see Figure 3.7) and a linear decrease of receding contact angle as the static contact angle decreased (see Figure 3.10a). The second behaviour points out to that, on certain surfaces, the measurement of receding contact angle depended on the drop preparation even using the same technique. This behaviour was occasionally susceptible to the initial drop volume (see Figure 3.10b). In those cases where the linear correlation was medium or high, we calculated the Minimum Receding Contact Angle (MRCA) as the value of receding contact angle extrapolated to the static contact angle. Otherwise, the MRCA was estimated as the mean value over all observed receding contact angles. We collect the MRCA values in Table 3.2. The receding contact angle measured on the PTFE and PMMA surfaces depended on the drop formation. In these cases, the energy of shrinking drops with lower static contact angle was enough to overcome the multiple energy barriers close to the limit receding configuration. Instead, the receding contact angle on the hp-PTFE and Ti surfaces was independent on the drop preparation. Nevertheless, the PC surface revealed a singular behaviour: a high linear correlation between the receding contact angle and the static contact angle for 120 μl-drops and a weak linear correlation for 75 μl-drops. The smoothing of the rough PTFE surface (hp-PTFE) removed the drop preparation dependence and the volume dependence. However, we cannot explain the PC results in terms of roughness effect. A plausible argument for the PC surface might be the different contact time between solid and liquid during the experiments performed with 75 μl-drops and 120 μl-drops, indicating that water molecules did not find the opportunity to modify the polymer film significantly (108, 112).

We plotted the values of receding contact angle in terms of the static contact angle for the two drop volumes studied for the water-hp-PTFE system and the water-PC system(see Figure 3.10). It is worth highlighting that only for both PTFE surfaces (rough and heat-pressed), the

best fitting straight lines were not parallel. This might reveal a roughness effect.

Marmur referred to the term "theoretical receding contact angle" (72) as the minimum value of the observable (measurable) contact angle at incipiently receding contact lines. This contact angle is often poorly repeatable (unstable). Otherwise, Marmur also coined the term "practical receding contact angle" (72) as the minimum value of the observable (measurable) and repeatable (stable) contact angle hold during the entire motion of drop (as illustrated in Figure 3.2). The MRCA estimated from practical receding contact angles is a good approximation to theoretical receding contact angle.

3.2 Controlled Shrinking Sessile Drop

In Figures 3.11 and 3.12, we show a typical experiment performed with the CSSD method. We observed that the liquid-vapour area decreased linearly as time for an intermediate range (see Figure 3.11b), after the pinning stage (see Figure 3.12). As happens with freely evaporating drops, the receding contact line in CSSD experiments held a constant contact angle (see Figure 3.12). We also varied the length of the CSSD experiment (see Figure 3.13). In the fast CSSD experiment (t_t =100s), no hydrodynamics effects were found (see Figure 3.13b). The CSSD method was independent on the process length, up to 900 s. Above 900 s, the shrinking drop began to evaporate significantly because the withdrawal rate was similar to the actual evaporation rate. The CSSD process reproduced the final mixed stage of drop evaporation (see Figure 3.13b).

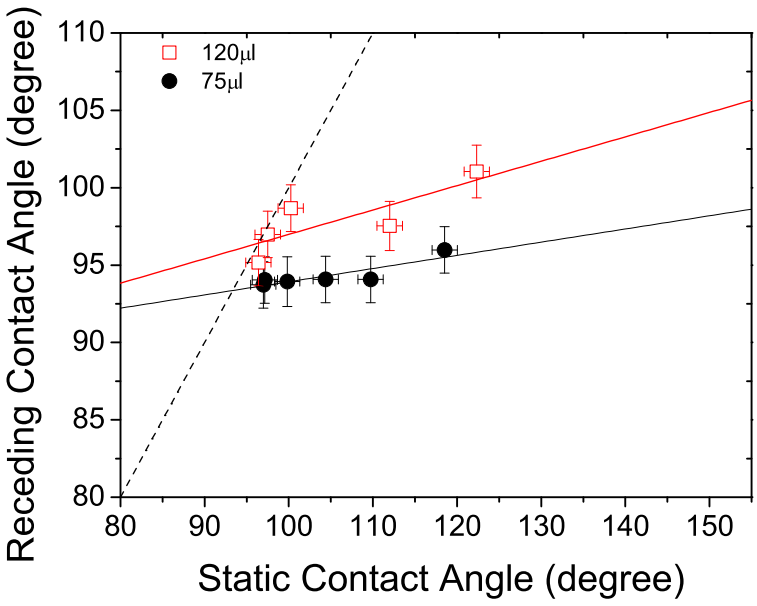

(a)

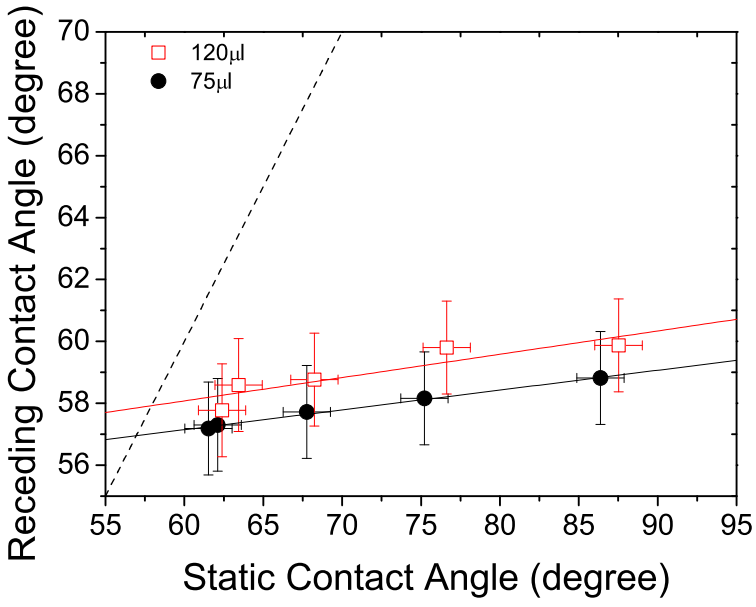

(b)

Figure 3.10: Receding contact angle in terms of the static contact angle for (a) the water-hp-PTFE system and (b) the water-PC system. The open symbols correspond to an initial drop of 120 μl and the solid symbols, to an initial drop of 75 μl. The dashed line is the straight line $y = x$. The MRCA value was calculated as the mean value of receding contact angles (no linear correlation) or as the intersection between the dashed line and the best-fit straight line, accordingly.

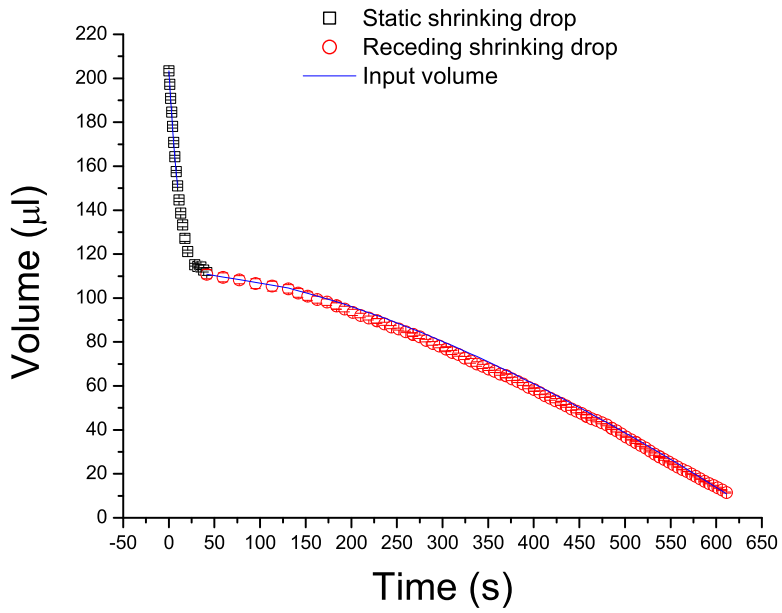

(a) Drop volume in terms of time

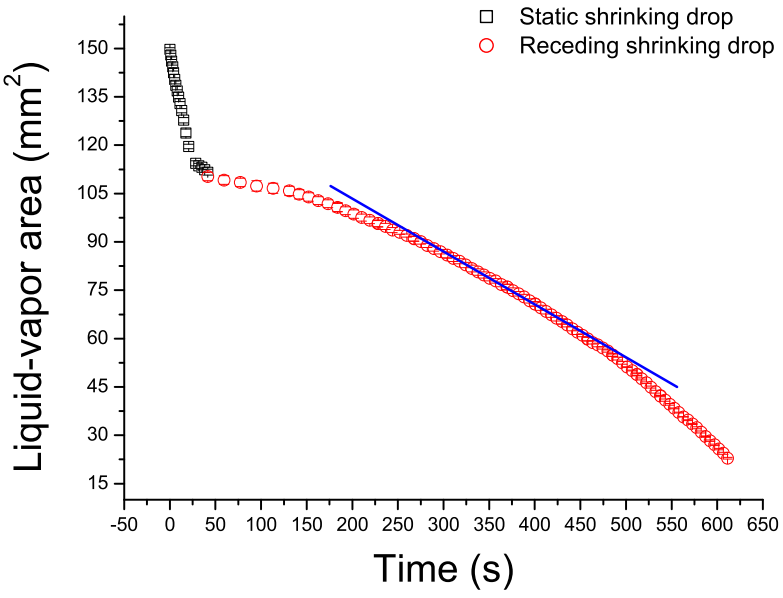

(b) Liquid-vapour area in terms of time

Figure 3.11: CSSD experiment of Milli-Q water on a PMMA surface. We illustrate the linear behaviour of the liquid-vapour area with a blue straight line.

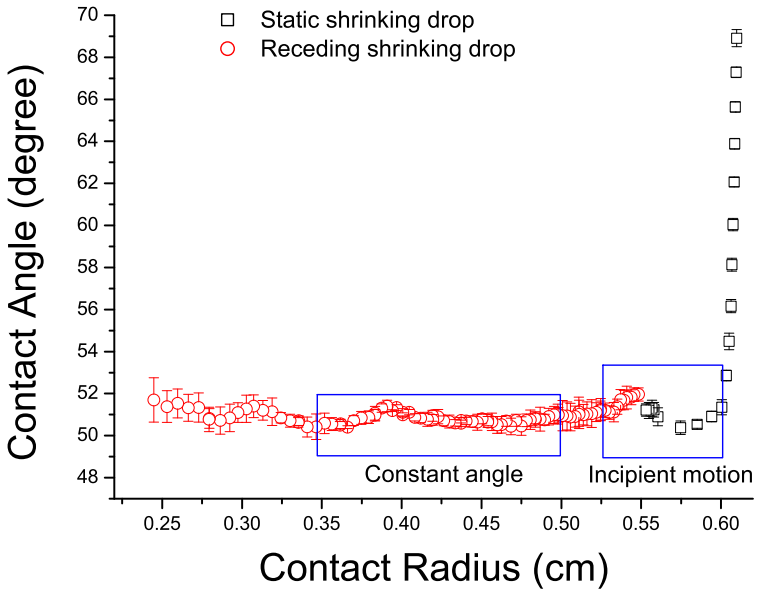

Figure 3.12: Contact angle in terms of contact radius in a CSSD experiment of Milli-Q water on a PMMA surface.

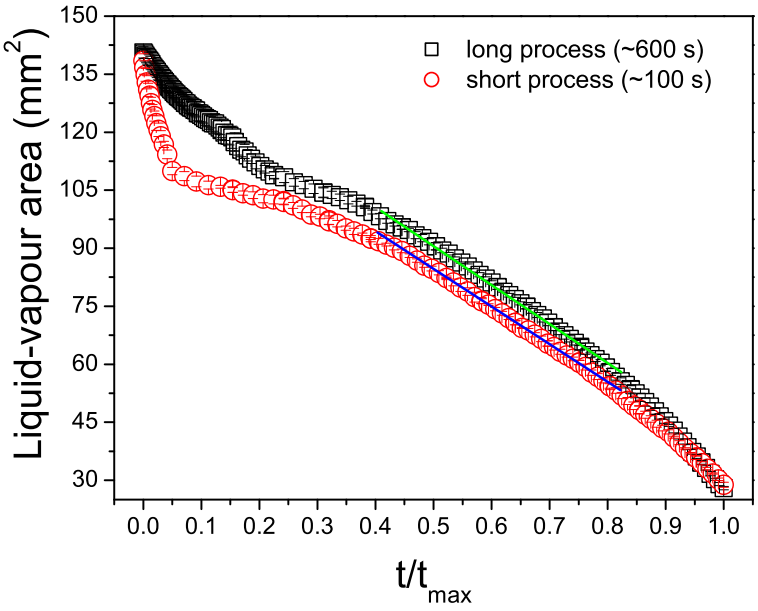

(a) Liquid-vapour area in terms of normalized time

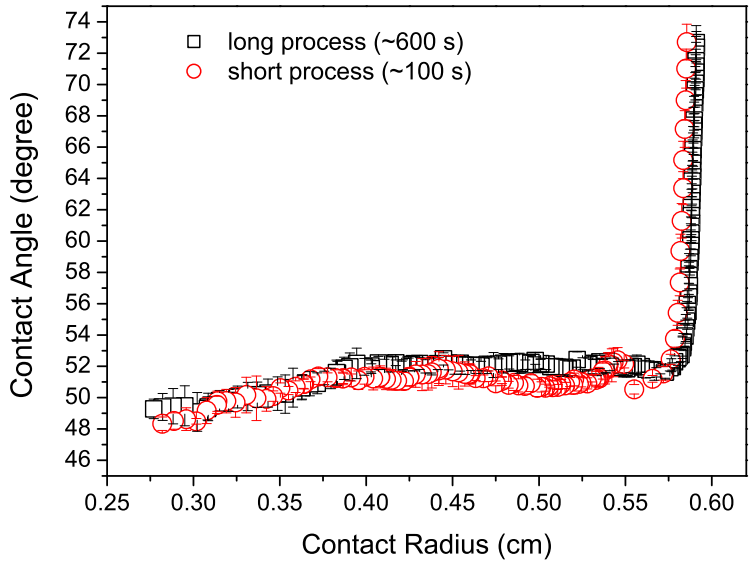

(b) Contact angle in terms of contact radius

Figure 3.13: CSSD experiments of Milli-Q water on a PMMA surface for two different times t_t: 100s and 600s. We illustrate the linear behaviour of the liquid-vapour area with blue and green straight lines for each experiment.

CHAPTER 4

Conclusions

Receding contact lines of pure liquids

In this work, we focused on the dynamics of three-phase contact line at very low capillary numbers. In this scenario, the observed contact angle should be speed-independent. However, we found that the quasi-static contact angle at moving contact lines of shrinking drops depended on the volumetric flow rate. We were able to measure stable, minimum values of receding contact angle with quadratic flow rate. This behaviour points out to a hysteresis effect rather than a viscous effect. We recommend, whenever possible, to perform a preliminary study on the impact of the drop preparation and drop size on the receding contact angle measurement.

With the methodology developed in this part, we are able to control the speed of the receding contact lines and further to emulate the first stages of drop evaporation. The drop volume was changed by removing liquid to a initial drop using a motorized-micrometer syringe. Contact line dynamics of shrinking drops was then controlled by regulating the volume flow rate. We were able to reproduce the linear decrease of liquid-vapour area with time of evaporating drops using a non-linear withdrawal of liquid volume. Unlike freely-evaporating drops of pure liquids, the receding contact lines of shrinking drops mostly held a constant contact angle over a significant area. The

internal flux distribution imposed, included the flow produced by the eventual microevaporation at the triple line, was the same for all experiments, once fixed the initial drop volume, the process length and the substrate (contact angle hysteresis). This way, the Controlled Shrinking Sessile Drop (CSSD) method allows standardizing the contact line dynamics of evaporating drops.

English

Next, we summarize the main conclusions of the part I of this work:

1 Quadratic volumetric flow rate in low-rate dynamic contact angle experiments enables the steady motion of contact lines of sessile drops, which standardizes the input of kinetic energy to driven contact lines. This strategy applies to a wide range of polymer surfaces. Further work should be addressed to the systematic use of quadratic flow rate in low-rate dynamic contact angle experiments.

2 Receding contact angle values measured at steadily moving contact lines are time- and speed-independent. This enables to map significantly the surface energetics over the substrate.

3 Receding contact angle of a sessile drop on certain surfaces dependes on how the drop was formed. Larger initial drops and a previous withdrawal of liquid enables the early receding motion for shrinking drops. This allows to evaluate the minimum observable value of receding contact angle, independent of the drop placement.

4 The overall process (including the mix stage) of liquid drop evaporation has been reproduced successfully using a no-linear variation of drop volume.

Español

A continuación, resumimos las principales conclusiones de la parte I de este trabajo:

1 Un ritmo volumétrico quadrático en experimentos de ángulo de contacto dinámico facilitan el movimiento uniforme de línea de contacto de gotas sésiles, lo que estandariza la entrada de energía cinética a la línea guiada. Se debería estudiar en profundidad el uso sistemático de ritmos volumétricos quadráticos en experimentos de ángulo de contacto dinámico.

2 Los ángulos de contacto de retroceso medidos en líneas de contacto en movimiento uniforme are independientes de la velocidad y del tiempo. Esto permite mapear significativamente la energía superficial del sustrato.

3 El ángulo de contacto de retroceso de una gota sésil sobre determinadas superficies depende de cómo se formó la gota. Gotas voluminosas y una succión previa de líquido facilitan el movimiento temprano en retroceso de gotas "menguantes". Esto permite evaluar el valor observable mínimo del ángulo de contacto de retroceso, con independencia de la colocación de la gota.

4 El proceso global (incluyendo la etapa mixta) de evaporación de gotas sésiles se ha reproducido con éxito utilizando una variación no lineal de volumen de gota.

Part II

Receding contact lines of complex liquids

CHAPTER 5

Theoretical framework

Receding contact lines of complex liquids

5.1 Coffee stain effect

When a coffee drop evaporates on a solid surface, a ring-like deposit is left along the perimeter. If the liquid contains particles, like in a suspension, these particles will be driven outwards by the flow. When all the liquid has evaporated, the particles will form a ring or stain (see Figure 5.1). Morphology of the particle deposits varies in extensively manner (see Figure 5.2), aside from ring-like structures (5), they can exhibit a central bump (119), uniform deposit (120) or complex patterns involving multiple rings (121), network of polygons or hexagonal arrays (122). Diversity in morphology deposits is due to the complex mechanism behind the transport of particles phenomena during drop evaporation.

The mechanism for particle deposits and the morphology of the deposits left has been widely studied. The first study proposing a physical model was the published by Deegan et al (6). They demonstrated that exist two conditions necessaries for ring-like deposits apparition: contact line pinning and evaporation from the edge of the drop. They showed that the particle migration is

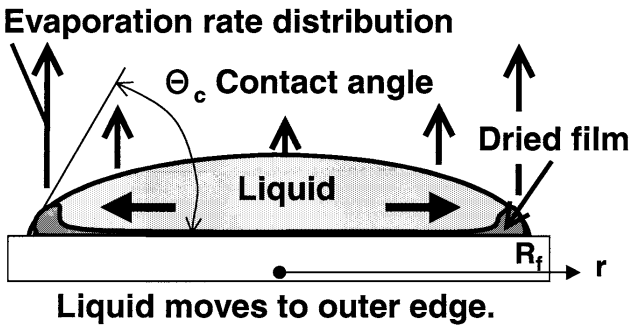

Figure 5.1: Drying of a sessile drop of a complex liquid.

caused by an outward flow within the drop that is driven by the loss of solvent by evaporation. Furthermore, they also noticed that the nonuniform evaporation draws energy unevenly from the drop, creating temperature gradients and consequently the flow field is affected by surface tension gradients, i.e., Marangoni flows. This flow creates a shear stress that drags fluid along the interface, setting up re-circulating flows. The gradients of surface tension can be produced by temperature gradients or solute concentration gradients along the drop surface. Marangoni flow during drop evaporation can control deposition patterns (30, 37, 126). It has been reported (127) that the ratio between the substrate and drop thermal conductivities controls the direction of Marangoni convection inside an evaporating drop, with a direct effect on the deposit pattern.

How to control particle deposition has been extensively studied, for example, it has been shown for evaporating jetted drops (120) that varying the chemical composition of the ink, the deposit morphology can change from a ring to a uniform two-dimensional monolayer with a well-ordered hexagonal structure. Denkov et al. (128) found that during the last stages of the evaporation, capillary forces are responsible for the ordering of the particles. The effect of the substrate wettability on the particle deposition speed toward the contact line has also been studied (129). Recently, Marin et al. (28) found that a transition from ordered, crystalline arrays to disordered packings arises from a temporal speed up of the particle motion near the end of the evaporation: "the rush-hour effect".

The contact line of evaporating drops of colloidal suspensions is pinned due to the accumulation of colloidal particles forming a topographic barrier (a solid ring). This ring can perpetuate the pinning of the contact line or either produce the jump of the contact line, according to the wettability contrast between particle and substrate. Hence, self-pinning is always enhanced when the colloids are more wettable than the surface. Multiple rings can result from the stick-slip behaviour of receding contact lines.

Previous studies (130) demonstrated that the particle size and receding contact angle of the

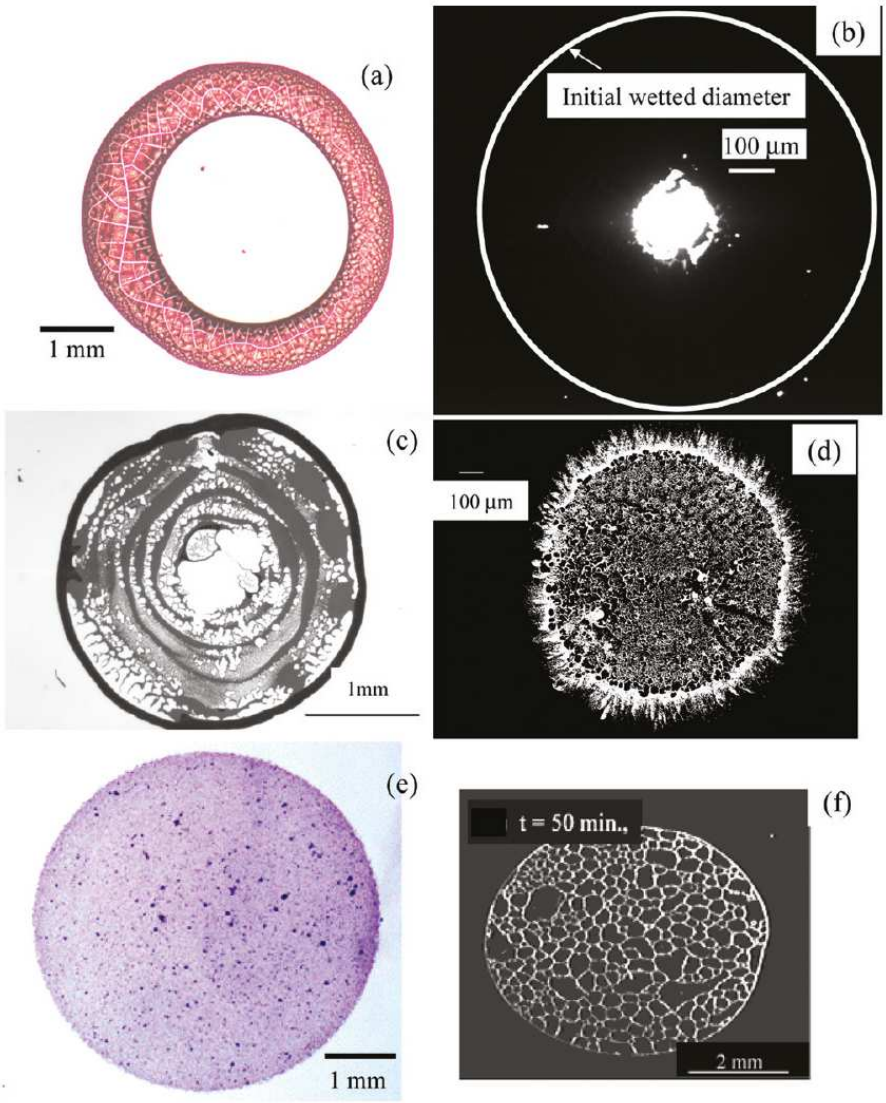

Figure 5.2: Different deposits obtained after drying drop of particle suspension: (a) ring-like pattern from an aqueous drop containing 60 nm polystyrene spheres on titanium substrate (3); (b) central bump obtained after the drying of a 38 nL isopropanol drop on PDMS(123); (c) multiple rings from a microliter water drop containing 1μm polystyrene microspheres on glass (119);(d) fingering at contact line obtained from a microliter isopropanol drop with 1μm polystyrene microspheres on glass (119); (e) uniform deposition pattern of 60 nm hydroxyapatite particles from an aqueous drop on titanium disk (124); (f) hexagonal cells from a surfactant-laden aqueous drop containing polystyrene microspheres on a substrate modified by octadecyltricholorosilane (125).

substrate, determine the distance away from the contact line where particles get deposited, which determines the final deposition morphology of particles. Chhasatia et al. (131) found that with the change in substrate wettability significant differences are created in the microflow patterns inside the drop, resulting in different particle dynamics and deposit morphologies.

As explained before, the deposition of colloidal particles from an evaporating droplet onto a substrate depends on the flow profile that is induced inside the evaporating droplet. Under different evaporation conditions, fluid can either flow toward or away from the contact line. When the evaporative flux of liquid is relatively constant across the droplet or moderately enhanced at the edge of the droplet (hydrophilic surfaces), an outward flow develops in the liquid. This outward flow convects the solute toward the contact line, leading to the development of a solute ring on the substrate. Conversely, if evaporation primarily occurs at the center of the droplet (hydrophobic surfaces), then a solute ring does not form because the liquid flows toward the center of the droplet. Rather, a uniform deposit of particles remained on the substrate.

Siddhartha et al. (132) studied the electrokinetic effects on the particle deposition. They found that, electrokinetic-effect induced (as a consequence of evaporation of an electrolyte drop in contact with a charged substrate) enhancement the deposition velocity at the end of the drop lifetime may lead to a drastic increase of the disordered phase deposition velocity, modulating the consequent "coffee stain" effect to a significant extent.

The role of DLVO interactions on the morphology of the particle deposits has been investigate by Bhardwaj et al. (37). They found that there are three convective patterns that cause the different particle deposits. A peripheral ring is obtained due to the radial flow created by the maximum evaporation rate at the contact line. A uniform layer is formed when the transport of particles normally toward the substrate occurs due to an attractive DLVO force. A central bump is created with Marangoni recirculation loop.

On the other hand, the "coffee stain" effect produces a undesired inhomogeneous distribution of solutes. In applications such as microarrays, coating and printing, the inhomogeneity of the residual deposits compromises the overall performance of the system. In this way, many studies have been developed in order to reverse or mitigate the "coffee ring" effect. Eral et al. (33) found that the stains of colloidal particles can be suppressed by electrowetting at alternating frequencies ranging from a few Hz to a few tens of kHz. The effects that contribute to the suppression of the "coffee stain" effect are: the time-dependent electrostatic force which prevents the pinning of the contact line and the internal flow fields generated by the AC electrowetting prevents the accumulation of particles along the contact line. Yunker et al. (32) found that the shape of the suspended particles can be used to eliminate the coffee-ring effect. The ellipsoidal particles are deposited uniformly during evaporation. They also found that under appropriate conditions, suspensions of spheres mixed with a small number of ellipsoids produce uniform deposition. Therefore, adding

ellipsoids to existing suspensions, uniform depositions can be produced.

5.2 Derjaguin, Landau, Verwey and Overbeek interactions

The van der Waals and electrostatic forces do affect the colloidal systems, but most previous studies on the evaporating droplet did not consider the effects. There are just a few works devoted to study the effects of the interparticle interaction and particle-substrate interaction (24, 126, 131, 133).

Figure 5.3 shows schematically the various types of interaction potentials that can occur between two similarly charged surfaces or colloidal particles in a 1:1 electrolyte solution under the combined action of the van der Waals and electrostatic forces (134). Depending on the electrolyte concentration and surface charge density or potential one of the following may occur:

- For highly charged surfaces in dilute electrolyte, there is a strong long-range repulsion that peaks at some distance.
- In more concentrated electrolyte solutions there is a significant secondary minimum. The potential energy minimum at contact is known as the primary minimum. For a colloidal system, even though the thermodynamically equilibrium state may be with the particles in contact in the deep primary minimum, the energy barrier may be too high for the particles to overcome during any reasonable time period. When this is the case, the particles will either sit in the weaker secondary minimum or remain totally dispersed in the solution. In the latter case the colloid is referred to as being kinetically stable (as opposed to thermodynamically stable).
- For surfaces of low charge density or potential, the energy barrier will be lower. This leads to slow aggregation, known as coagulation or flocculation. Below a certain charge or potential, or above some concentration of electrolyte, known as the critical coagulation concentration, the energy barrier falls below the $W = 0$ axis (middle curve in Figure 5.3) and the particles then coagulate rapidly. The colloid is now referred to as being unstable.
- As the surface charge or potential approaches zero the interaction curve approaches the pure van der Waals curve, and two surfaces now attract each other strongly at all separations.

The surface potential of spherical particles (ψ_p) can be related to the surface charge density (σ_p) by the Gouy-Chapman relation (135):

$$\sigma_p = \frac{2\varepsilon\varepsilon_0 k_B T}{e\kappa^{-1}} \sinh\left(\frac{e\psi_p}{2k_B T}\right) \tag{5.1}$$

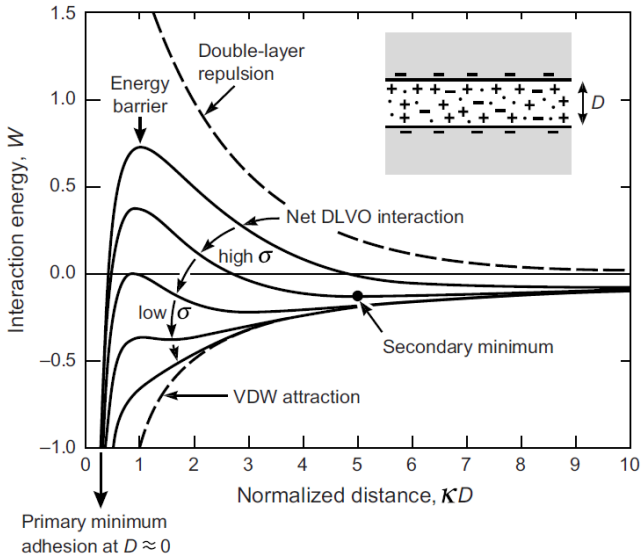

Figure 5.3: Schematic energy versus distance profiles of the DLVO interaction. The actual magnitude of the energy W is proportional to the particle size (radius) or interaction area (between two planar surfaces) (134).

where $\varepsilon\varepsilon_0$ is the total permittivity of the water, k_BT the Boltzmann constant, T the absolute temperature, e the electronic unit charge, and κ^{-1} the Debye length, which is the thickness of the diffuse electric double layer and is defined as:

$$\kappa^{-1} = \sqrt{\frac{\varepsilon\varepsilon_0 k_B T}{2N_A e^2 I}} \tag{5.2}$$

with N_A the Avogadro number and I the ionic strength of dispersant, which is defined as:

$$I = \frac{1}{2}\sum_{i=1}^{n} Z_i^2 C_i \tag{5.3}$$

where Z_i is the valence of the ions and C_i the concentration of the dissolved ions.

Colloidal particles in an evaporating drop experience van der Waals and electrostatic interactions with other particles, as well as with the substrate near the contact line. For a colloidal evaporating drop on a substrate, the total DLVO force between a particle and the substrate can be calculated as the algebraic sum of the electrostatic and van der Waals forces:

$$F_{DLVO} = F_{el} + F_{vdW} \tag{5.4}$$

The particle-substrate electrostatic force is calculated as:

$$F_{el} = F_{el}\,(0)\exp(-z/\kappa^{-1}) \tag{5.5}$$

where, κ^{-1} is the Debye length (eq. 5.2) and z the distance between the particle and the substrate. The electrostatic force at zero distance depends on the temperature, the particle diameter and the surface potentials of the particle and the substrate.

The van der Waals attraction force between the substrate and the particle is given by (135):

$$F_{vdW} = \frac{1}{12} A d_p^3 \frac{\alpha_{rtd}}{z^2\,(z+d_p)^2} \tag{5.6}$$

where A is the Hamaker constant and d_p is the particle diameter. Although particle and substrate were likely charged, if the particles get very close to the substrate then the short-range attractive forces become significant.

Unlike the double-layer (electrostatic) interaction, the van der Waals interaction potential is largely insensitive to variations in electrolyte concentration and pH, and it can be considered as fixed in a first approximation. Further, the van der Waals attraction must always exceed the electrostatic repulsion at small enough distances (D) since it is a power law interaction (i.e., $W \propto -1/D^n$), whereas the double-layer interaction energy remains finite or rises much more slowly as D$\rightarrow$0.

However, when two surfaces or particles approach closer than a few nanometers, continuum theories of attractive van der Waals and repulsive double-layer forces often fail to describe their interaction. This is either because one or both of these continuum theories breaks down at small separations or because other non-DLVO forces come into play. These additional forces can be monotonically repulsive, monotonically attractive, or oscillatory, and they can be much stronger than either of the two DLVO forces at small separations. There are also non-DLVO forces that are due to surface-adsorbed polymers or to surface-specific (rather than solvent-specific) interactions. Solvation forces depend not only on the properties of the intervening liquid medium but also on the chemical and physical properties of the surfaces for example, whether they are hydrophilic or hydrophobic, smooth or rough, amorphous or crystalline (atomically structured), homogeneous or heterogeneous, natural or patterned, rigid or fluid-like. These factors affect the structure that confined liquids adopt between two surfaces, which in turn affects the solvation force.

Alike several authors (37), the non-DLVO forces acting on the substrate-particle system will be neglected in this work.

CHAPTER 6

Materials and techniques

Receding contact lines of complex liquids

The formation and the morphology of particle deposits are largely dependant on the properties of the particles and the substrate. The properties of particle suspensions such as size (136), volume fraction (137), hydrophilicity/hydrophobicity (138) and surface electrical charge (37) can further the occurrence or the mitigation of the self-pinning of contact line (139) and the own deposition over the substrate. Otherwise, the contact angle hysteresis and the surface electrical charge of the substrate also affect the deposit formation and its morphology.

Due to the relevance of the particle properties in the coffee stain effect, in this chapter we analyzed the following properties of the different types of particle suspensions used in this work: particle diameter, electric state, colloidal stability, viscosity, wettability of particles and surface tension. Over the substrates used for the deposit formation, we measured the roughness and the contact angle hysteresis. The electrical state of the substrates was estimated from particle electrophoretic mobility measurements. For these purposes, a wide set of techniques was employed and the results obtained are compiled below.

6.1 Particles

We used in this work commercial aqueous suspensions of spherical particles, which are collected in Table 6.1. In our CSSD experiments (see Section 2.5), we formed large sessile drops of suspension (200μl) at moderately high concentrations ($\Phi_V \geq 1\%$)[a]. These experimental conditions restricted the use of ad hoc synthesized suspensions, usually delivered in small amounts. We purchased polymeric particles (polystyrene, polymethylmethacrylate) and metal oxide particles (silica, titanium oxide). The metal oxide particles were delivered without customized surface functionalization except for the aminated silica. The maximum concentration of these suspensions was $\Phi_V = 5\%$. We also used suspensions of silica particles concentrated up to $\Phi_V \geq 17.5\%$, kindly supplied by Klebosol. The particle suspensions were diluted in buffer solutions by dialysis for CSSD experiments.

Dialysis is the movement of molecules by diffusion from high concentration to low concentration through a semi-permeable membrane. Molecules that are smaller than the membrane pores are able to move through the membrane and reach equilibrium with the total volume of the solution in the system. A sample of 10 ml of particle suspension was dialyzed against 1 l of buffer solution for 5 h and next, the buffer solution was exchanged two times. We used a dialysis tubing cellulose membrane (D9652, Sigma Aldrich) with a size pore in the range of 1-2nm.

Material	**Acronym**	**Manufacturer**	**Max. $\Phi_V(\%)$**	**Density (g/cm^3)**
Silica	SiO2-120nm	Microparticles	2.5	2
Silica	SiO2-1.16μm	Microparticles	2.5	2
Poly(methyl methacrylate)	PMMA	Microparticles	5	1.19
Aminated Silica	SiO2-NH2	Microparticles	1	2
Silica	SiO2-20nm	Klebosol	17.5	2.01
Silica	SiO2-90nm	Klebosol	33	2.01
Silica	SiO2-50nm	AttendBio Research	1.25	2
Polystyrene	PS	AttendBio Research	2.5	1.05
Titanium oxide	TiO2	Sigma Aldrich	30	1.3

Table 6.1: Particles used in this work with their acronym, manufacturer, maximum volume fraction and density.

6.2 Particle diameter

After the drying of colloidal suspensions or for the 2D colloidal assembly by convective deposition, the particle size will modify the morphology of the final pattern (10). It is reported that small

[a] Φ_V will represent the particle volume fraction in all the text.

particles may be readily arranged at the vicinity of contact lines rather than larger particles due to the "wedge" shape of the solid-liquid-air interfacial region (hydrophilic substrates). Hence, as reported in literature (136, 140), small particles usually form rings near the drop edge whereas the larger particles show the opposite behavior (see Figure 6.1).

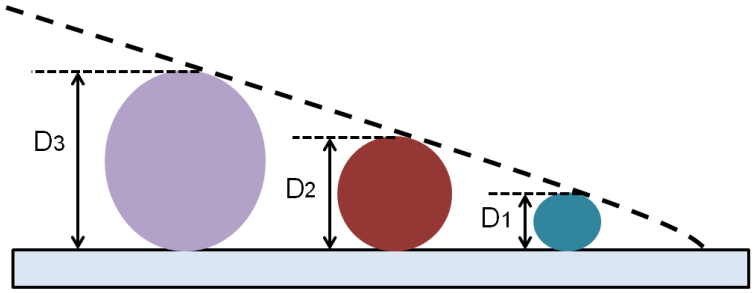

Figure 6.1: Sketch of the particles deposition at the interfacial "wedge"as the particle diameter.

In order to characterize the size of the particles used in the present work, we used a high performance particle sizer (ALV), which utilizes a well-established technique known as Non-Invasive Back Scattering (NIBS). This technique enables measuring the diameter of particles typically in the submicron scale (1nm-5μm particle diameter) and at high concentrations ($1 \times 10^{-4} - 5\%$ W/W).

Mesoscopic particles are continuously moving due to their thermal energy (Brownian motion), in consequence their diffusion velocity can be measured. For this purpose, the particles are illuminated with a laser beam ($\lambda = 632.8$ nm). The intensity of the scattered light fluctuates at a rate that is dependent on the diameter of the particles. Thus, small particles cause the intensity to fluctuate more rapidly than the large ones. Analyzing the intensity fluctuations, the diffusion coefficient of the particles due to the Brownian motion can be calculated. Finally, the particle diameter is computed from the Stokes-Einstein equation. The diameter measured is called hydrodynamic diameter and it refers to how a particle diffuses within a liquid.

The experiments were performed with particle suspensions diluted in Milli-Q water at a concentration of $\Phi_V = 1\%$. The diameters of the particles used in this work are shown in Figure 6.2.

6.3 Electric state

It is known that particle-particle and substrate-particle electrostatic interactions have a great relevance in the deposit patterns (37). The particle arrangement over the substrate is greatly mediated by DLVO interactions (see Section 5.2). For the cases of colloidal assemblies, the main

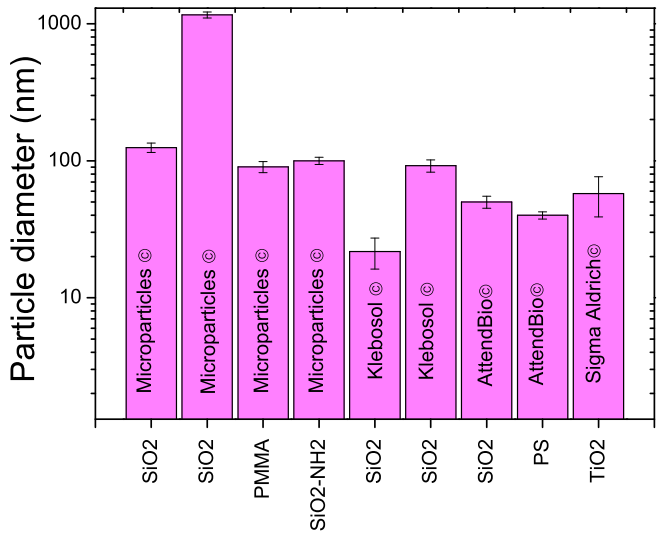

Figure 6.2: Diameter of the particles used in this work (log scale). The supplier/manufacturer of particles is written in each column. The size measurements were performed at $\Phi_V = 1\%$.

driving force lies in electrostatic attraction between colloidal spheres and substrates with opposite charges (141). Thus, controlling DLVO interaction, different assemblies of colloidal particles on arbitrary substrates can be obtained.

Particles in aqueous suspension acquire surface electrical charge due to surface ionization and/or adsorption of charged species. To quantify the surface electric state of colloidal suspensions, the zeta potential is usually employed. Zeta potential is an estimate of surface electrical potential and it is usually estimated from electrokinetic measurements (142).

When an electric field is applied across the dispersion, the particles migrate toward the electrode of opposite charge with a velocity proportional to the magnitude of the zeta potential. This velocity divided by the field strength is the electrophoretic mobility. Using the medium viscosity and the particle size, the zeta potential is calculated from the electrophoretic mobility and the application of the Smoluchowski or Hückel approximations, accordingly (142). Usually, zeta potential of particle suspensions is assumed low when it takes a value lower than 25 mV (thermal voltage).

We measured the electrophoretic mobility using a Zetasizer Nano (Malvern). This device uses Phase Analysis Light Scattering (PALS). Firstly, a laser beam is used to illuminate the particles within the sample. Then the incident laser beam passes through the sample and the scattered light is detected. When the electric field is applied to the suspension, the particles movement causes a fluctuation on the light intensity with a frequency proportional to the particle velocity due to the Doppler effect.

With the purpose of finding the optimal concentration of particle suspension for electrophoretic mobility measurements, we prepared particle suspensions with different concentration ranging from $\Phi_V = 1 \times 10^{-4}\%$ to 0.1%. The optimal concentration was found when particle electrophoretic mobility "saturated", regardless of the particle concentration. We used a concentration above this optimal value in order to assure that the electrophoretic mobility results obtained were not dependent of particle concentration. The results of particle electrophoretic mobility as a function of particle concentration are shown in Figure 6.3 for the SiO2-90nm particles diluted in Milli-Q water. This was repeated for the rest of particle suspensions. Finally, all the particle suspensions were diluted at a concentration of $\Phi_V = 0.01\%$.

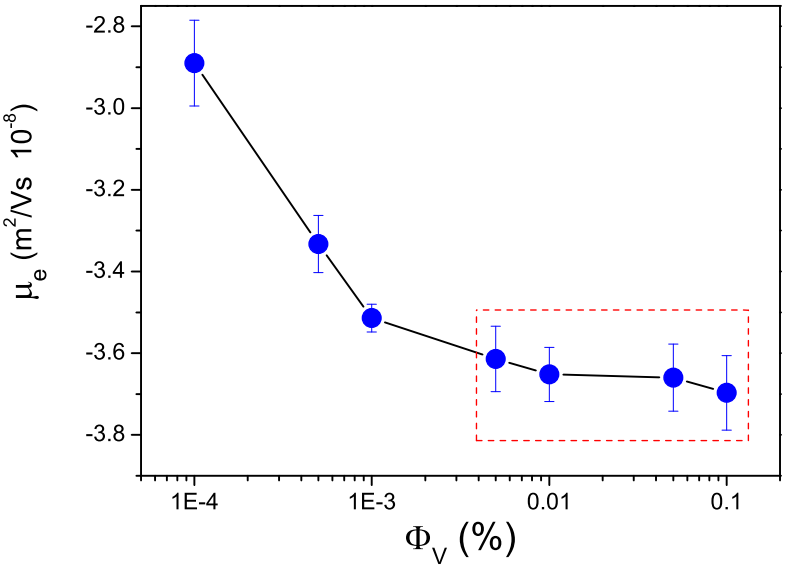

Figure 6.3: Electrophoretic mobility of SiO2-90nm particles as function of particle concentration. When the electrophoretic mobility saturated, we found the optimal concentration for electrophoretic mobility measurements.

In order to modulate the electrostatic particle-particle interactions, we changed the particle electrical charge by means of the medium pH. Thus, the particle suspensions were prepared by diluting particles in buffer solutions of low ionic strength ($\leq$ 15mM). A buffer solution is an aqueous solution consisting of a mixture of a weak acid and its conjugate base or a weak base and its conjugate acid. This composition enables the stabilization of the medium pH. We prepared suspensions with pH value ranging from 2 to 10. The chemical compounds used in each buffer solution are listed in Table 6.2. In order to obtain the precise pH value, a small amount of NaOH was added. The contribution to the ionic strength of this amount was negligible (2-3 magnitude orders smaller) compared with the contribution of the reactant used for each case.

We measured the particle electrophoretic mobility as a function of pH value for all the types of particles used in this work (see Table 6.1), at concentration of $\Phi_V = 0.01\%$. The results are

pH	Chemical compounds	Concentration (mM)
2	HNO_3	0.1*
3	HNO_3	0.017*
4	AcH (CH_3COOH)	13.5
5	AcH (CH_3COOH)	3.15
6	NaH_2PO_4	1.79
7	NaH_2PO_4	1.13
8	H_3BO_3	15
9	H_3BO_3	5.14
10	H_3BO_3	2.2

*The cases of pH2 and 3 were not buffer solutions because their pH value was just reached by adding small quantities of HNO_3.

Table 6.2: Chemical compounds and their concentrations used for the preparation of buffer solutions with different pH values.

shown in Figure 6.4. Although most of the particles were negatively charged for all the pH values studied, SiO2-NH2 and TiO2 particles revealed positive charge in a pH range from 2 to 5.

We were interested to know, from the electrophoretic mobility measurements, the isoelectric point (IEP) of each type of particle. The IEP is the pH value at which the zeta potential passes through zero (i.e. the particle is electrically uncharged). From the results obtained in Figure 6.4, as expected, we found that the IEP for SiO2 particles was pH2, for TiO2 particles was pH5.5 and for SiO2-NH2, pH9. Silica particles are covered by Si-OH units (silanol). The silanol groups are acidic, which corresponds to an IEP $\approx$ 2. Instead, TiO2 particles contain abundant TiOH groups on their surface. TiOH groups are acidic in alkaline solution and basic in acidic solution. The electrophoretic mobility results for the polymeric particles revealed negative zeta potential in all the range of pH values studied but, for the PMMA particles, the weakest particle-particle electrostatic interactions were obtained at pH2. However, the electrical charge of the PS particles remained constant as pH was changed and in adittion, the interparticle interactions were highly repulsive.

6.4 Colloidal stability

Evaporation-mediated assembly of colloidal particles is successful if, previously, the particles are homogeneously dispersed without any phase separation. Colloidal suspensions are intrinsically unstable systems. If the rate of destabilization is low enough compared with the laboratory scale time periods, then the suspension can be considered as kinetically stable (143). The destabilization mostly occurs due to two physical phenomena:

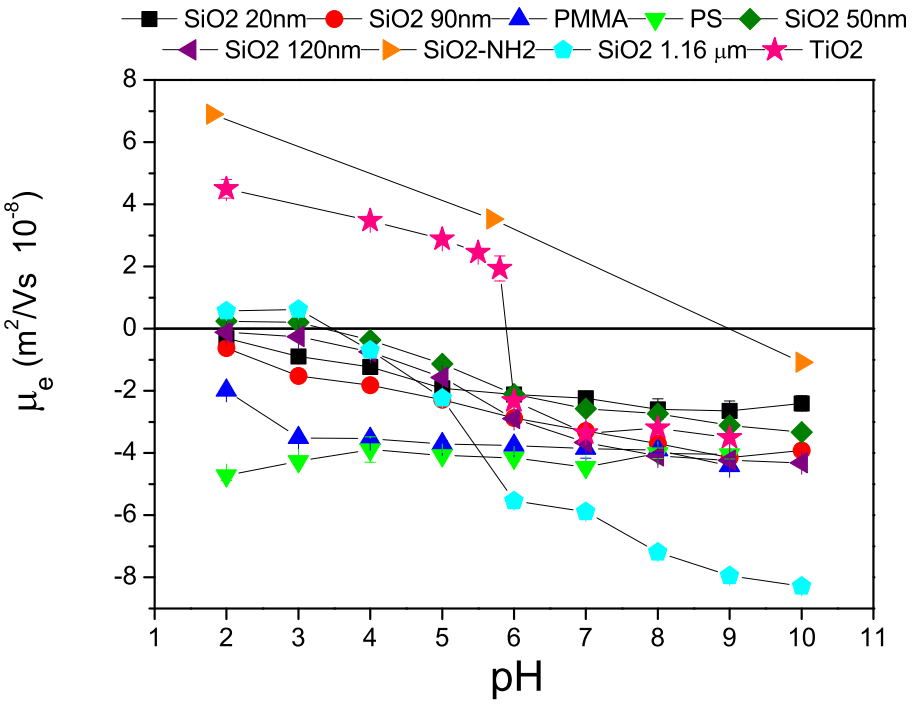

Figure 6.4: Particle electrophoretic mobility as a function of pH value of all the particles used in the present work. The electrophoretic mobility measurements were performed at $\Phi_V = 0.01\%$

i. Particle diameter increase (coalescence) or particle aggregation (flocculation).

ii. Particle migration (creaming or sedimentation).

Even although creaming and sedimentation are often considered as reversible phenomena, coalescence and flocculation are usually irreversible.

Since the particle size of the suspensions studied was mostly small (minor than 130 nm [b]), sedimentation or creaming did not occur for our experimental time scale [c] due to the particle Brownian motion and the electrostatic interactions between particles. We focused on those suspensions where electrostatic interactions were minimized. To study the colloidal stability of these suspensions, the electrophoretic mobility (see Section 6.3) and particle size (see Section 6.2) were monitored.

As described in Section 6.3, particle electrophoretic mobility is a function of particle velocity, which depends on the particle diameter. For this reason, we measured particle electrophoretic

[b] In the case of SiO2 particles greater than 1μm, sedimentation was expected to occur independently of pH. These particles were only used to monitor the drop evaporation with optical microscopy (see Section 8.1)

[c] The maximum experimental time was about 630s.

mobility as a function of time in order to know if particle diameter changed during a CSSD experiment. For this purpose, we prepared suspensions at pH2 where the particle-particle electrostatic interactions were minimal, except for the PS, TiO2 and SiO2-NH2 particles (Figure 6.4). A weakly charged system has more probability to aggregate than a highly charged system. If the particle electrophoretic mobility remained constant in time for those systems with minimized electrostatic interactions, then the particle aggregation was not significant.

We measured electrophoretic mobility in terms of time for particles of PMMA, SiO2-50nm and SiO2-120nm at pH2 and a concentration of $\Phi_V = 0.01\%$. Electrophoretic mobility was measured every 3 min for 30 min. The results are shown in Figure 6.5. From these results, we concluded that no particle aggregation occurred when the particle-particle electrostatic interactions were minimized. It is worth mentioning that, in this study, the suspensions were much more dilute ($\Phi_V = 0.01\%$) than in CSSD experiments ($\Phi_V \geq 1\%$).

In order to verify the occurrence of particle aggregation for concentrated suspensions, we measured the particle diameter as function of time for SiO2-50nm, SiO2-120nm, PMMA and PS suspensions diluted in Milli-Q water and buffer solutions at pH2, pH9 and $\Phi_V = 1\%$. The particle size was monitored with the high performance particle sizer (ALV) every 5 min for one hour. The final sizes are shown in Figure 6.6. From these results, we concluded that particles did not aggregate for at least one hour, even if the particle-particle electrostatic interaction was weak.

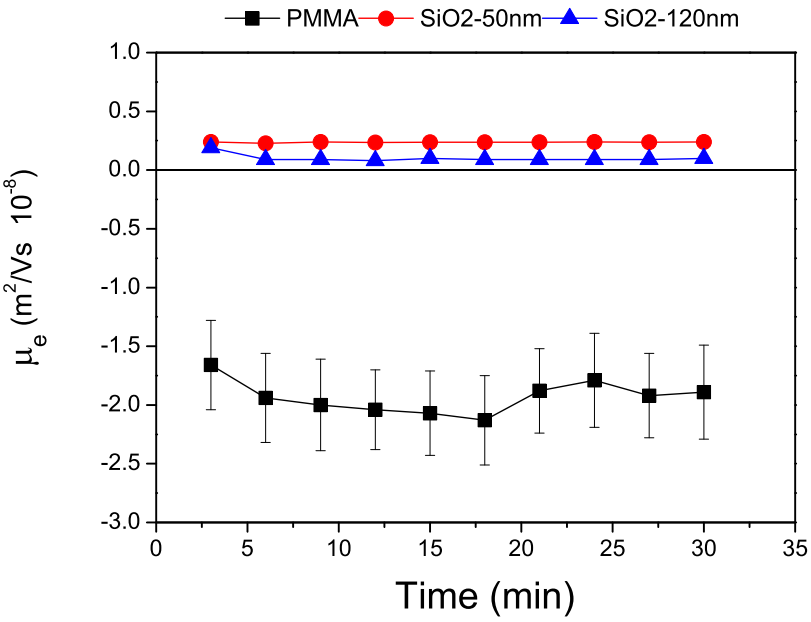

Figure 6.5: Particle electrophoretic mobility as function of time for the particles of PMMA, SiO2-50nm and SiO2-120nm buffered at pH2 and $\Phi_V = 0.01\%$. At this pH value, the electrostatic interparticle interactions were weak.

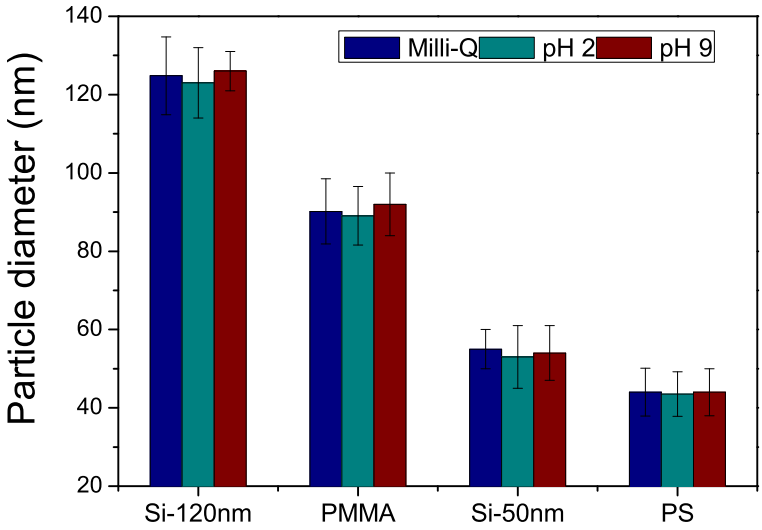

Figure 6.6: Particle diameter of the SiO2-120nm, PMMA and PS particles diluted in Milli-Q water and in buffer solutions at pH2 and pH9, $\Phi_V = 1\%$, after one hour.

To test sedimentation phenomena, we used an optical analyzer TURBISCAN MA 2000. The measurement principle of this device is a detection head which moves up and down along a flat-bottomed cylindrical cell. The detection head is composed of a pulsed near-infrared light source (λ=850 nm) and two synchronous detectors. The transmission detector receives the light which goes across the sample (at 180° from the incident beam), while the backscattering detector receives the light scattered backward by the sample (at 45° from the incident beam). The detection head scans the entire length of the sample (about 65 mm) acquiring transmission and backscattering data each 40 μm (1625 transmission and backscattering acquisitions per scan). Results are represented by a curve showing the percentage of backscattered or transmitted light as a function of the sample tube length (in mm).

We measured the backscattering and transmission percentages (see Figure 6.2) through the suspension of the largest and heaviest particles (see Table 6.1) with the weakest electrostatic particle-particle interaction that we used for CSSD experiments (see Section 8.2). This choice was taken as the worst-case situation. If this suspension is stable against sedimentation, we assure that the rest of suspensions are also stable in CSSD experiments. We prepared a suspension of SiO2-120nm particles buffered at pH2 and a concentration of $\Phi_V = 1\%$. We measured backscattering and transmission percentages every second for one hour. The results are shown in Figure 6.7. To neglect the effects caused by the the upper and lower sample limits, we took the results from 5 to 27.5 mm (limited by red lines in Figure 6.7). Both signals remained constant along the sample tube for one hour. Hence, we concluded that no particle sedimentation occurred for one hour.

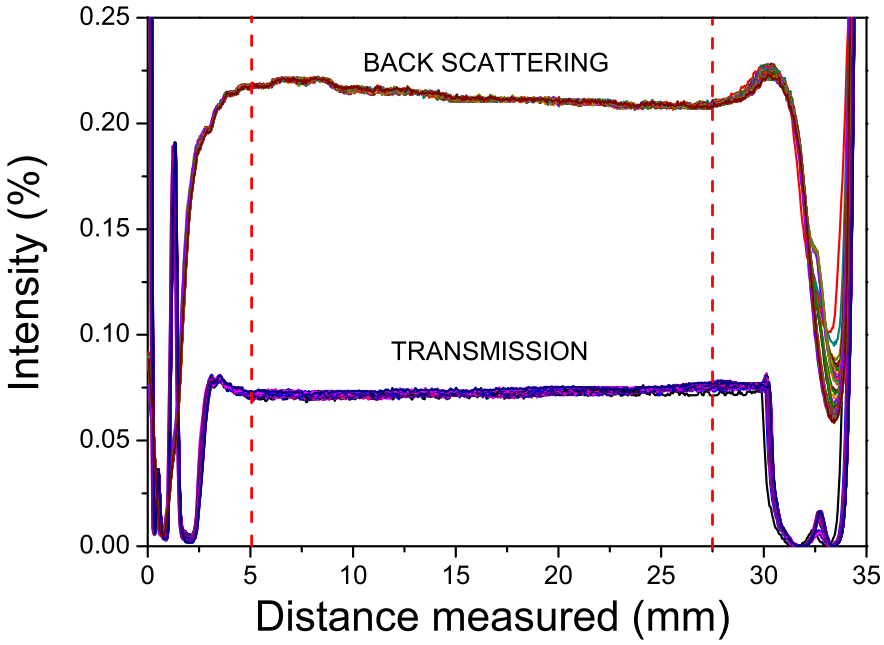

Figure 6.7: Backscattering and transmission percentages measured for one hour through a suspension of SiO2-120nm particles buffered at pH2 (with the weakest electrostatic interaction) and $\Phi_V = 1\%$. The different colours for each case refer to different time periods.

6.5 Viscosity

Advancing and receding contact angles may be affected by the viscosity of the liquid (108). In the case of liquids with low viscosity, surface forces are dominant and the contact angles are not dependant of the motion rates of the three-phase contact line (see Section 1.1.4). For liquids with high viscosity, an increment of the rate of motion causes the advancing contact angle to increase and the receding contact angle to decrease.

In order to study if the contact angle measured in CSSD experiments was affected by the viscosity of the particle suspensions, rheology experiments were carried out in a MCR 501 magneto-rheometer (Anton Paar) with a parallel plate configuration at room temperature. We used a glass plate with 40 mm diameter. To calibrate the rheometer, we used silicone oil (Sigma-Aldrich) with a well known viscosity (20mPa s at room temperature). The viscosity of Milli-Q water and the SiO2-90nm particle suspensions at $\Phi_V = 1$ and 8.3% was measured as function of the shear stress. To test if the particle suspension viscosity changed with the particle electrical charge, we measured the viscosity of the suspensions at pH2 and pH9, namely, weakly and strongly interacting charged particles, respectively. The results show (see Figure 6.8) that the viscosity of the particle suspension was not affected by the particle concentration nor the particle electrical charge. Hence, the particles arrangement during the drying of the suspension seems to be not altered by the suspension viscosity. Furthermore, the particle-particle interactions in the bulk did not present significant changes compared with the dilute regime studied in Section 6.3. Thus, we assured that the contact line dynamics in CSSD experiments was not affected by viscous effects.

6.6 Wettability of particles

Dynamics of three-phase contact lines of drying sessile drops will depend on the wettability properties of substrate and nanoparticles. The amplitude of contact angle hysteresis and the receding contact angle of the substrate will determine the transition of an evaporating drop from the situation of static contact line to moving contact line with constant contact angle. If the drop contains nanoparticles, the wettability contrast between substrate and particle will also affect triple line motion through the self-pinning effect (see Section 5.1).

We define the wettabillity contrast ($\Delta\theta$) as the difference between the substrate receding contact angle and the particle receding contact angle ($\Delta\theta = \theta_s - \theta_p$). We selected the receding contact angle because during CSSD experiments and in general, during any suspension drying process, the contact line motion is firstly lead by the receding contact angle of the substrate and secondly, it is affected by the receding contact angle of the particle.

It is well known that measuring the contact angle of mesoscopic particles is a very hard

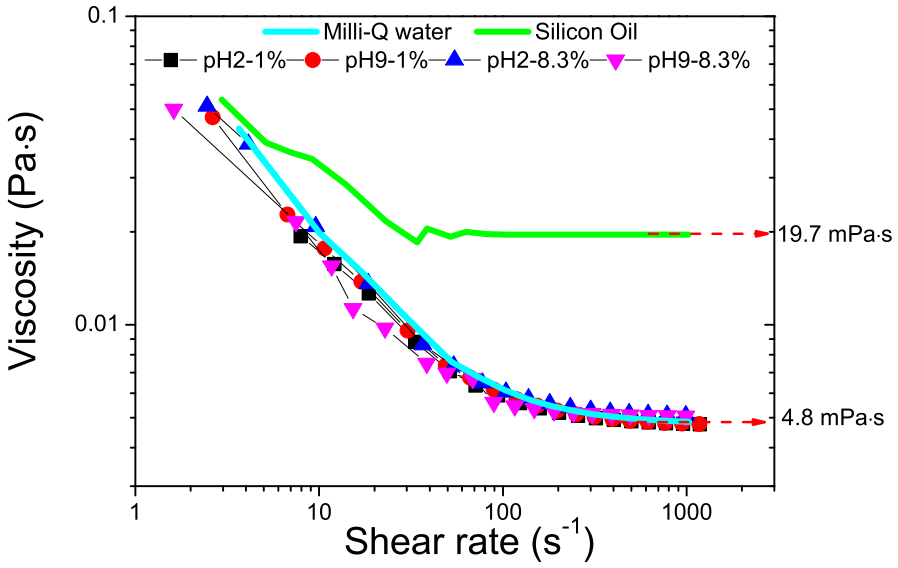

Figure 6.8: Viscosity as function of shear stress of Milli-Q water, silicone oil (calibration liquid) and SiO2-90nm suspensions at $\Phi_V = 1$ and 8.3% and pH2 and pH9.

task (144). We assumed that the advancing and receding contact angles of PMMA, PS and TiO2 substrates, measured in Sections 3.1.1 and 6.8, agreed with the contact angles of the corresponding nanoparticles. For the rest of suspensions, we took the values reported in (145). Since TiO2 contact angle depends on the pH value (see Section 6.8), we list the contact angle values for the three pH values studied in the present work.

Particle	θ_a (°)	θ_r (°)	$\theta_a - \theta_r$ (°)
SiO_2*	25	12	13
TiO_2 pH9	66.5	24.2	42.3
SiO_2-NH_2*	78	30	48
TiO_2 pH5.5	76.2	37.5	38.7
TiO_2 pH2	79	43.5	35.5
PMMA	72	52	20
PS	92	72	20

*Contact angle values taken from the reference (145).

Table 6.3: Advancing and receding contact angles of the particle suspensions used in this work. Since the TiO2 contact angle is a function of pH value, we list the three different values of pH studied in this work.

CSSD experiments were performed on PMMA and TiO2 surfaces as described in Section 2.5. This way, experiments with positive and negative wettability contrast were studied according to the type of particle. Moreover, experiments with zero wettability contrast were reproduced for the cases of TiO2 surface-TiO2 particle and PMMA surface-PMMA particle. The condition of

zero wettability contrast might be arguable due to the different origin of particle and substrate. For example, in the TiO2-TiO2 system the particles were composed of titania (titanium oxide) whereas the substrate was pure metallic titanium, immediately oxidized. Similarly, the PMMA particles were prepared by synthesis and the PMMA sheets by extrusion.

6.7 Surface tension

Adsorption of nanoparticles at the liquid-air interface of drying drops may change the evaporation rate. The surface tension measurement enables to detect if the nanoparticles prefer to diffuse towards the water-air interface rather than to remain in the drop bulk. It is worth mentioning that the surface tension of a sessile drop of pure liquid does not affect the motion of contact line, which depends on the wettability properties of the substrate. However, if there were nanoparticles at the liquid-air interface very close to the triple line then the solid-liquid interactions would change and so, the contact angle. Moreover, the arrangement of nanoparticles at the vicinity of contact lines might be altered due to the interactions with the nanoparticles placed at the liquid-air interface.

We monitored the surface tension of static pendant drops of the nanoparticles suspensions studied in this work in terms of time. The experimental device was the same than used for contact angle measurements (see Section 2.3).

To check if water surface tension changed with the pH value, a 25μl pendant drop of buffer solution was formed at a constant flow rate of 0.4 μl/s, and its surface tension was measured for 400 s. Each experiment was repeated 5 times. Results for surface tension (symbols) and drop volume (lines) of buffered solutions at pH2, pH5.5 and pH9 values are shown in Figure 6.9. The drop formation took long 60 s, as illustrated in Figure 6.9 before the vertical dashed line. Once the final drop volume was reached then the surface tension held a constant value. We observed that the water surface tension did not change with the pH value.

To study adsorption of nanoparticles at the liquid-air interface, we prepared particle suspensions buffered at pH2 and pH9 values with a concentration of $\Phi_V = 1\%$. At these values, the particle-particle electrostatic interactions were mostly weak and strong, respectively. The density of particle suspensions was not measured, instead we calculated it as:

$$\rho_s = \rho_p \Phi_V + \rho_w \left(1 - \Phi_V\right)$$

where ρ_s, ρ_p and ρ_w are the densities of the suspension, the particle and the pure water respectively. We chose PMMA, PS and SiO2-120nm particles due to their different hydrophilicity (see Table 6.3). We monitored the surface tension of 25μl pendant drops of the particle suspensions above mentioned. The results are presented in Figure 6.10. The initial value of surface

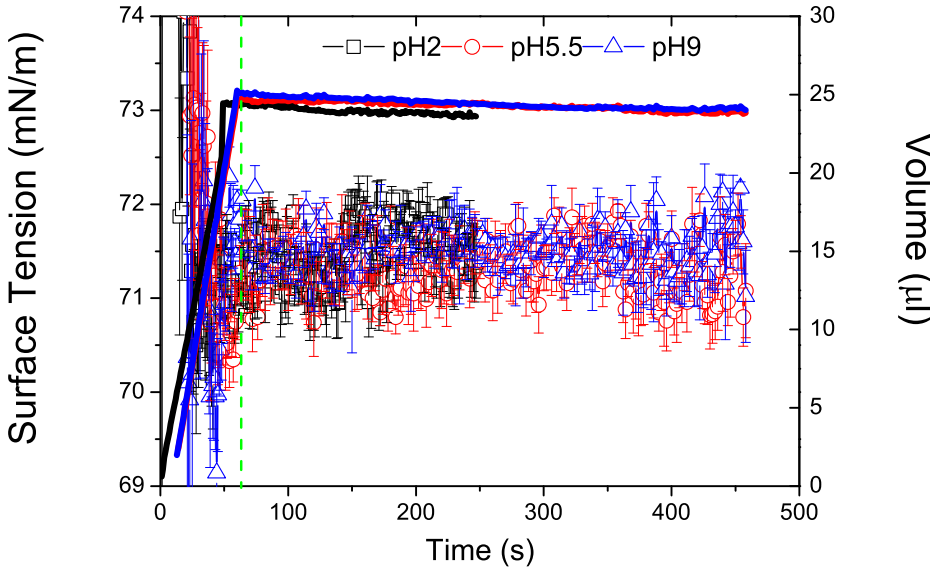

Figure 6.9: Surface tension (symbols) and drop volume (lines) as function of time for water pendant drops at different pH values.

tension of the three particle suspensions was lower than the value of buffered water (see Figure 6.9). This decrease seems to be due to the fast particle migration towards the interface during the drop formation. Moreover, the initial value of surface tension for each suspension (dashed lines in Figure 6.10) seems to be correlated to the particle size (see Figure 6.2): smaller particle, faster diffusion. However, this effect might be also modulated or even exceeded by the particle hydrophilicity: more hydrophilic particle, greater interfacial activity. Unlike SiO2-120nm particles, a surface tension reduction of about 3% after 450 s was found for PMMA and PS particles. This reduction might be explained by the liquid evaporation. However, in all the cases described, the role of pH was negligible.

During the drop evaporation, the particle concentration in the drop bulk increased and new particles diffused towards interface reducing further the surface tension. Alternatively, due to the decrease of liquid-air area, the particle density at the interface could increase. However, this effect was less marked as higher hydrophilicity of particle (PS<PMMA<SiO2) due to the plausible saturation of the water-air interface. This effect was also enhanced as the particles were smaller (PS<PMMA<SiO2).

In summary, the surface tension of the SiO2 nanoparticle suspensions revealed a weak dependence on the particle hydrophilicity. For CSSD experiments, with sessile drops of 200 μl without significant evaporation, we assumed that the liquid-air adsorption was negligible.

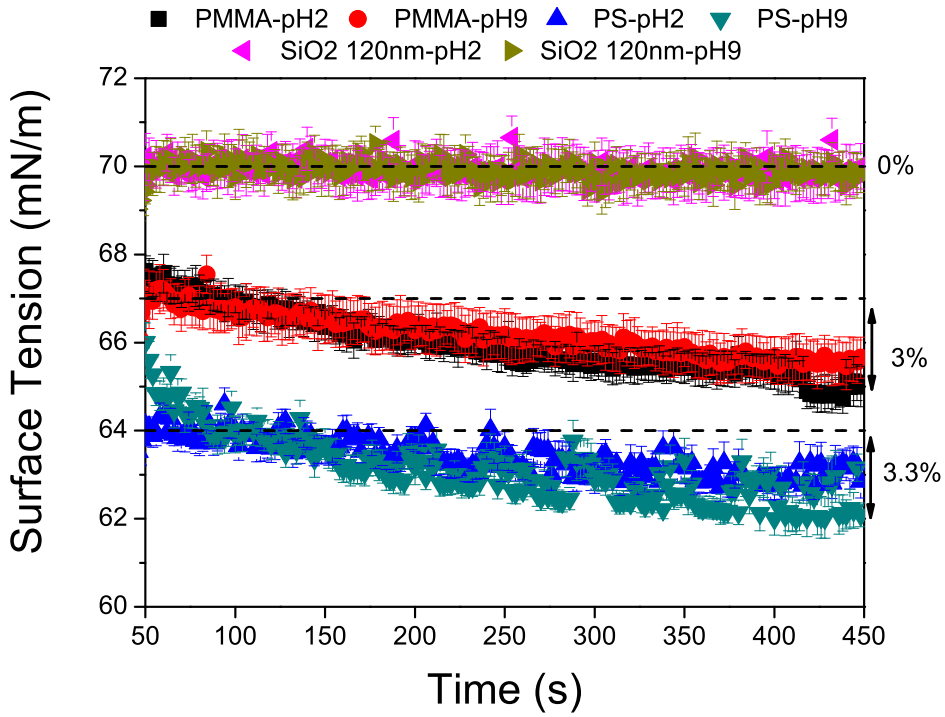

Figure 6.10: Surface tension in terms of time of suspensions of SiO2-120nm, PMMA and PS particles at pH2 and pH9, $\Phi_V = 1\%$. The dash lines show the initial value of surface tension for PMMA and PS particles.

6.8 Substrates for deposit formation

Pinning of contact line is fundamental for the ring/stain formation during evaporation of a colloidal drop (see Section 5.1). If the contact line is pinned at the edge of the drop, it is preventing from retracting and when the drop volume is reduced by loss of liquid, a strong outward flow in the solvent is created. This flow carries most of the solute to the contact line. Under these conditions, when the evaporation process is finished, a ring/stain deposit is created (6).

Wettability is a very important property of solid surfaces, which is governed by both chemical composition and surface topography. The contact angle hysteresis of the substrate can provide the force necessary to pin the contact line (see Section 1.1.4). Therefore, the substrate hysteresis plays a very relevant role in the particle deposit formation.

In the next Chapters, we employed PMMA (2mm-thick sheets, CQ grade, Goodfellow) and commercially pure (unalloyed) titanium (ASTM grade II-Manfredi) as substrates for deposit formation. We chose these materials by their different wettability response. In order to characterize the substrate hysteresis, we measured the advancing and receding contact angles using the QFR technique (see Section 3.1.1).

6.8.1 Poly(methyl methacrylate)

The PMMA sheets employed for deposit formation were cut by laser as discs with 1.5 cm in diameter. A hole of 1 mm diameter was done on each sample. Before each experiment, the surfaces were cleaned ultrasonically in a detergent solution for 10 min, followed by ultrasonic rinsing in Milli-Q water. Finally, the samples were immersed in Milli-Q water.

The roughness was measured with a white light confocal microscope (PLμ, Sensofar Tech S.L.) using the different objectives: 10X (1.39 x 1.02 mm^2), 20X (695.5 x 509.18 μm^2), 50X (285 x 209.2 μm^2), 100X (138.7 x 101.85μm^2) and 150X (95 x 69.75μm^2). As well, the roughness was measured with an atomic force microscope (MultiMode Scanning Probe Microscope, Nanoscope IV, Veeco). The results are shown in Figure 6.11. As expected, depending on the observation scale, quite different values of roughness may be obtained. Roughness parameters increase as the measurement scale because at lower scale, they reveal short range correlated features and at greater scales, they monitor entirely the long period roughness oscillations. However, for the scale of the distance covered by the moving contact lines in CSSD experiments (see next Chapter), the PMMA substrates were reasonably smooth.

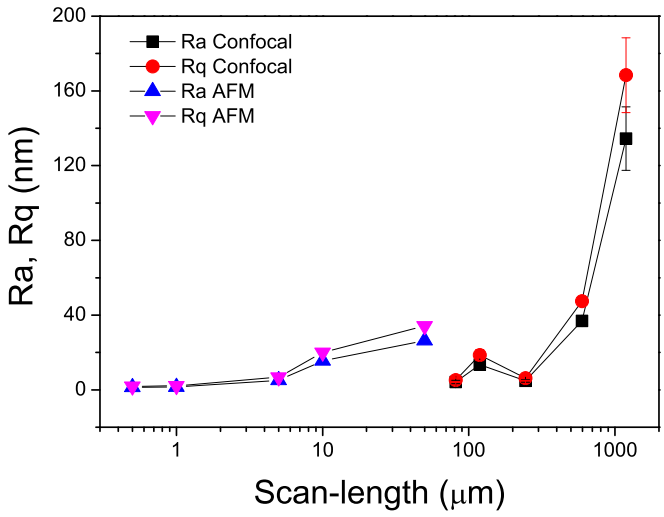

Figure 6.11: Roughness values of the PMMA substrates measured with a white light confocal microscope and an atomic force microscope.

Next, we studied the contact angle hysteresis of PMMA substrates with Milli-Q water. We measured low rate dynamic contact angles using the QFR method (Section 2.4). The drop volume was 120μm. The results are shown in Figure 6.12. They were averaged over five drops. We observed no stick-slip effects. The CAH observed was $\approx 20^\circ$. To investigate if the wetting response of PMMA was altered by pH, we performed QFR experiments with buffered drops at pH

ranging from 2 to 9. From the results plotted in Figure 6.13, we concluded that the advancing and receding contact angles of buffered drops on PMMA surfaces were independent of pH.

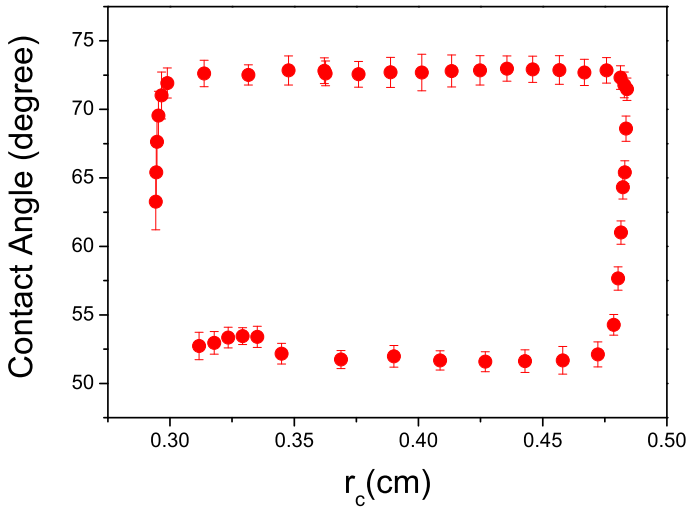

Figure 6.12: Advancing and receding contact angles of Milli-Q water drops on the PMMA surfaces using the QFR method. The maximum drop volume was 120μl.

6.8.2 Titanium

Commercially-pure titanium consists of polycrystalline grains with diameters of several microns. A native oxide layer, with a thickness of several nanometers, usually covers the titanium grains. This oxide layer is amorphous and irregular in thickness and chemical composition. The "intrinsic" contact angle of the oxide surface on titanium is still controversial, and depends on the surface roughness, oxide crystallinity and adventitious contaminants. Hence, the wetting response of titanium surface depends on their previous history. The water contact angles of flat titania and titanium metal surfaces are typically below 10° when measured immediately (<5 min) after UV/ozone cleaning (146). On the other hand, for an atomic layer deposited 56 nm thick TiO2 film (amorphous), the water contact angle was 80° prior and 6° after UV irradiation overnight (147).

The TiO2 cylinders were suitably cut into small disks of approximately 15-16 mm in diameter and 1.5 mm in thickness. Next, titanium surfaces were finely polished. The samples were sonicated in distilled water, next in a solution of 70% (v/v) acetone (20 min) and again in distilled water (30 min).

To study the topography of the TiO2 surfaces, we used white light confocal microscope and AFM in the same manner than for the PMMA surfaces (Figure 6.11). The results are shown in

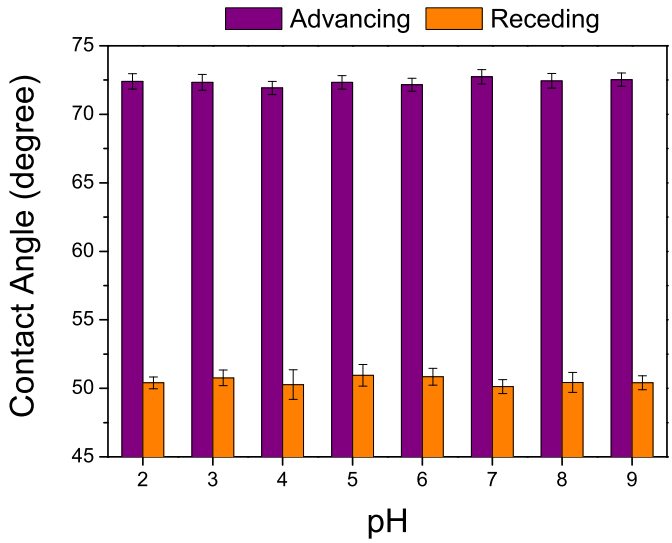

Figure 6.13: Advancing and receding contact angles measured on the PMMA surfaces as function of pH using the QFR method. The maximum drop volume was 120μl.

Figure 6.14.

Next, we characterized the contact angle hysteresis of the smooth titanium surfaces. We measured low-rate dynamic contact angles of Milli-Q water and buffered drops at pH2, pH5.5 and pH9 on the titanium surfaces with the QFR method. The results in Figure 6.15 show that for the case of TiO2 surface, the advancing and receding contact angle depended on the pH of the drop. The dependence of the contact angle could be due to the electrical response of the TiO2 as the medium pH was changed. As shown in Figure 6.4, the electrical charge of TiO2 nanoparticles at pH2 is highly positive, at pH5.5 they present the IEP and at pH9 the charge is highly negative. Thus, the variability in the electrical behaviour of TiO2 with the pH is directly observed in the contact angle response.

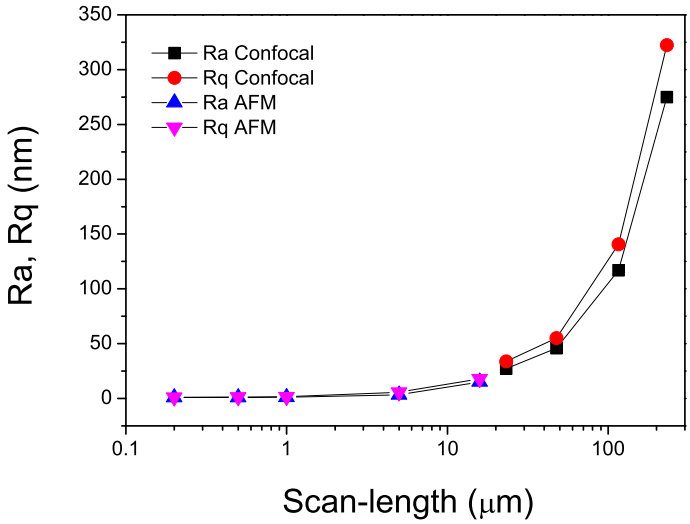

Figure 6.14: Roughness values of the TiO2 surfaces measured with a white light confocal microscope and an atomic force microscope.

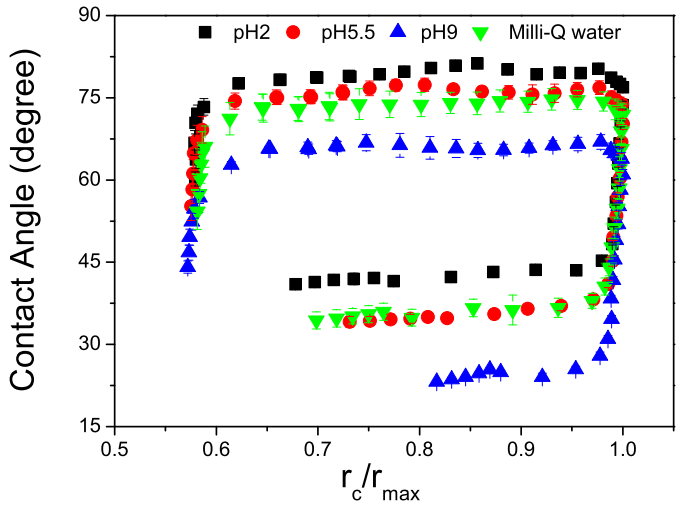

Figure 6.15: Advancing and receding contact angles measured on the TiO2 surfaces with Milli-Q water and buffer solutions at pH2, pH5.5 and pH9 using the QFR method. The maximum drop volume was 120μl.

6.9 Summary

We have characterized the nanoparticle suspensions and the substrates that we used for the experiments described in Chapters 8 and **??**. In Table 6.4 we summarize the main properties of the particle suspensions studied in this work. The main remarks are:

Particle	**diameter(nm)**	$\theta_r\ (^0)$	**IEP**
SiO_2-20nm	22 ± 1	12	pH2
SiO_2-50nm	50 ± 5	12	pH2
SiO_2-90nm	92.1 ± 1.2	12	pH2
SiO_2-120nm	$125 \pm 4.5\ 2$	12	pH2
SiO_2-1.16μm	1160 ± 60	12	pH2
SiO_2-NH_2	100 ± 6	30	pH9
PS	40 ± 2.4	72	*
TiO_2	57.6 ± 18.6	37.5	pH5.5
PMMA	90.2 ± 8.3	52	pH2*

Table 6.4: Particles used in this work and their main features. *As shown in Figure 6.4, the PMMA particles did not reveal isoelectric point, however the minimal electrostatic interactions were obtained at pH2. The electrical charge of PS particles was constant regardless of pH value.

i. The particle suspensions mostly showed a narrow diameter distribution over a wide range of mean sizes (see Figure 6.2).

ii. The electrical charge of the particles was accordingly altered through the medium pH, even becoming zero (see Figure 6.4).

iii. Most particles were negatively charged for the pH range studied (pH2-10). Instead, TiO2 and SiO2-NH2 particles were positively charged in the range from pH2 to pH5 (see Figure 6.4).

iv. Minimal electrostatic interactions were obtained at pH2 for SiO2 and PMMA particles (see Figure 6.4).

v. Minimal electrostatic interactions for TiO2 particles were reproduced at pH5.5 (see Figure 6.4).

vi. The particle suspensions were stable during the experimental time. Aggregation and sedimentation phenomena were not presented (see Figures 6.5, 6.6 and 6.7).

vii. The viscosity of the particle suspensions was not affected by the particle concentration nor the particle electrical charge (see Figure 6.8).

viii. PS particles revealed the lower hydrophilicity and SiO2 particles, the higher hydrophilicity (see Table 6.3).

ix. Liquid-air interface was not significantly affected by the particle suspensions (see Figure 6.10).

x. The advancing and receding contact angles of the PMMA surfaces were independent of the medium pH (see Figure 6.13).

xi. The advancing and receding contact angles of the TiO2 surfaces depended on the medium pH (see Figure 6.15 and Table 6.3).

CHAPTER 7

Evaporating drops and shrinking drops of nanoparticle suspensions

Deegan et al (6) found that there are two necessary conditions for ring like deposits formation: contact line pinning and evaporation from the edge of the drop . When one of these conditions is relaxed, the final deposit is uniform or a central spot is observed (see Section 5.1). For a drop in which the liquid is removed from the center of the drop (shrinking drop), it has been theoretically proved that, instead of a solute ring, a uniform deposit of particles should be formed (148). This type of "evaporation" does not induce a flow of liquid toward the contact line. Since the loss of liquid is from the center of the drop, then an inward flow is developed and the "evaporated" liquid is replenished in the bulk. The CSSD technique (described in Section 2.5) fulfills one of the two necessary conditions for ring-like deposit formation: pinning of contact line. However, the loss of liquid is not performed from the contact line but from the bulk. Under these conditions, the formation of ring-like deposits are not expected to occur.

In order to study the contact line dynamics of freely-evaporating drops of nanoparticle suspensions, we performed evaporation experiments with SiO2-20nm, SiO2-50nm, SiO2-120nm and PMMA suspensions on PMMA surfaces. The suspensions were diluted in Milli-Q water (at free

pH [a]) at $\Phi_V = 1\%$. The drop volume was 100μl. The experiments were perfomed at room temperature (25°C) and relative humidity of 50%. The results are shown in Figure 7.1. In all the cases, the initial behaviour of the contact line was similar: at the beginning of the experiment, the contact line was pinned while the contact angle was decreasing and once the receding contact angle was reached (about 50° see Section 6.6), the contact line started to recede. For the SiO2-20nm suspensions, the contact line was receding with the same contact angle, but at $r_c \approx 0.7 r_{max}$ the contact angle began to decrease again till the end of the experiment. For the SiO2-50nm and SiO2-120nm suspensions, the behaviour of the contact line was similar to the former case although the contact angle decreased during the entire process. For the PMMA suspensions, the contact line was pinned at the beginning of the experiment, the contact angle was decreasing and the contact line began to move once the receding contact angle was reached. During this receding motion of the contact line a jump was observed ($r_c \approx 0.97 r_{max}$). Next, the contact line continued to recede and the contact angle was decreasing . At $r_c \approx 0.9 r_{max}$ the contact angle abruptly decreased. At $r_c \approx 0.85 r_{max}$, a second jump was observed and finally at $r_c \approx 0.75 r_{max}$, the contact line remained pinned till the evaporation process was finished. The differences observed with the PMMA suspensions compared with the SiO2 suspensions could be due to the substrate-particle wettability contrast (see Section 6.6). As we will illustrate later, the wettability contrast becomes very relevant for the pinning behaviour of contact lines.

In order to analyze the different deposits obtained after evaporation, we acquired images of the deposits using an optical microscope (Optiphot-2, Nikon) with an objective 10X. The external and internal parts of the deposits were distinguished. In Figure 7.2 we illustrate the shape of the final deposits formed as well as the positions where the images were acquired. In Figure 7.3 we show the deposits obtained for the different substrate-particle systems studied. For the SiO2-20nm suspensions, a well-defined ring was formed in the external part. In the internal part, a particle layer with cracks was found. The deposit formed with the SiO2-50nm nanoparticles was similar to case of the SiO2-20nm nanoparticles, but the internal layer was joined to the ring in certain positions. The shape of the deposit left with the SiO2-120nm nanoparticle was finger-like (one of these fingers is shown in the Figure 7.3) in the outer part and a layer in the inner part. Alike the SiO2-50nm nanoparticles, with the PMMA nanoparticles, an external ring with finger-like structure was also observed followed by a layer separated by a small distance and in the inner part, some isolated particle deposits were observed, and finally a layer.

In order to study the contact line dynamics of shrinking drops of nanoparticle suspensions, we performed CSSD experiments on PMMA substrates with the SiO2-90nm suspensions diluted in Milli-Q water (free pH) at $\Phi_V = 0.1$, 1 and 3 %. The results of contact line dynamics are shown in Figure 7.4. Unlike the evaporation experiments, the results correspond to mean values of of three experiments performed for each concentration. At the beginning of the experiment,

[a] The pH of a pure water drop gradually changes during the evaporation (dissolved carbon dioxide).

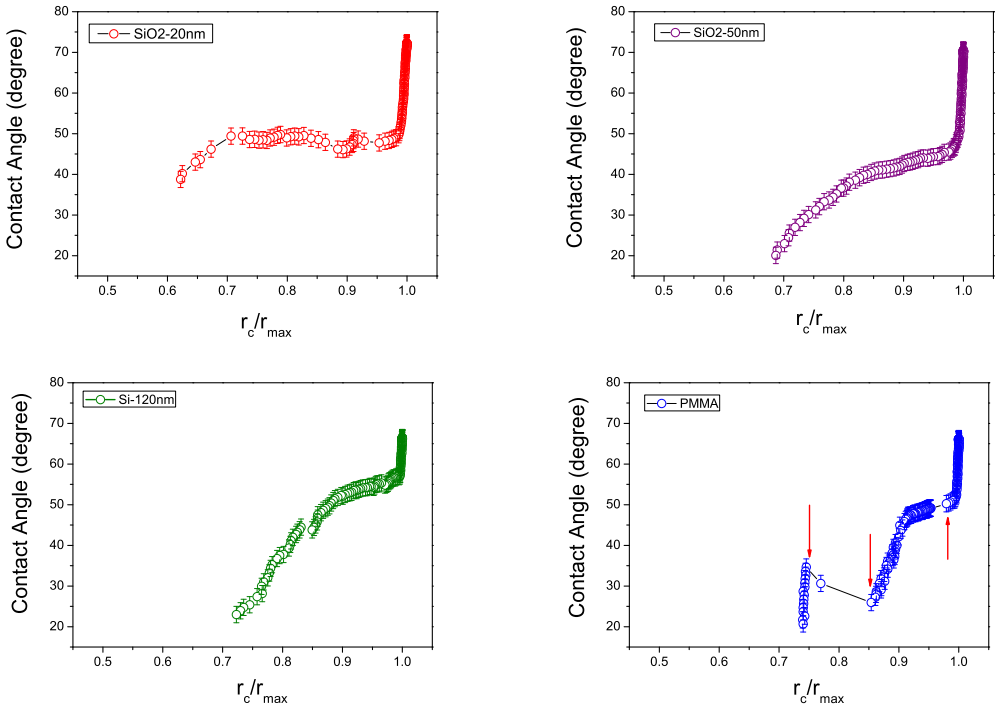

Figure 7.1: Contact line dynamics of freely-evaporating drops of SiO2-20nm, SiO2-50nm, SiO2-120nm and PMMA suspensions on PMMA surfaces. The suspensions were diluted in Milli-Q water at $\Phi_V = 1\%$. The drop volume was 100μl. The red arrows in the graph of the PMMA suspensions indicate the jumps observed during the receding motion of the contact line.

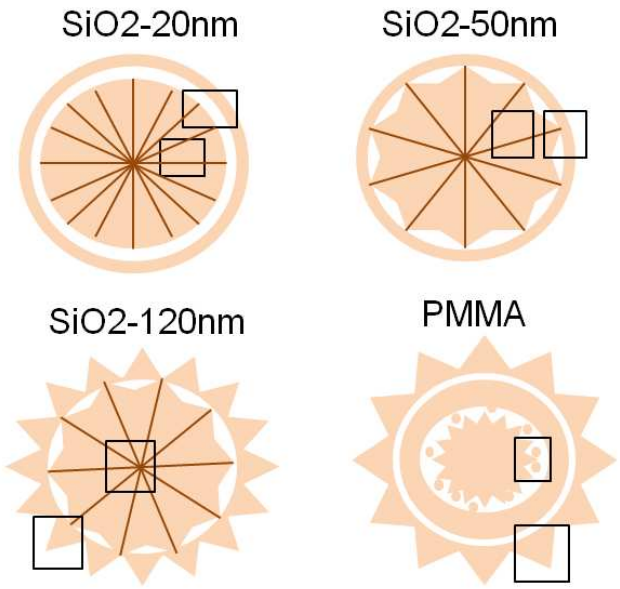

Figure 7.2: Sketch of the shape of the final deposits as well as the positions where the images were acquired. The dark lines represent the main cracks observed.

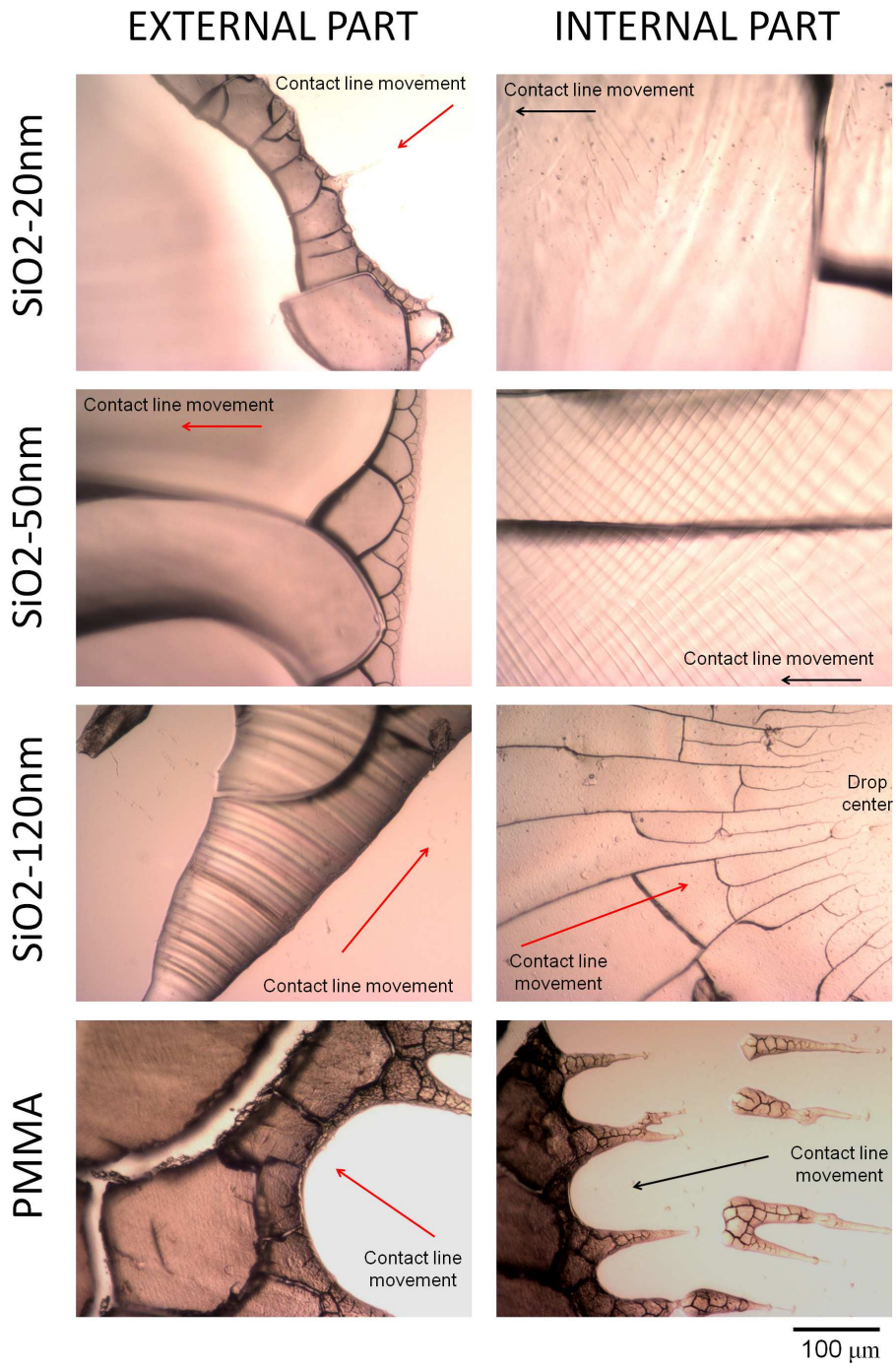

Figure 7.3: Images of the external and internal parts of the final deposits obtained after evaporation experiments. The experiments were performed on PMMA substrates with different suspensions (for each row) at $\Phi_V = 1\%$. The images were acquired with an optical microscope with a 10X objective.

the drop contact radius remained constant (pinning) while the contact angle decreased due to the contact angle hysteresis described in Section 1.1.2. Once the PMMA receding contact angle was reached, the contact line began to move backward and the receding motion was observed till the end of the experiment. The contact line behavior was identical to the case of pure liquids (see Chapter 4) for the three concentration values and, as expected, no particle deposits were obtained, except for the residual spot left at the center of the sample.

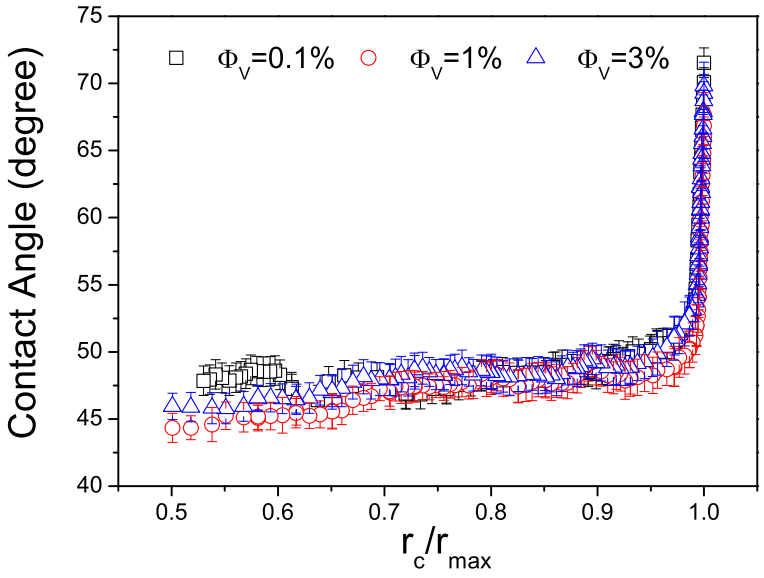

Figure 7.4: CSSD experiments performed on PMMA substrates with the SiO2-90nm suspensions diluted in Milli-Q water at Φ_V =0.1, 1 and 3 %.

To analyze the relevance of the size and the type of particle for the formation of deposits, we performed CSSD experiments on PMMA substrates with SiO2-20nm, SiO2-50nm, SiO2-120nm and PMMA suspensions diluted in Milli-Q water (free pH) at $\Phi_V = 1\%$. The results are shown in Figure 7.5. The error bars represent the standard deviation of the results obtained for three drops. In all the cases, no particle deposits were obtained and the contact line dynamics was very similar to the case of pure water (without particles). As was shown in Figures 7.4 and 7.5, the relevance of the concentration and the size of the particles were not significant for the particle deposition at free pH with the CSSD technique. It is important to remark that during the evaporation of drop containing nanoparticle suspensions, the particle concentration is increasing as the volume is decreasing whereas with the CSSD technique the bulk particle concentration remains constant during the entire process.

From the results shown in Figures 7.4 and 7.5, we conclude that although the CSSD technique standardizes the contact line dynamics of a freely evaporating drop of pure liquid (see Section **??**), it is apparently unable to reproduce the evaporation of a drop with nanoparticles. Due to the

complex physics involved in the drying of nanoparticle suspensions, the particle deposit formation might be dictated by other mechanisms (see Section 5.1) such as the liquid flow, pinning/depinning of the contact line, heat transfer between the drop and the substrate, Marangoni convection, the interaction of the free surface of drop and the growing peripheral deposit, etc. With a freely-evaporating drop of nanoparticle suspensions, particle deposits were always obtained regardless of particle volume fraction and particle size. Instead in the CSSD experiments, no particle deposits were obtained even by varying particle volume fraction and particle size. However, it is plausible to think that other properties of the system can be relevant for the formation of particle deposits and in particular, they could be significant for the formation of deposits using the CSSD technique. During the CSSD experiments, the temperature was assumed to be constant along the drop surface because the (macro)evaporation was negligible. Hence, no thermal Marangoni flow was produced.

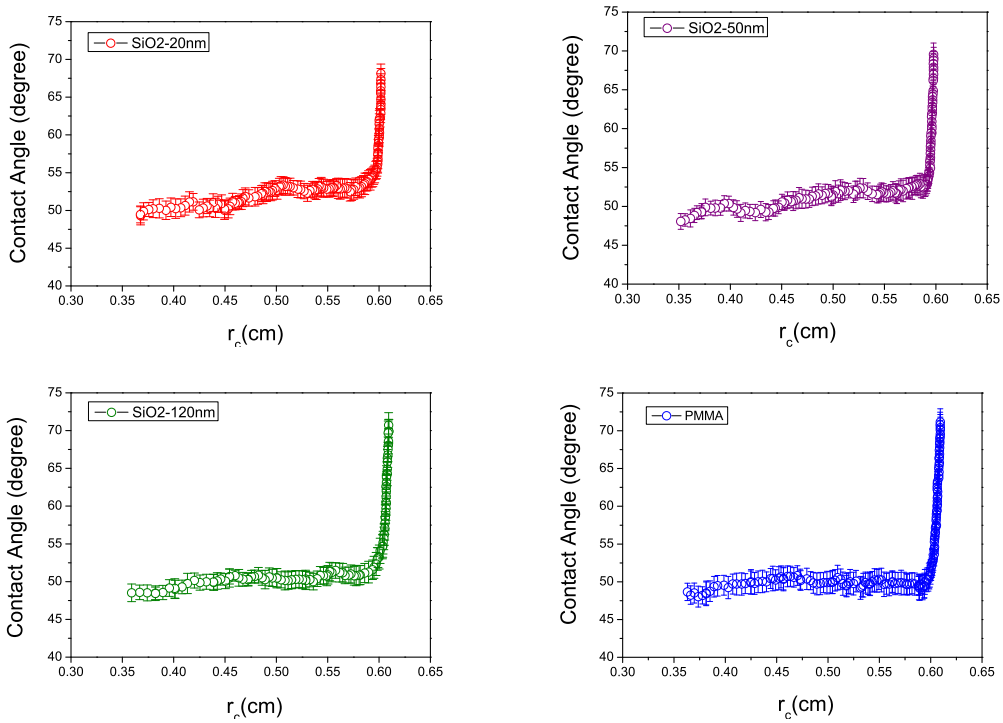

Figure 7.5: CSSD experiments performed on PMMA substrates with SiO2-20nm, SiO2-50nm, SiO2-120nm and PMMA suspensions diluted in Milli-Q water at $\Phi_V = 1\%$.

CHAPTER 8

The role of the electrostatic interactions in the formation of nanoparticle deposits

8.1 Evaporating drops of nanoparticle suspensions

During the drying of particles suspensions, the particle deposition process can be dictated by DLVO interactions, i.e. the electrostatic and van der Waals forces. These interactions might modify the shape of the final deposit (37, 141, 149). In order to test the relevance of substrate-particle electrostatic interactions on the particle deposit formation, we performed free evaporation experiments on PMMA substrates with PS, SiO2-90nm and TiO2 suspensions at $\Phi_V = 1\%$ (see Section 6.1 for details of the suspensions). The drop volume was 100μl. The experiments were perfomed at room temperature (25°C) and relative humidity of 50%. To change the electrostatic interactions, the nanoparticles were buffered at pH2 and 9. At pH2 the substrate-particle electrostatic interactions were minimum, while a strong substrate-particle repulsion was obtained at pH9 (see Figure 6.4). The results showed that different morphologies of the nanoparticle deposits were obtained as the electrostatic interactions of the system were varied (see Figure 8.1).

We also performed free evaporation experiments on TiO2 substrates to examine the attractive substrate-particle interactions. We prepared PS and TiO2 nanoparticle suspensions at $\Phi_V = 1\%$

and pH 2, 5.5 and 9. At these pH values, TiO2 revealed positive electric charge, the IEP and negative electrical charge, respectively (see Figure 6.4). The SiO2-90nm nanoparticles revealed the IEP at pH2 and at pH5.5 and 9, two different magnitudes of negative electrical charge. The electrical charge of PS nanoparticles is not function of pH. At pH2, 5.5 and 9, PS nanoparticles reveal negative electrical charge (see Figure 6.4). Again, we observed very different morphologies as the electrostatic interactions were changed (see Figure 8.2).

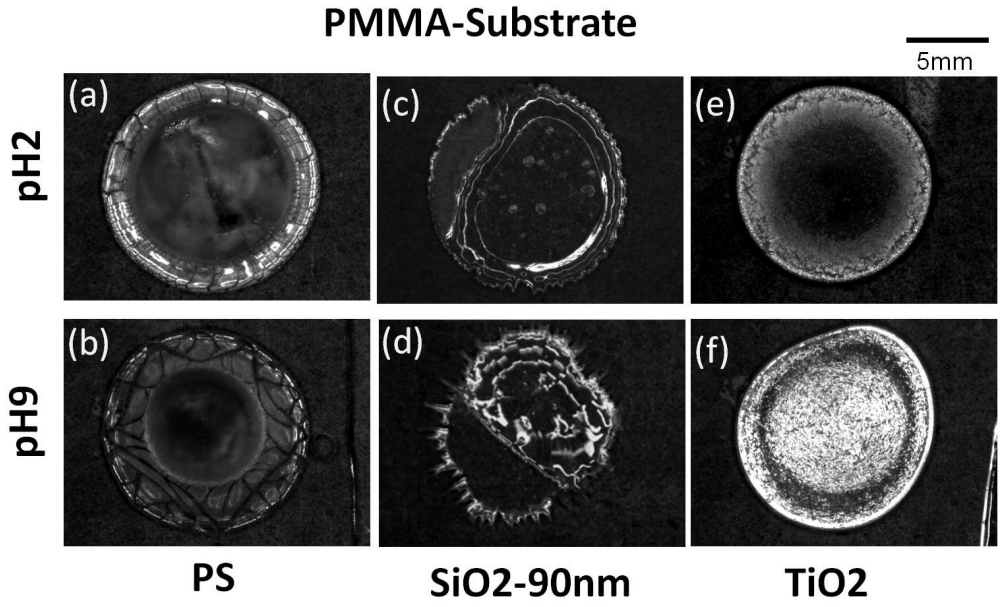

Figure 8.1: View of the nanoparticle deposits obtained after drop evaporation experiments on PMMA substrates with (a)-(b) PS, (c)-(d) SiO2-90nm and (e)-(f) TiO2 nanoparticle suspensions at $\Phi_V = 1\%$. The drop volume was 100μl. The particle-particle and substrate-particle electrostatic interactions were varied through the pH value of the suspensions (see Figure 6.4).

In order to study the contact line dynamics of freely-evaporating drops when the substrate-particle electrostatic interactions were changed, we also performed drop evaporation experiments on PMMA substrates with SiO2-120nm nanoparticles buffered at pH2 and 9. At these pH values, the substrate-particle electrostatic interaction were weak and strong respectively (see Section 6.3). The particle concentration was $\Phi_V = 1\%$ and the drop volume was 100μl. The results are shown in Figure 8.3 [a]. At pH2 the contact line remained pinned while the contact angle was decreasing. This behaviour was kept during the entire evaporation process. However, at pH9 the contact line was only pinned at the first of the process. The contact angle was decreasing till it reached the receding contact angle, then the contact line started to recede. During this motion,

[a] Due to the low reproducibility of evaporation experiments (see Section **??**), we present only the contact line dynamics of one experiment. However we performed three experiments for each system (not shown) to validate the behaviour.

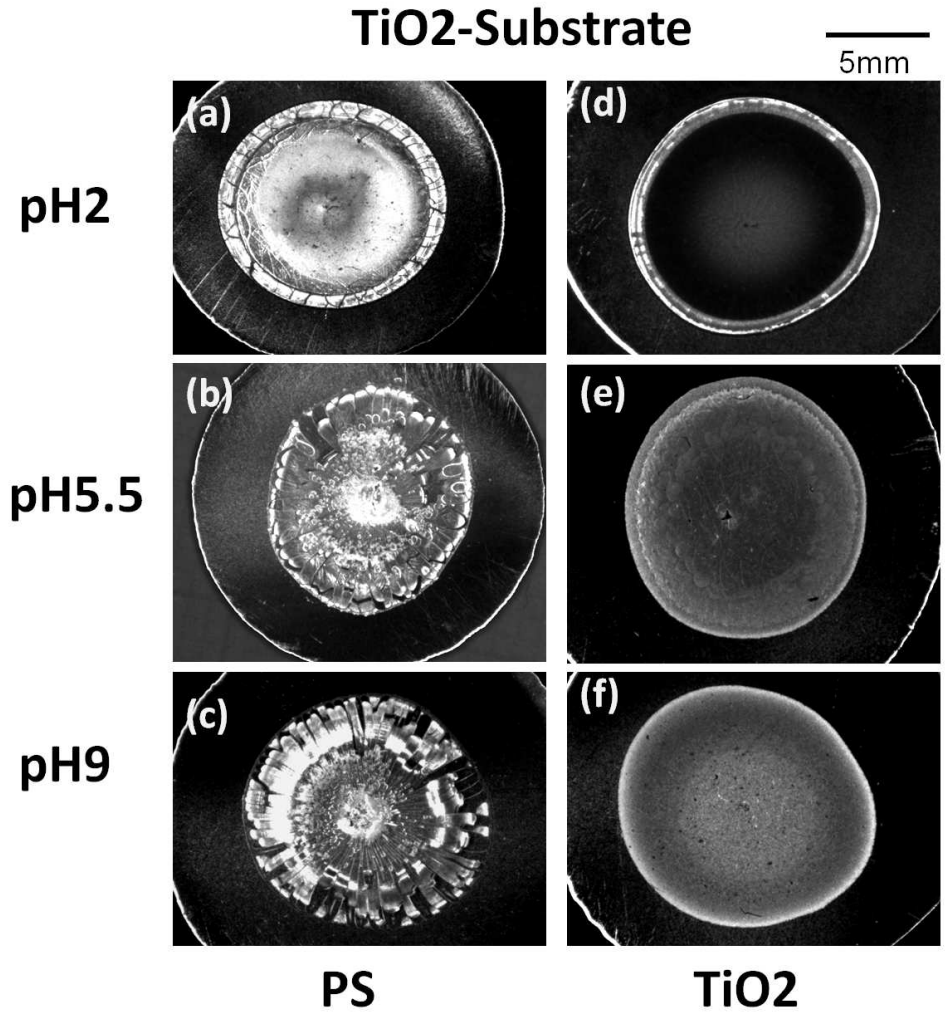

Figure 8.2: Top view of the nanoparticle deposits formed after drop evaporation experiments on TiO2 substrates with (a)-(c) PS and (d)-(f) TiO2 suspensions at $\Phi_V = 1\%$ and different pH values.

the contact angle was decreasing until the evaporation process finished. A jump of the contact line was observed at r_c=0.85r_{max}

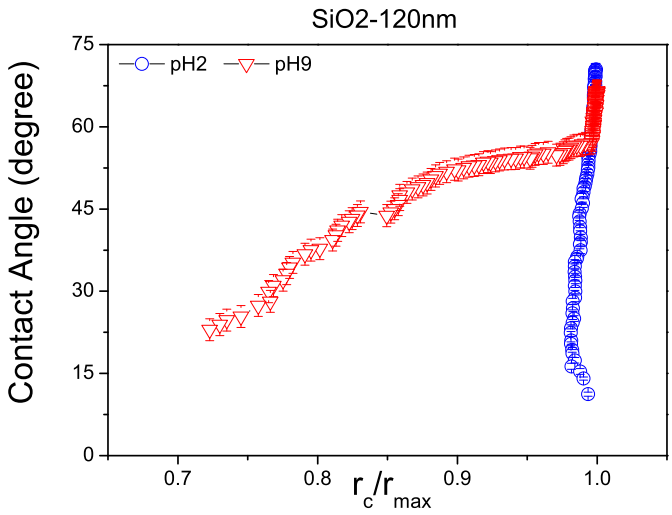

Figure 8.3: The contact line dynamics of free evaporating drops on PMMA substrates with SiO2-120nm nanoparticles buffered at pH2 and 9 and $\Phi_V = 1\%$. The drop volume was 100μl.

From the results obtained for the different substrate-particle electrostatic interactions (see Figures 8.1, 8.2 and 8.3), it is reasonable to think that the nanoparticles deposition might depend on the electrostatic interactions. Bhardwaj et al. (37) have reported that in the case of substrate-particle repulsion, the particles are prevented from contacting the substrate and they follow the general flow pattern, which is radially toward the wetting line forming a peripheral ring. When the substrate-particle electrostatic interaction is weak then the nanoparticles agglomerate and they sparsely spread over the entire initial wetted area. However, there are several unresolved issues still.

In order to study the behaviour of the particles within a free evaporating drop for the cases of electrostatic repulsion and weak electrostatic interactions, we performed drop evaporation experiments with SiO2-1.16μm particles buffered at pH2 and pH9 at $\Phi_V = 0.01\%$ on PMMA substrates [b]. The entire evaporation process was monitored in-situ using an optical microscope (Optiphot-2, Nikon) with a 20X objective. In order to focus the contact line, a 10μl drop was placed on the PMMA substrate. Next, an amount of 5μl was extracted using a micropipette and the drop started to evaporate just before receding. This way, the process started with a initial contact angle lower than the contact angle of the 10μl drop initially placed on the substrate,

[b] We used SiO2-1.16μm particles because microspheres are routinely used to indicate liquid flow in evaporating drops. The SiO2-1.16μm particles system might present undesired phenomena such as sedimentation or aggregation during the experiment (see Chapter 6). However, the SiO2-1.16μm particles at $\Phi_V = 0.01\%$ enabled to explore very different behaviours when the electrostatic interactions were intentionally changed.

varying from the advancing to the receding contact angle (see Section 6.6).

With electrostatic repulsion (pH9, Figure 8.4), we observed that at the very early stages of the evaporation process the microparticles inside the evaporating drop started to accumulate at the contact line (t=5s). The particles followed a radial outward flow and thus they formed a thin ring at moving contact line. The growing of the ring is shown in the images from t=5s to t=3750s. The particles accumulated at the contact line till it was pinned (about t=3500s, image not shown). The contact line pinning could be due to the high particle confinement at the wetting line (37). The strong electrostatic repulsion between particles could explain the ordering of particles at the moving contact line up to a critical volume fraction at the liquid wedge. The final deposit was a ring with almost no particles at the center of the drop. With weak electrostatic interactions (pH2, Figure 8.5), the particles were not observed at the contact line just at the beginning of the process. The contact line started to recede and after t=500s, few particles were observed at the moving contact line. The weakly interacting microparticles accumulated without order driven by the evaporating flow (t=1000s). At t=2000s, a pinning event was observed at the contact line. At t=2500s, the particles accumulated around the pinning point. The contact line remained pinned at this position while it receded. After other pinning events, at t=3615s, the contact line was entirely pinned and a film of liquid was formed. The liquid film collapsed at t=3620s. From t=3620s to the end of the evaporation process, the film dried and a deposit was formed. Again, the final deposit was a ring with almost no particles at the center of the drop. However, the morphology of the deposits was different. Using a white light confocal microscope, we extracted the topography information of the different profiles for each deposit (see Section 8.3 for details). The results obtained are shown in Figure 8.6. The profile of the ring-like deposits formed at pH2 is much higher than the obtained at pH9 (41μm compared with 3.5μm). Nevertheless, at pH9 the ring formed was much wider (179μm compared with 37μm).

On the basis of the results obtained, we have observed some significant differences in the process of drying of nanoparticle suspensions when the electrostatic interactions in the substrate-particle system were changed:

- A wide diversity of deposits can be obtained after drying of drops by varying the pH of the suspensions (see Figures 8.1 and 8.2).
- The contact line dynamics of evaporating drops with nanoparticles was very different as the electrostatic interactions were changed. We observed that weak electrostatic interactions caused that the contact line remained pinned during the entire evaporation process while for a strongly interacting system, a receding contact line was observed (see Figure 8.3).
- The mechanism of accumulation of microparticles at the contact line was different according to the pairwise electrostatic interactions. Driven by the particle-particle repulsion, the particles accumulated at the contact line from the beginning of the process. The particles

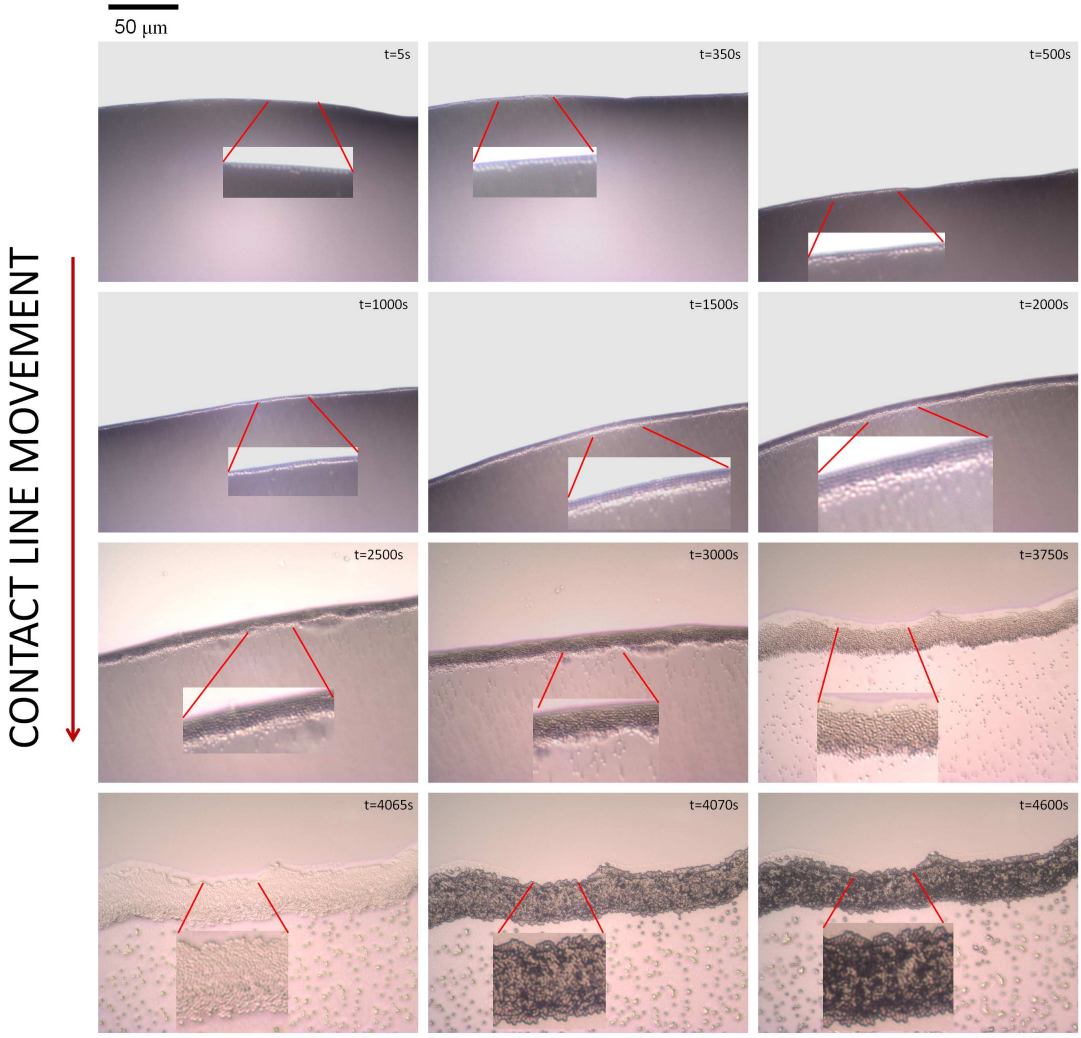

Figure 8.4: Detail of the contact line of a 5μl drop of SiO2-1.16μm suspension buffered at pH9 and at $\Phi_V = 0.01\%$ on a PMMA substrate. The images were acquired with an optical microscope and an objective of 20X.

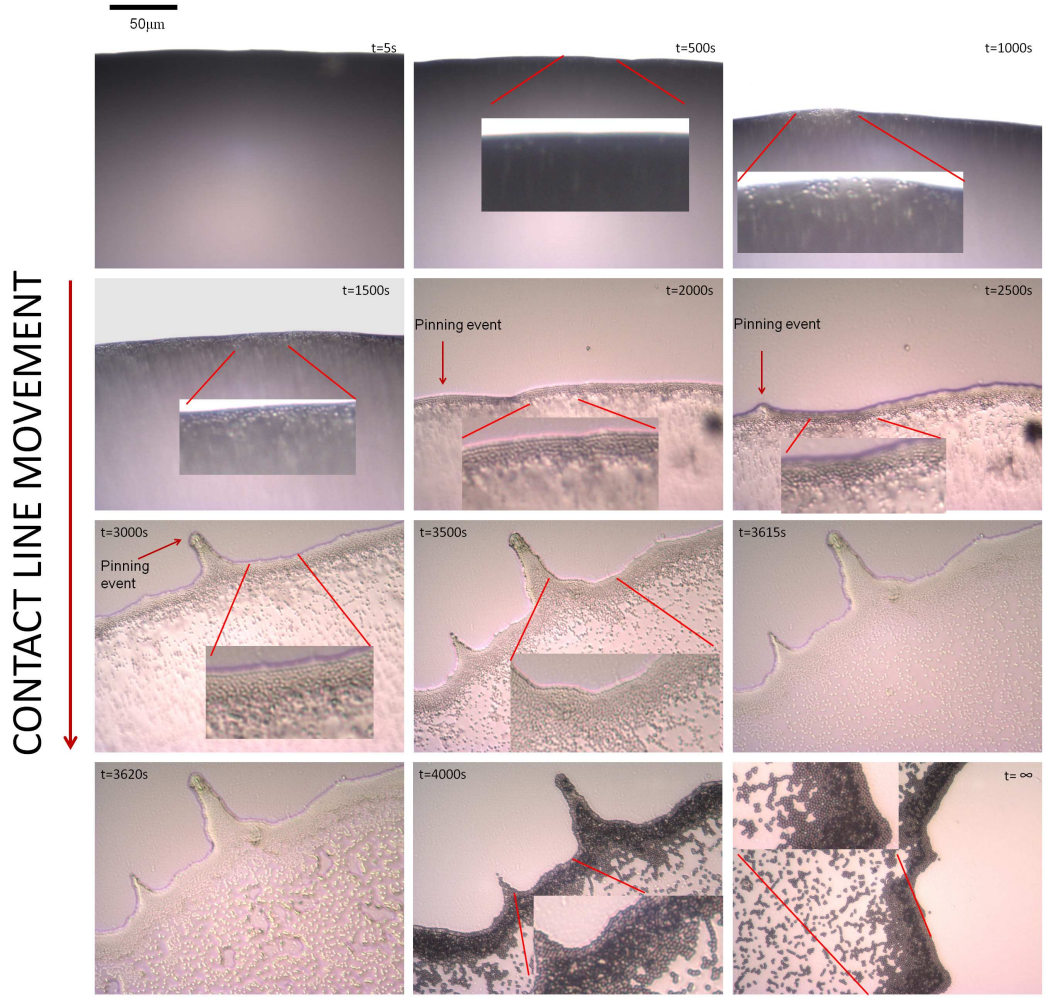

Figure 8.5: Detail of the contact line of a 5μl drop of SiO2-1.16μm suspension buffered at pH2 and at $\Phi_V = 0.01\%$ on a PMMA substrate. The images were acquiered with an optical microscope and an objective of 20X. The image acquired at t=∞ corresponds to a different position of the contact line and the evaporation was concluded.

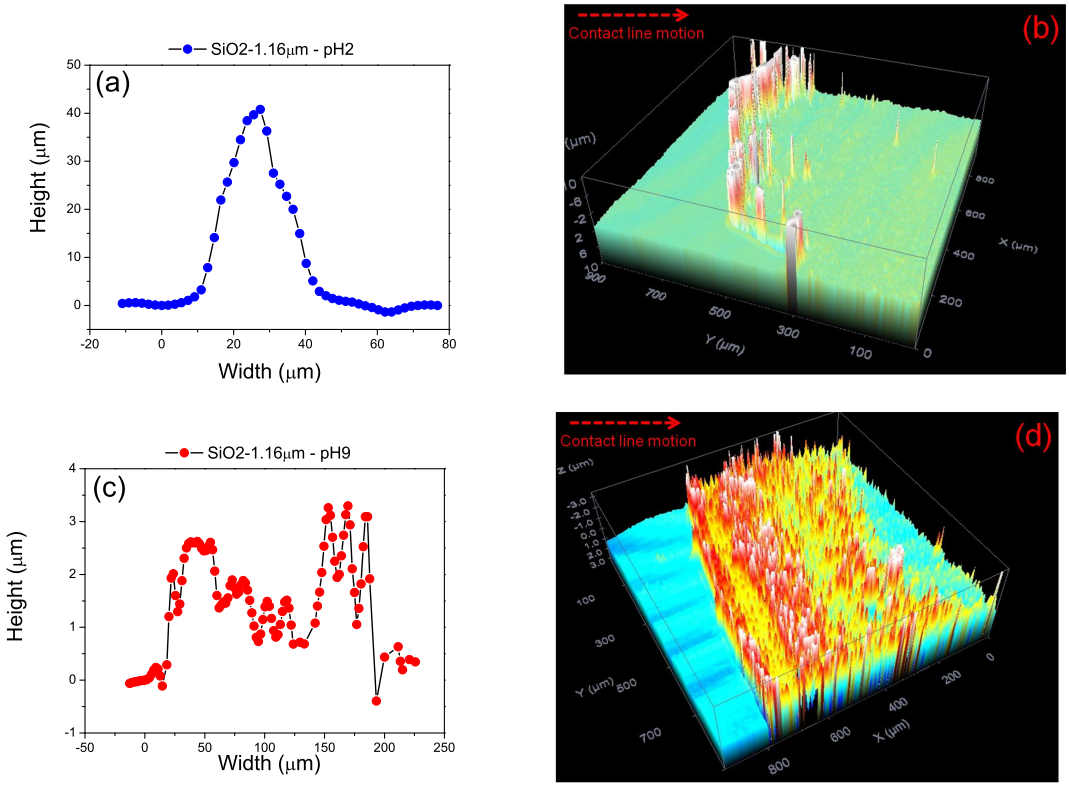

Figure 8.6: Analysis of the profile of the ring-like deposits formed after drop evaporation with SiO2-1.16μm buffered at (a)-(b)pH2 and (c)-(d)pH9 on PMMA substrates, $\Phi_V = 0.01\%$. The images were acquired with a white light confocal microscope.

moved together with the contact line until a global pinning event occurred and finally, the drop evaporated. With weak substrate-particle interactions, the particle deposits formed seem to be caused by the local accumulation of particles during the receding movement of contact line (self-pinning). In this case, the contact line pinning occurred earlier than for the repulsive case (see Figures 8.4 and 8.5).

We have observed that the electrostatic interactions play an important role in the formation of particle deposits. This way, it is reasonable to think that the mechanism of particles deposition when the electrostatic interactions are changed might be examined with CSSD experiments.

8.2 Preliminary CSSD experiments with nanoparticle suspensions

To study the effects of the substrate-particles electrostatic interactions with the CSSD experiments, we performed preliminary experiments on PMMA substrates with the SiO2-90nm suspension at $\Phi_V = 1\%$. The particle suspensions were prepared at pH2, pH5 and pH9. At these pH values, SiO2-90nm nanoparticles revealed the IEP and two different values of negative electrical charge, respectively (see Figure 6.4). The contact line dynamics is shown in Figure 8.7. Initially the behaviour of the contact line for the three pH values was the same one than for pure liquids (see Section 2.5): Constant contact radius, decreasing contact angle (pinning) and once the receding contact angle of PMMA was reached, then the contact line started to move backward. At pH5 and pH9, the contact line receded till the end of the process. However, at pH2 the receding contact line presented a stick-slip behaviour (see Section **??**). After the first contact line pinning, the contact line receded till the contact angle decreased to a certain value (below the PMMA receding contact angle) due to a new pinning event. This behaviour was repeated till the end of the process. The stick-slip behaviour is attributed to the effect of the accumulation of nanoparticles near the triple line (see Section 5.1). Unlike the cases of pH5 and pH9, an external ring-like deposit was formed after the first pinning event (see Figure 8.8). The subsequent stick-slip events caused small nanoparticle deposits (see Figure 8.9). These nascent nanoparticle deposits would become ring-like deposits if the experiment time scale (without evaporation) and the particle concentration in bulk were greater.

In order to monitor the nanoparticles deposition when the substrate-particle electrostatic interactions were varied, we performed CSSD experiments with the SiO2-120nm suspension buffered at pH2 and pH9 at $\Phi_V = 1\%$ on PMMA substrates. The contact line during the CSSD experiments was observed using the optical microscope with a 10X objective. The procedure was similar to the used for the experiments of evaporating drops (see Section **??**). With weak substrate-particle interactions (pH2), Figure 8.10 shows that during the first pinning event the ring formation was completed. Next, the contact line receded and it was pinned again. The subsequent stick-slip

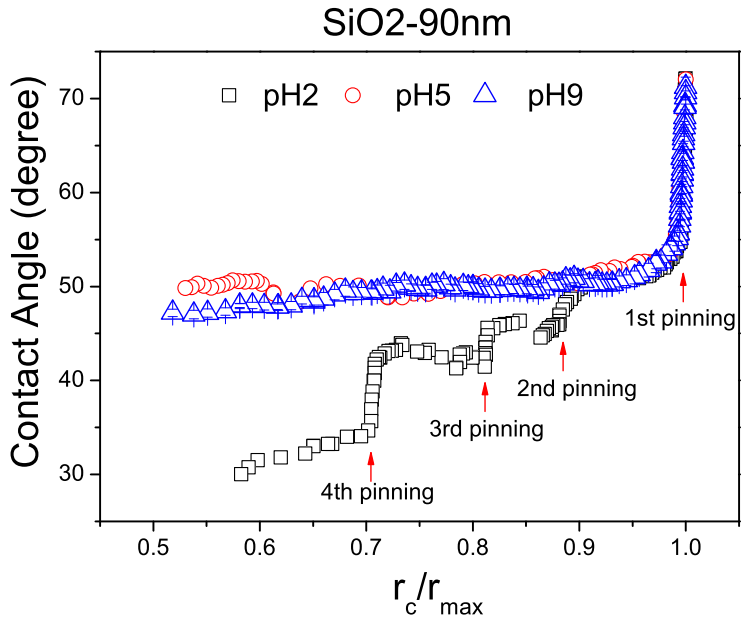

Figure 8.7: CSSD experiments performed on PMMA substrates with SiO2-90nm nanoparticles at $\Phi_V = 1\%$ and buffered at pH2, pH5 and pH9. We found a stick-slip motion of the contact line only for the case pH2. The contact radius was normalized by the maximum contact radius obtained in each case, $r_{max} \approx 0.6$cm.

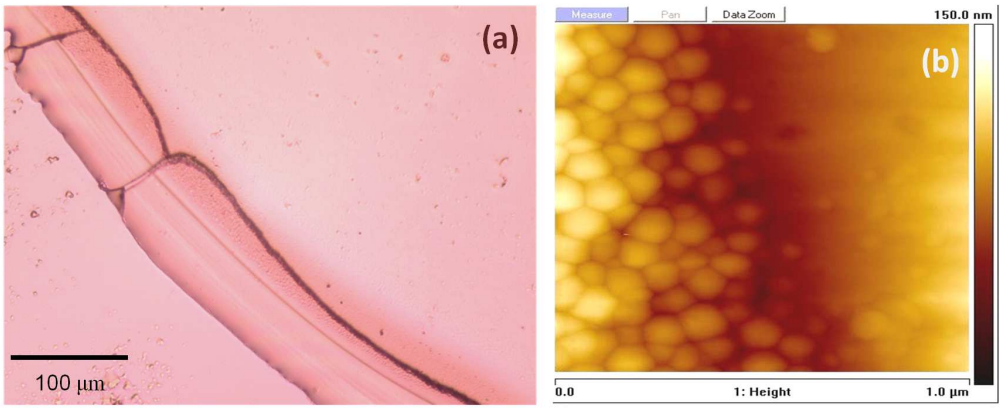

Figure 8.8: Final particle deposit formed with a CSSD experiment on a PMMA substrate with SiO2-90nm nanoparticles buffered at pH2, $\Phi_V = 1\%$. a) Image visualized with an optical microscope (Optiphot-2, Nikon objective 10X). b) Image obtained with an atomic force microscope (MultiMode Scanning Probe Microscope Nanoscope IV, Veeco).

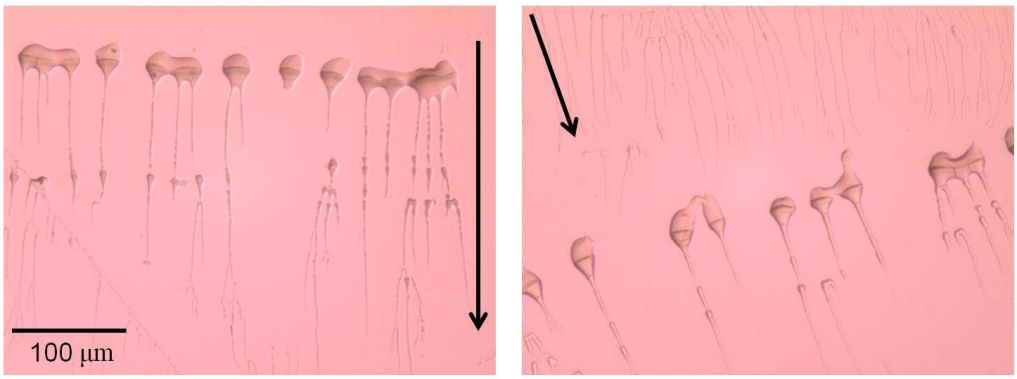

Figure 8.9: Primitive deposits formed after the first pinning event (see Figure 8.7) in a CSSD experiment on PMMA substrate with SiO2-90nm nanoparticles buffered at pH2, $\Phi_V = 1\%$. The images were obtained with an optical microscope (Optiphot-2, Nikon). The branches (weakly bounded nanoparticles) point out to the center of the drop. The arrows indicate the direction of the contact line movement.

events were caused by the nascent deposits (see Figure 8.9). In the case of substrate-particles repulsion (pH9), Figure 8.11 shows that when the contact angle reached the receding contact angle, the contact line started to recede and the receding mode was kept till the end of the process. Except for the residual central spot, no particle deposits were left during the entire process.

We have showed that, certain values above or below, the particle concentration and particle size seem to be unimportant for the formation of particle deposits with the CSSD technique (see Figures 7.4 and 7.5). Then it is plausible to think that particle deposits are formed when the substrate-particle electrostatic interactions are weak (pH2). On the contrary, at pH5 and pH9, when repulsive substrate-particle interactions are involved and the electrical charge of the particles is significant, no particle deposits are obtained. Since the role of the electrostatic interactions is determinant for the apparition of particle deposits, we will examine it with CSSD experiments. It is worth mentioning that, the wettability contrast and contact angle hysteresis (see Section 8.6) can also modulate the morphology of the final deposit.

To study the different cases of substrate-particle and particle-particle electrostatic interactions, we performed CSSD experiments on PMMA and TiO2 substrates at fixed concentration with different suspensions (see Table 6.4). The electrostatic interaction were altered diluting the nanoparticles in buffer solutions at different pH values. The pairwise electrostatic interactions were estimated from the electrophoretic mobility of each material (see Figure 6.4). Following this strategy, we studied the following cases:

i. Substrate-particle electrostatic attraction (SPEA).

ii. Strong substrate-particle repulsion (SSPR).

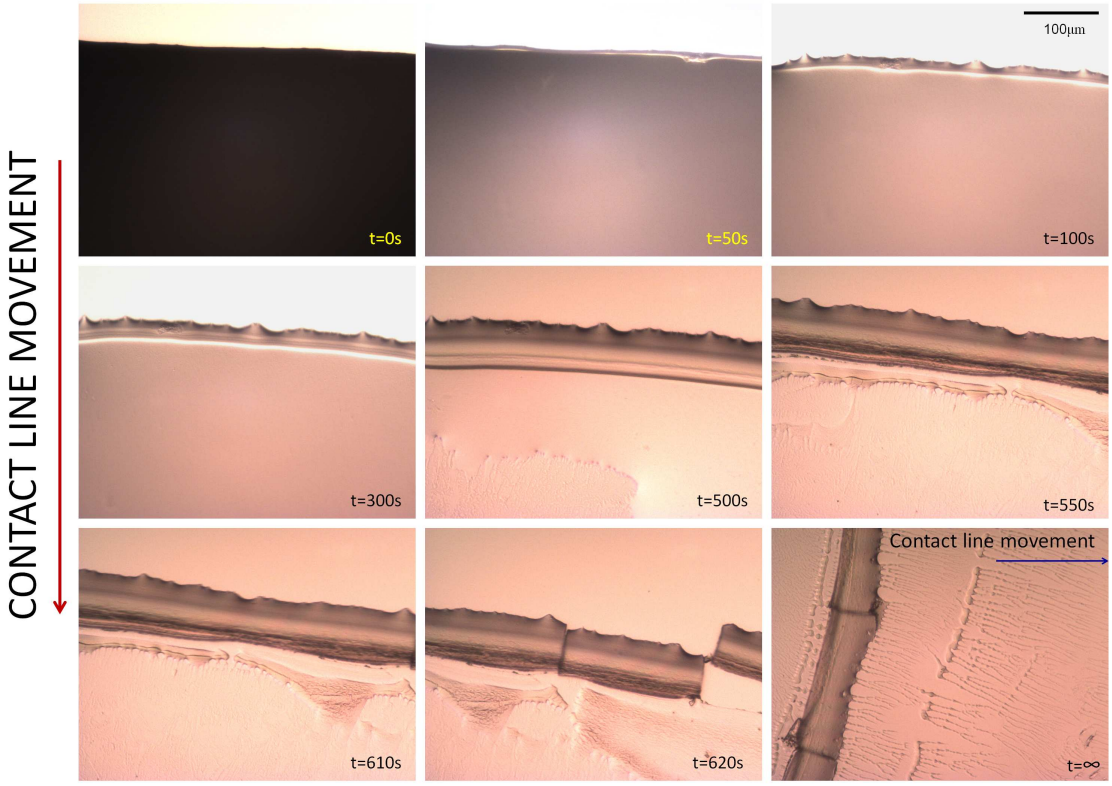

Figure 8.10: Visualization of the contact line during a CSSD experiment of a SiO2-120nm suspension drop buffered at pH2 on a PMMA substrate. The concentration was $\Phi_V = 1\%$. The images were acquired using an optical microscope (Optiphot-2, Nikon) with a 10X objective. The image acquired at t=∞ corresponds to a different position of the contact line and when the CSSD experiment was concluded.

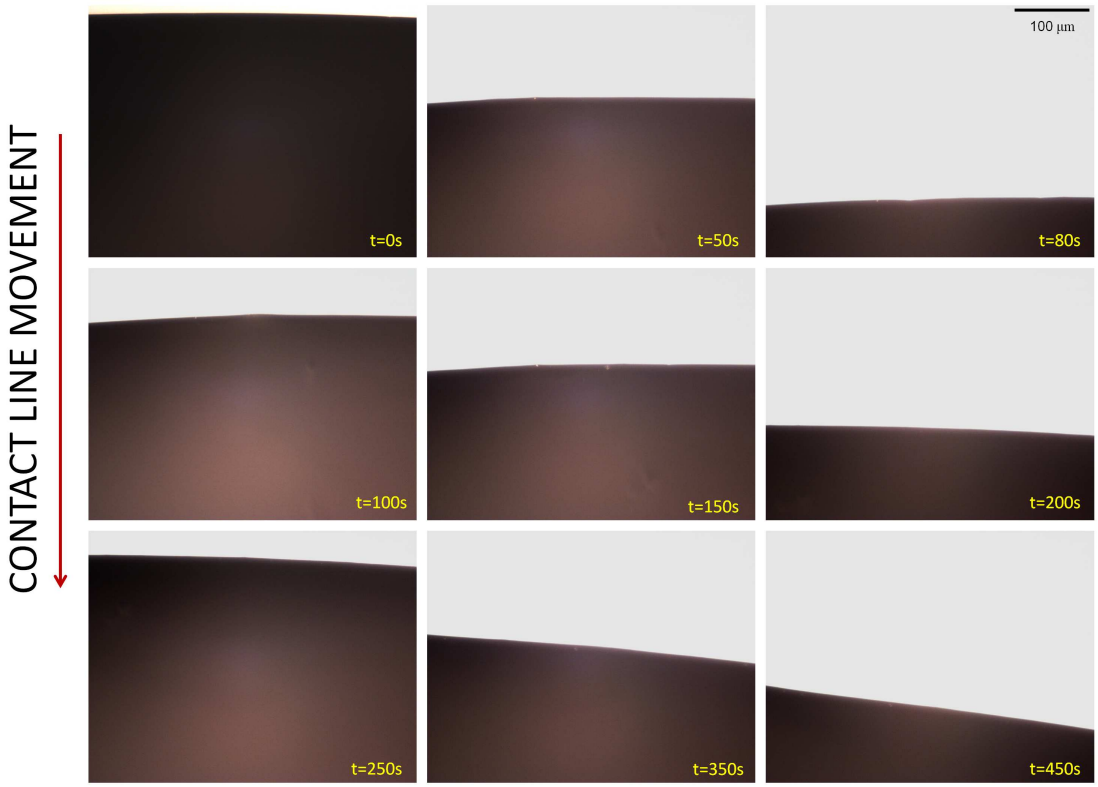

Figure 8.11: Visualization of the contact line during a CSSD experiment of a SiO2-120nm suspension drop buffered at pH9 on a PMMA substrate. The concentration was $\Phi_V = 1\%$. The images were acquired using an optical microscope (Optiphot-2, Nikon).

iii. Weak substrate-particle interaction (WSPI).

8.3 Substrate-particle electrostatic attraction

When the interaction forces are attractive in the drying of colloidal suspensions, the particles close to the substrate are attracted to it and then, they form a particulate layer (37, 141, 149). However, Bhardwaj et al. (37) found that a significant quantity of particles are not directly attracted by the substrate and they form a relatively thick uniform deposit with an unexpected peripheral ring.

The attractive substrate-particle electrostatic interactions were reproduced on TiO2 and PMMA substrates. In addition to the different electrical state, these substrates allowed us to explore two receding contact angles. The nanoparticles used were PS, PMMA, SiO2-120nm and TiO2 suspensions. The different types of nanoparticles allowed us to study the effects of the wettability contrast (see Section 6.6) on the particle deposition process. The nanoparticles were diluted at pH2, pH3 and pH4, and at $\Phi_V = 1\%$. At these pH values, the particle-particle interactions were repulsive with different strengths. The systems examined are shown in Table 8.1.

The results of the CSSD experiments are shown in Figure 8.12. The results show that the contact line dynamics presented stick-slip behaviour with the PMMA, SiO2-120nm and TiO2 suspensions, while for the PS suspension, no macroscopic receding of contact line was observed. We found particle deposits for all the cases studied. However, the morphology of the deposits formed was accordingly different.

Substrate-Particle	ζ_s (mV)*	ζ_p (mV)*	$\Delta\theta(^\circ)$
TiO2-PS	57.9	-47.8	-28.5
TiO2-PMMA	44.8	-34.51	-8.5
TiO2-SiO2-120nm	43.8	-8.2	25.5
PMMA-TiO2	-22.6	57.9	8.5

*The zeta potential values were estimated from particle mobility measurements (see Figure 6.4).

Table 8.1: Systems examined to study the substrate-particle electrostatic attraction with CSSD experiments.

In order to analyze the morphology of the deposits obtained, we used a white light confocal microscope to extract the morphology information from different profiles of each deposit. The profile of the ring-like deposits was analyzed as explained in Figure 8.13. The red arrow shows the direction along which we acquired the profile of the deposit, characterized by the width (W) and the height (Z). The mean values of the width and the height of the different deposit sections were evaluated over at least five profiles to obtain statistically meaningful features of the deposits formed.

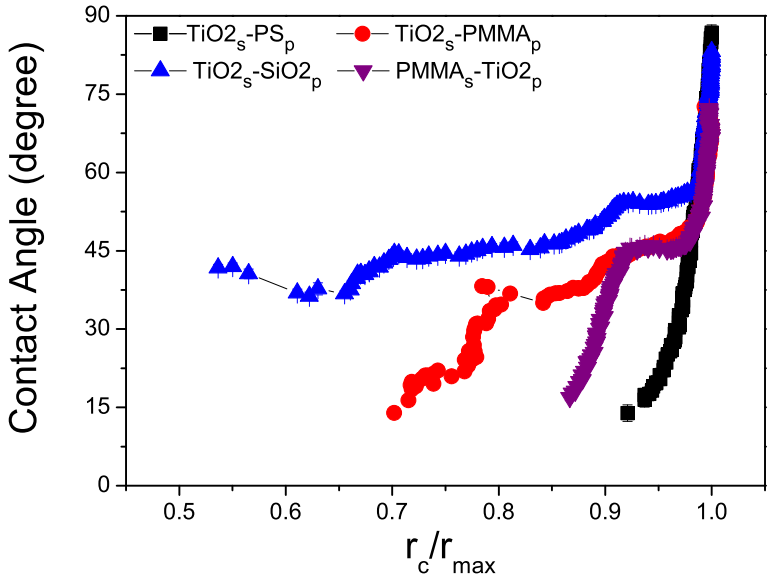

Figure 8.12: CSSD experiments performed on TiO2 and PMMA substrates with PS, PMMA, SiO2-120nm and TiO2 nanoparticles. The subscript in the legend denotes the material that corresponds to the substrate (s) and to the particle (p). The concentration of the particle suspensions was $\Phi_V = 1\%$. It is worth highlighting the different initial contact angle for TiO2 substrates. This effect reveals the variability between samples of TiO2 surfaces due to the strong history dependence (see Section 6.8).

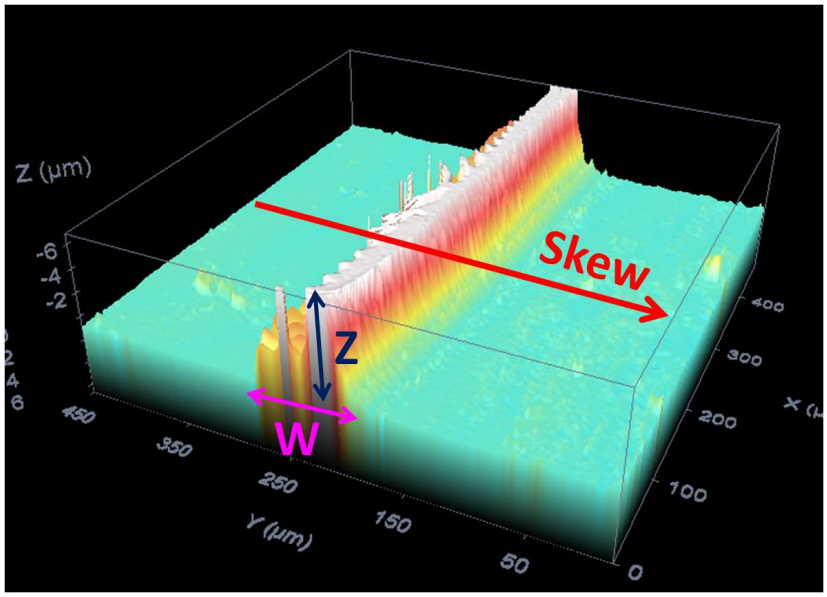

Figure 8.13: Analysis of the profile of the ring-like deposits from the acquired by a white light confocal microscope (PLμ, Sensofar Tech S.L.). The red arrow represents the direction along which we extracted the profile; Stands for the height Z, and W the width.

We analyzed the profiles of the nanoparticle deposits formed with attractive substrate-particle electrostatic interactions for the systems described in Table 8.1. The profiles are shown in Figure 8.14. A peripheral ring followed by a uniform layer was formed with the four systems. The thickness values of each layer are represented by green arrows. The results show that significant differences in the deposit morphology were found for the four systems.

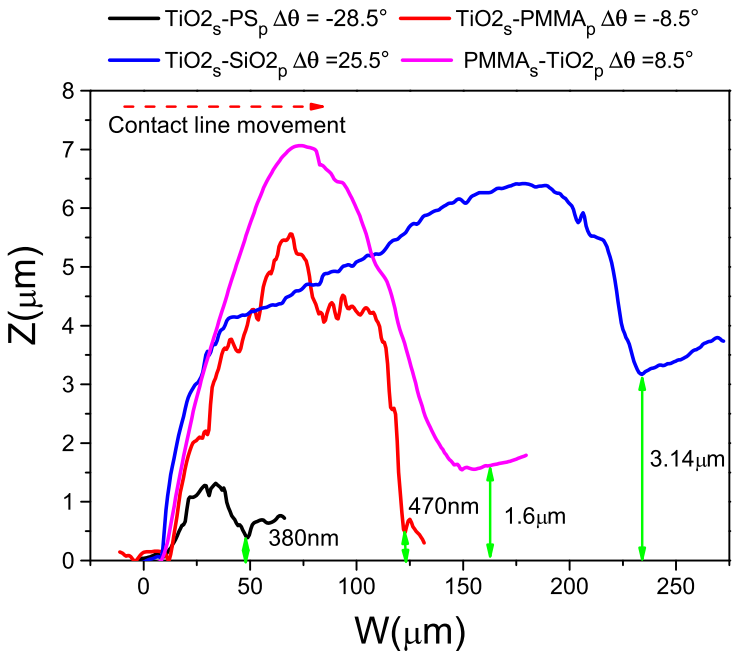

Figure 8.14: Profiles of the ring-like deposits formed with attractive substrate-particle electrostatic interactions. The subscript in the legend denotes the material that corresponds to the substrate (s) and to the particle (p). The green arrows point out the thickness values of each uniform deposit at $\Phi_V = 1\%$.

8.4 Strong substrate-particle repulsion

In the case of free evaporating drops, when there is a strong substrate-particle repulsion, the particles are prevented from contacting the substrate and they follow the convective flow, which is radial toward the contact line. Then, exterior ring-like deposits are expected to occur (37).

We studied the effect of strong substrate-particle repulsion on the contact line dynamics and deposit morphology. Again, we used PMMA and TiO2 substrates to study two receding contact angles. For the PMMA substrates, we prepared PS, SiO2-120nm and TiO2 suspensions buffered at pH9 with a concentration of $\Phi_V = 1\%$. For the TiO2 substrates, we prepared PMMA, PS, TiO2 and SiO2-120nm suspensions also buffered at pH9 with a concentration of $\Phi_V = 1\%$. At this pH value, the particle-particle and substrate-particle electrostatic interactions were enhanced. The systems examined are collected in Table 8.2.

Substrate-Particle	ζ_s (mV)*	ζ_p (mV)*	$\Delta\theta(^\circ)$
PMMA-PS	-50.7	-47.8	-20
PMMA-SiO2-120nm	-50.7	-44.9	40
PMMA-TiO2	-50.7	-44.8	27.8
TiO2-PMMA	-44.8	-50.7	-27.8
TiO2-PS	-44.8	-47.8	-47.8
TiO2-SiO2-120nm	-44.8	-49.9	12.2
TiO2-TiO2	-44.8	-44.8	0

*The zeta potential values were estimated from particle mobility measurements (see Figure 6.4).

Table 8.2: Systems examined to study the strong substrate-particle electrostatic repulsion with strongly interacting charged particles with the CSSD experiments.

The results of contact line dynamics on PMMA and TiO2 substrates are shown in Figures 8.15 and 8.16, respectively. The results were similar in both cases and the contact line behaved in the same way than for pure liquids: no stick-slip behaviour was observed and no particle deposits were obtained.

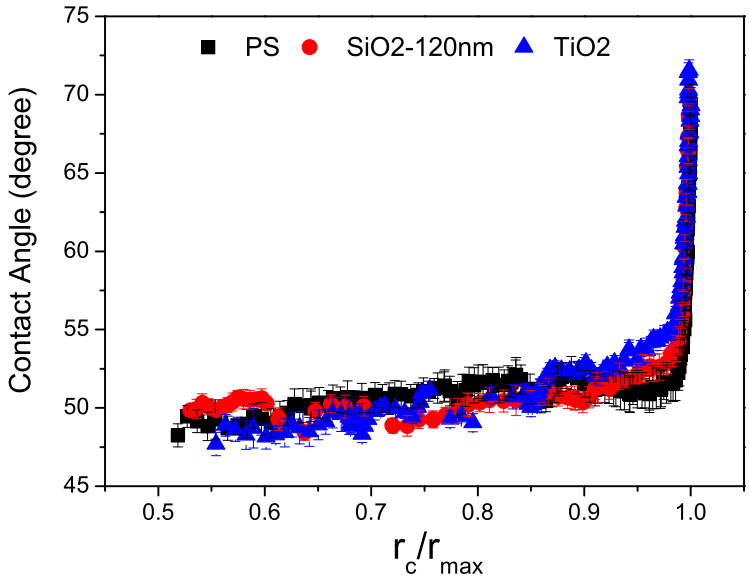

Figure 8.15: CSSD experiments performed on PMMA substrates with PS, SiO2-120nm and TiO2 nanoparticles buffered at pH9 with a concentration of $\Phi_V = 1\%$.

We found with the CSSD experiments that no particle deposits were obtained with strong substrate-particle repulsion. It is plausible to think that in the CSSD experiments if a strong substrate-particle repulsion is revealed, no particle deposits will be obtained and the parameters such as substrate receding contact angle, wettability contrast and particle-particle interactions are unimportant.

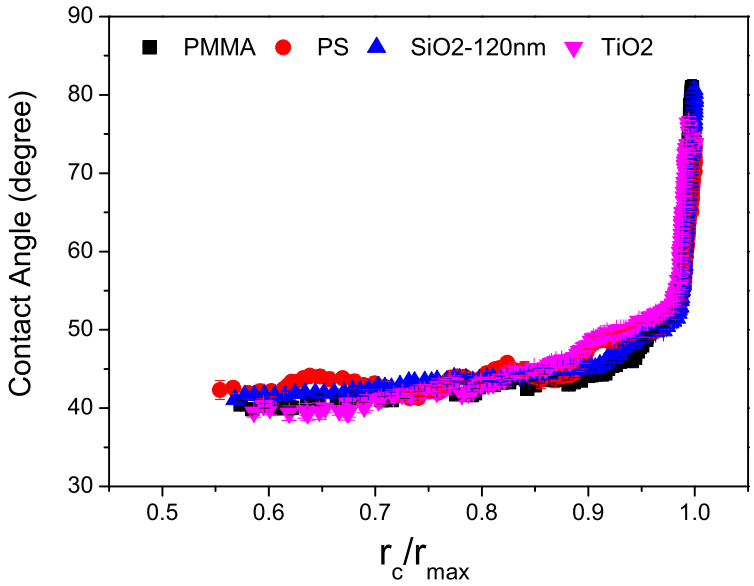

Figure 8.16: CSSD experiments performed on TiO2 substrates with PMMA, PS, SiO2-120nm and TiO2 nanoparticles buffered at pH9 with a concentration of $\Phi_V = 1\%$.

8.5 Weak substrate-particle interaction

Bhardwaj et al. (37) reported that simulations with numerical model based on a finite-element code predict a ring-like pattern with a very thin layer of deposit at the center when the substrate-particle repulsion is weak and the particles are weakly charged. However, the experiments with freely evaporating drops did not reproduce the deposit morphology predicted by the simulations. The experiments showed a deposit profile with flocculated particles. The authors (37) proposed that the reason for this discrepancy was the particle aggregation in bulk mediated by attractive interparticle van der Waals forces. Then aggregates were deposited over the entire area by sedimentation.

In order to test the case of weak substrate-particle interaction, we studied the substrate-particle systems collected in Table 8.3 with the CSSD technique. The results of contact line dynamics are collected in Figure 8.17. Initially, the first pinning due to the contact angle hysteresis of the substrate was observed. Once the contact angle reached the receding contact angle, the contact line receded. During the receding motion, the contact line presented stick-slip events in all the cases till the end of the process. The stick-slip behaviour was more pronounced depending on the wettability contrast of the system. In Figure 8.18 we show the profiles of the deposits obtained for the different substrate-particle systems. The differences in the height and width of the deposits obtained are evident. The wettability contrast was very relevant for the morphology of the final deposit.

Substrate-Particle	ζ_s (mV)*	ζ_p (mV)*	$\Delta\theta(^\circ)$
PMMA-SiO2-120nm	-22.6	-7.9	40
PMMA-PMMA	-22.6	-22.6	0
TiO2-TiO2	12.5	12.5	0
PMMA-PS	-22.6	-49.8	-20
TiO2-PMMA	12.5	-47.8	-14.5

*The zeta potential values were estimated from particle mobility measurements (see Figure 6.4).

Table 8.3: Systems examined to study for the weak substrate-particle interactions with CSSD experiments.

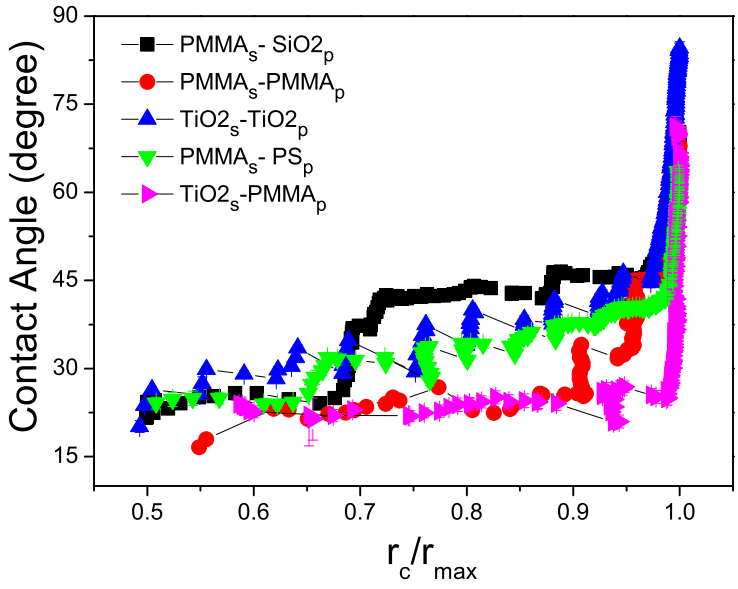

Figure 8.17: CSSD experiments performed to study the weak substrate-particle electrostatic interaction. The substrate-particle systems studied are listed in Table 8.3. The subscript in the legend denotes the material corresponds to the substrate (s) and to the particle (p). The concentration of particle suspensions was $\Phi_V = 1\%$.

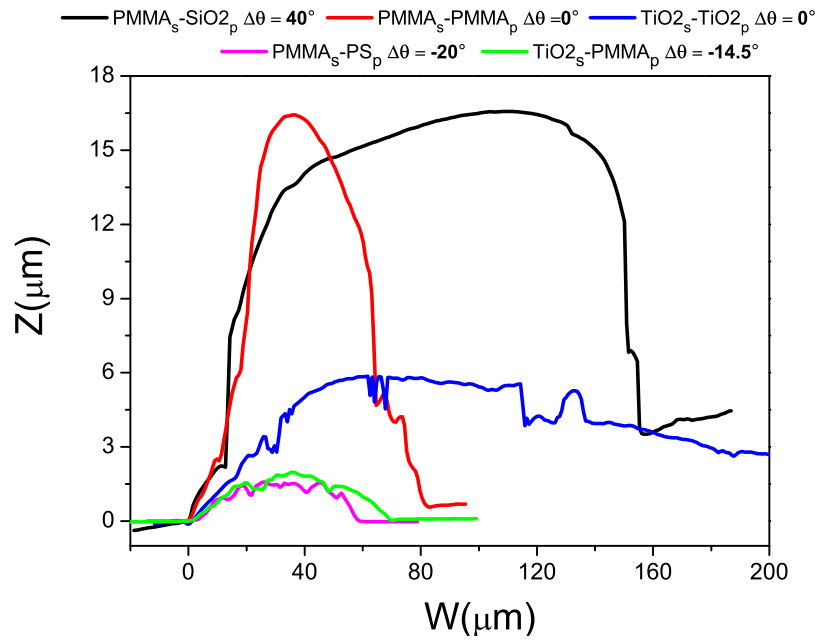

Figure 8.18: Profiles of the ring-like deposits formed with weak substrate-particle interactions. The subscript in the legend denotes the material that corresponds to the substrate (s) and to the particle (p).

8.6 Discussion

We summarize in Figure 8.19 all the CSSD experiments performed for the different substrate-particle systems and the dimensions of the particle deposits obtained.

In order to analyze the differences in the morphology of the ring-like deposits, we plot the lengths of the deposits for each type of substrate-particle interaction. In Figure 8.20 we show the results for the systems with substrate-particle electrostatic attraction. We represent the height (Z) and width (W) of the ring-like deposits extracted from the profile analysis (see Figure 8.13). We also represent $\Delta\theta$ for each interacting substrate-particle system to examine the impact of the wettability contrast on the deposit morphology.

The deposit morphology depends on the following parameters: the strength of the substrate-particle attraction, the particle-particle repulsion, the substrate-particle wettability contrast and the receding contact angle of the substrate. In Figure 8.21 we illustrate the impact of these parameters on the particle deposition. The nanoparticle deposits for each substrate-particle system may be correlated to the magnitude of the substrate-particle electrostatic interaction (Figure 8.21 a). Hence, in the case of high attractive forces, the nanoparticles should be easily deposited on the substrate. The height of the deposit (Z) seems to be directly related with the particle-particle repulsion (Figure 8.21 b). The deposit height should increase when the particle-particle repulsion is weak . The weakly interacting nanoparticles are able to pile up without difficulty. The

Substrate -particle interaction	System (Substrate - Particle)	Wettability contrast Δθ (⁰)	Deposit?	Type	Z (μm)	W (μm)
SPEA	TiO2-PS	-28.5	YES	RING	2.6 ± 0.2	72.5 ±3
SPEA	TiO2-PMMA	-8.5	YES	RING	4.7 ± 0.7	75.6 ± 16
SPEA	TiO2-SiO2	25.5	YES	RING	6.3 ± 0.2	206.2 ±25
SPEA	PMMA-TiO2	8.5	YES	RING	6.2 ± 1	119.7 ± 6
SSPR	PMMA-SiO2	40	NO	-	-	-
SSPR	PMMA-PS	-20	NO	-	-	-
SSPR	PMMA-TiO2	27.8	NO	-	-	-
SSPR	TiO2-PMMA	-27.8	NO	-	-	-
SSPR	TiO2-PS	-47.8	NO	-	-	-
SSPR	TiO2-SiO2	12.2	NO	-	-	-
SSPR	TiO2-TiO2	0	NO	-	-	-
WSPI	PMMA-SiO2	40	YES	RING	14.1 ±2.5	148.8 ±10
WSPI	PMMA-PMMA	0	YES	RING	14.3 ±2.7	65.6 ±1
WSPI	TiO2-TiO2	0	YES	RING	6.8 ±0.7	128.4 ±11
WSPI	PMMA-PS	-20	YES	RING	1.6 ±0.3	54.2 ±8
WSPI	TiO2-PMMA	-14.5	YES	RING	1.9 ±0.03	75.5 ±9

Figure 8.19: Summary table for the nanoparticle deposits obtained from all the CSSD experiments with different substrate-particle systems. The mean values and error bars of Z and W were computed over at least five profiles.

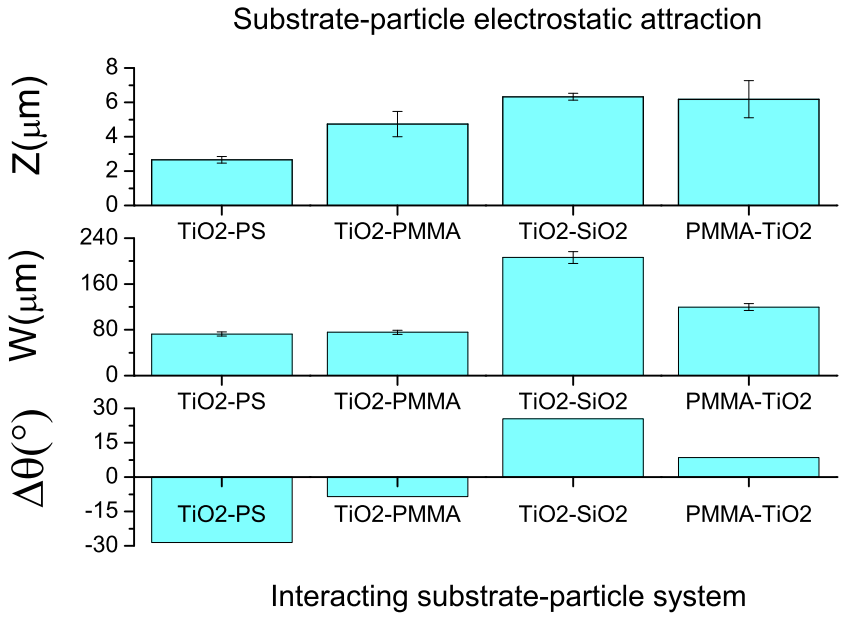

Figure 8.20: Characteristic lengths of the ring-like deposits (Z and W) obtained with substrate-particle electrostatic attraction (see Section 8.3), for different systems. In the last row we plot the substrate-particle wettability contrast.

wettability contrast promotes (or mitigates) the pinning of the contact line (see Section 5.1), thus the accumulation of particles near the contact line is enhanced with positive wettability contrasts. In Figure 8.21 c, we illustrate how the wettability contrast may alter the deposit morphology. With a high wettability contrast, the time that the contact line takes to move from a position S1 to S2 (stick-slip event) can be long or even the contact line can be pinned during the entire process. While the contact line remains pinned, the particles accumulate at the interfacial wedge. On the contrary, if the contact line moves from S1 to S2 in a short time, then less particles will be accumulated. Over a substrate with high receding contact angle, the particles can fill in the wedge vertically rather than over a substrate with lower receding contact angle (Figure 8.21 d). Therefore, higher receding contact angle, greater height of the deposit. The parameters described in Figure 8.21 may be relevant at once with different degree.

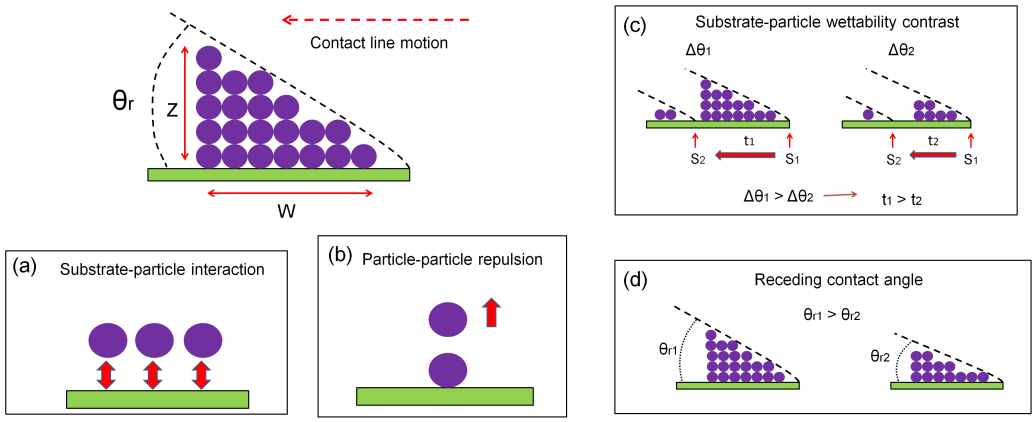

Figure 8.21: Impact of different parameters on the nanoparticle deposition: (a) Substrate-particle interaction, (b) particle-particle repulsion, (c) substrate-particle wettability contrast and (d) receding contact angle of the susbstrate.

To examine the effect of the parameters illustrated in Figure 8.21 on the lengths of the ring-like deposits mediated by substrate-particle electrostatic attraction (see Figure 8.20), the magnitudes of each parameter are shown in Table 8.4. The numbers represent the level of magnitude of each interaction, being 1 the strongest one and 4 the weakest one (see Chapter 6). For all the systems studied, the accumulation of nanoparticles onto the substrate was mainly promoted by the substrate-particle attraction. This way, it is plausible to think that as stronger substrate-particle attraction, higher and wider ring. However, Figure 8.20 shows that the smallest deposits were obtained with the TiO2-PS and TiO2-PMMA systems and, as shown in Table 8.4, the strength of the substrate-particle attraction in these systems was the greatest one. We conclude that the strength of the substrate-particle attraction was not relevant for the lengths (Z and W) of the ring-like deposits formed with substrate-particle electrostatic attraction.

To analyze the differences in the deposit morphology, we compared the results obtained with the TiO2-PS, TiO2-PMMA and TiO2-SiO2-120nm systems, where the receding contact angle re-

System	S-P interaction	P-P interaction	$\Delta\theta$	θ_r
TiO2-PS	1	2	- -	Low
TiO2-PMMA	2	3	-	Low
TiO2-SiO2-120nm	4	4	++	Low
PMMA-TiO2	3	1	+	High

Table 8.4: Magnitude of the determining parameters, shown in Figure 8.21, for the deposit morphology. The numbers represent the strength of each interaction, being 1 the strongest one and 4 the weakest one (see Chapter 6).

mains constant. Thus, the differences observed should be caused by the particle-particle repulsion and the wettability contrast. As shown in Figure 8.21, the higher ring was obtained with the TiO2-SiO2-120nm system followed by the TiO2-PMMA system and finally, the TiO2-PS system. As shown in Table 8.4, this behaviour is connected to the strength of the particle-particle repulsion: weaker repulsion, higher ring. The differences in the width of the ring-like deposits obtained point out to the wettability contrast. The widest ring was obtained with the TiO2-SiO2-120nm system (see Figure 8.21) and, the width of the rings obtained with the TiO2-PMMA and the TiO2-PS systems was similar. As shown in Figure 8.21, the wettability contrast of the TiO2-SiO2-120nm system was positive and negative for the TiO2-PMMA and TiO2-PS systems respectively [c]. The positive wettability contrast prolongs the pinning of the contact line and, as illustrated in Figure 8.21 c, more nanoparticles are accumulated at the contact line.

To study the impact of the substrate receding contact angle on the morphology of the ring, we compared the TiO2-SiO2-120nm and PMMA-TiO2 systems. In both cases the wettability contrast was positive. The wider ring was obtained for the TiO2-SiO2-120nm system, which revealed greater wettability contrast. The height of the ring was similar with both systems. As shown in Table 8.4, the particle-particle repulsion was very different, being the TiO2-TiO2 repulsion much more stronger than the SiO2-SiO2 repulsion. In consequence, the piling up of nanoparticles in the vertical direction should have been mitigated in the PMMA-TiO2 system. However, the PMMA receding contact angle was greater than the TiO2 receding contact angle. As sketched in Figure 8.21 d, once the contact line was pinned (due to the positive wettability contrast), the "wedge effect" in the PMMA-TiO2 system enabled to pile up more nanoparticles in the vertical direction.

In order to analyze the morphology of the ring-like deposits obtained by weak substrate-particle interaction (see Section 8.5), we plot in Figure 8.22 the characteristic lengths of the deposits (Z and W) and the substrate-particle wettability contrast. To examine the effect of the strength of the substrate-particle interaction, the particle-particle repulsion, the substrate-particle wettability

[c] In both cases, the pinning of the contact line was not induced, then no particle deposits was expected to form. However, particle deposits were formed due to the substrate-particle attraction present in all the cases studied (Figure 8.20).

contrast and the receding contact angle on the lengths of the ring-like deposits (Z and W), the magnitude of each parameter is shown in Table 8.5. From Figure 8.22, the higher and wider ring was obtained with the PMMA-SiO2-120nm system. This system reveals the best conditions for the particle deposition: the weakest substrate-particle and particle-particle repulsions, the higher wettability contrast and the higher substrate receding contact angle. The first condition does not impede the particle deposition on the substrate [d]. The second condition promotes the contact line pinning and the third condition enhances the "wedge effect".

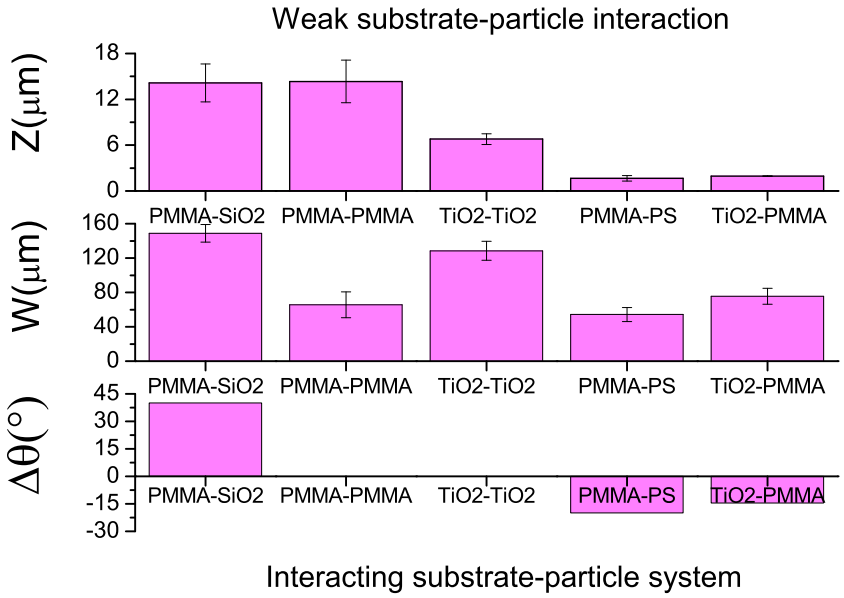

Figure 8.22: Characteristic lengths of the ring-like deposits (Z and W) obtained with weak substrate-particle interaction (see Section 8.5) for different systems. In the last row we plot substrate-particle wettability contrast.

Systems	S-P interaction	P-P interaction	$\Delta\theta$	θ_r
PMMA-SiO2-120nm	5	5	++	High
PMMA-PMMA	3	3	0	High
TiO2-TiO2	4	4	0	Low
PMMA-PS	1	1	- -	High
TiO2-PMMA	2	2	-	Low

Table 8.5: Magnitude of the determining parameters, shown in Figure 8.21, for the deposit morphology. The numbers represent the strength of each interaction, being 1 the strongest one and 4 the weakest one (see Chapter 1) 6.

In the case of the PMMA-PMMA and TiO2-TiO2 systems, both systems had zero wettability

[d] Since the particle-particle repulsion is weak and the nanoparticles are transported to the contact line by the outward flux, then they are confined at the wedge and then, they are attracted by van der Waal forces (see Section 5.2).

contrast. The lengths (Z and W) of the ring-like deposits could be dictated by the substrate-particle repulsion, the particle-particle repulsion and the substrate receding contact angle. The PMMA-PMMA system formed a higher ring than the formed with the TiO2-TiO2 system. This was due to the high receding contact angle of PMMA. The ring obtained with the TiO2-TiO2 system was wider than the obtained with the PMMA-PMMA system. The substrate-particle repulsion of the PMMA-PMMA system was slightly stronger than in the TiO2-TiO2 system. Hence, the TiO2 nanoparticles accumulated on the TiO2 substrate easier. Therefore, the strength of the substrate-particle repulsion becomes relevant for the particle deposition in the horizontal direction.

The PMMA-PS and TiO2-PMMA systems presented negative wettability contrast. In both cases the particle-particle repulsion was alike strong. The rings formed were very similar with small values Z. However, the ring formed with the TiO2-PMMA system was wider. In this case, the substrate-particle interaction was weaker (even attractive) than in the PMMA-PS system, where the particle deposition was less favored.

CHAPTER 9

Effects of particle concentration, size and polidispersity on the deposit morphology

Controlling the particle deposition in a substrate is a main issue to investigate due to the potential applications such as biochip devices, sensors, ultrahigh-density optical and magnetic recording media, etc. Self-assembled 2D colloidal crystals are monolayer arrays of colloidal microspheres or nanospheres, which have a great variety of successful applications in surface patterning such as colloidal lithography. This novel technique is used to fabricate diversify structures scaling down to nanometer features, in which the colloidal particles provide excellent masks or templates. However, the principal requirement for the success of these applications lies in the capability of fabricating colloidal crystals with excellent quality and controlled morphology (**?**).

Drying of a drop of nanoparticle suspension offer many alternatives towards the generation of deposits of nanoparticles on solid substrates. Depending on experimental conditions such as the solid volume fraction or particle size, a variety of morphologies can appear on the substrate (**?**). Many groups have reported the formation of nanoparticle rings, with diameters ranging from a few hundred nm to a few microns (). Due to the complex physical and chemical processes involved in the drying of nanoparticle suspensions, simple strategies as the increment in nanoparticle concentration, are not usually sufficient for the formation of rings of nanoparticles by following

solvent evaporation.

In Chapter 8, we found that particle deposits are obtained with the CSSD technique when the substrate-particle electrostatic interactions are attractive (see Section 8.3) or weak (see Section 8.5). In the present chapter we focused on the variations in the morphology of the particle deposits when parameter such as nanoparticle concentration, pinning time and particle size are changed. We performed CSSD experiments with the different nanoparticle suspensions at pH2 on PMMA substrates. We used this pH because the electrostatic interactions were weak (see Figure 6.4). PMMA substrates were utilized due to their stable response in contact angle (see Section **??**) and the transparency of the material to be analyzed by optical microscopy. The experiments were performed at room temperature (25°C) and relative humidity of 50%.

9.1 Nanoparticles concentration

In Section 8.5, we found that ring-like deposits are obtained with the CSSD technique with different nanoparticle suspensions on PMMA substrates at pH2 (weak substrate-particle electrostatic interactions). In the different experiments performed (see Figure 8.17) the nanoparticle concentration was fixed to $\Phi_V = 1\%$. In the present section we investigate the effects of the solid volume fraction on the deposit obtained with CSSD experiments.

As shown in Chapter 7, in a free evaporating drop of nanoparticle suspensions, the concentration increases during the evaporation and particle deposits are always obtained. However, Stowell et al. (**?**) found that the microscopic morphology of the self-assembled structures formed depends on the starting nanoparticles concentration in the dispersion prior to deposition. By decreasing nanoparticles concentration, the morphology observed changed from rings to polygonal networks, to ordered hexagonal networks, and finally structures without microstructural order. They concluded that dilute solutions are more susceptible to establishing Marangoni convection. Therefore, low concentrations of nanoparticles result in poorly defined structures leading to experimental difficulties in observing the resultant patterns.

Instead, with the CSSD technique, the particle concentration in bulk remains constant during the entire process. We expect to find a critical concentration for ring-like deposit formation. In order to investigate this minimum particle concentration, we performed CSSD experiments with SiO2-90nm suspensions and PMMA substrates at pH2. The nanoparticle concentration was decreased (from $\Phi_V = 1\%$ to $\Phi_V = 0.05\%$) until no particle deposit was obtained. In Figure 9.1 we plot the contact line dynamics of the different experiments. From $\Phi_V = 1\%$ to $\Phi_V = 0.5\%$, the contact line presented stick-slip behaviour, which indicates the existence of particle deposits onto the substrate. At $\Phi_V = 0.1\%$ the contact line presented an irregular receding motion with decreasing contact angle. At $\Phi_V = 0.05\%$, the contact line behaved such as for pure liquids till

$r_c \approx 0.6 r_{max}$, where the contact angle began to decrese during the receding motion. We analyzed the deposits obtained with an optical microscope (Optiphot-2, Nikon) with a 10X objective. The deposits obtained for the different concentrations are shown in Figure 9.2. At $\Phi_V = 1\%$ and $\Phi_V = 0.7\%$ ring-like deposits were obtained [a]. With $\Phi_V = 0.5\%$, a nascent ring was observed. At $\Phi_V = 0.1\%$, just a few branched nanoparticle deposits were formed and finally at $\Phi_V = 0.05\%$, no particle deposits were observed (except for the residual spot found at the center of the substrate). In Figure 9.1, the red arrow indicates that as the particle concentration is decreasing, the receding contact line dynamics tends to the contact line dynamics of a pure liquid.

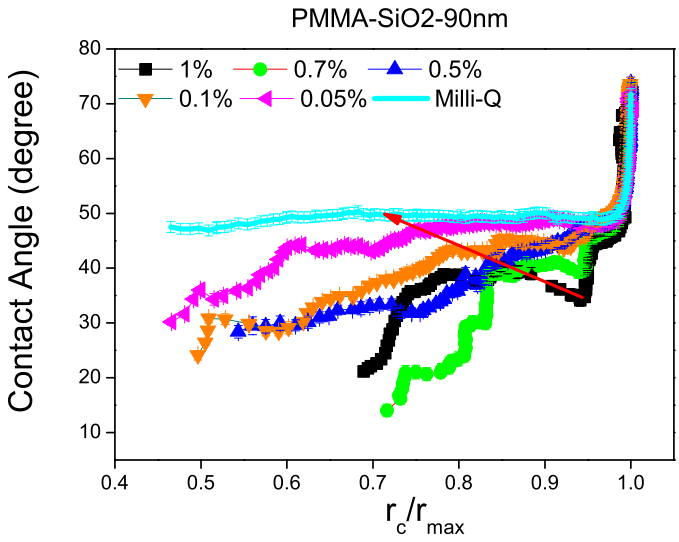

Figure 9.1: Contact line dynamics of SiO2-90nm suspensions at pH2 on PMMA substrates using the CSSD technique. The nanoparticle concentration value was varied from $\Phi_V = 1\%$ to $\Phi_V = 0.05\%$.

We found that with $\Phi_V \geq 0.5\%$ ring-like deposits can be formed with the PMMA-SiO2-90nm system at pH2. Below this concentration, poorly defined structures were formed. These results are in agreement with the found by Stowell et al. (**?**), although they attributed this behavior to a transition from diffusive to convective fluid flow during evaporation. Below a critical concentration, a Marangoni instability occurs giving rise to convective flow. Hu and Larson (**?**) found that Marangoni effect reverses coffee-ring depositions (see Section 5.1). The occurrence of the Marangoni instability depends on the temperature dependence of the surface tension, which was found to depend on the nanoparticles concentration and size. However, with the CSSD technique Marangoni effects are neglected. During the CSSD experiments, the temperature was assumed to be constant along the drop surface because the (macro)evaporation was negligible. Thus, no thermal Marangoni flow was produced. Therefore, the effect of a

[a] The images correspond to the external part of the deposits (a section of the ring), but in the internal part there were nanoparticle deposits (not shown). The internal deposits did not form rings, but according to the concentration, they formed a particulate layer or a branched deposit.

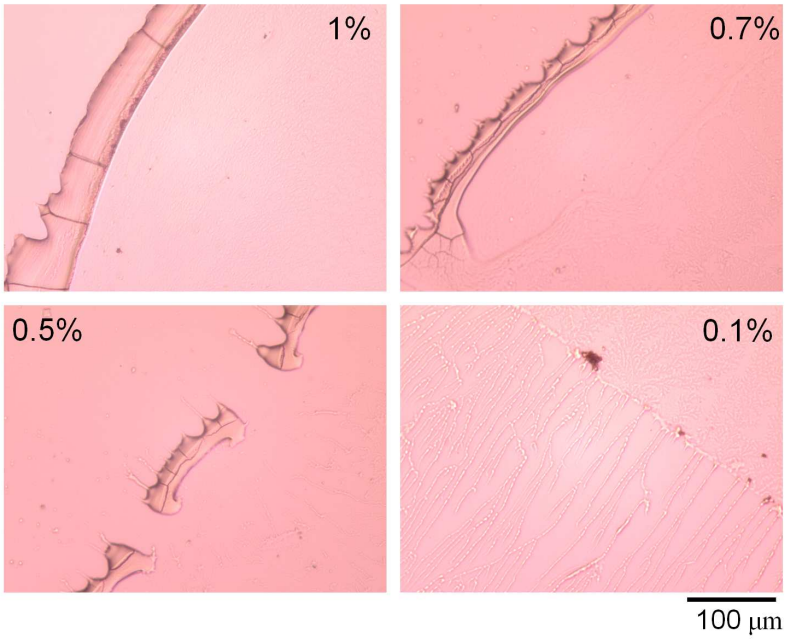

Figure 9.2: Images of the deposits obtained at different concentration. The images were acquired with an optical microscope with a 10X objective. The red arrow indicates the evolution during the receding motion of contact line as the particle concentration is decreasing.

minimal concentration to form a ring-like deposit with the CSSD technique could be due to the poor number of nanoparticles driven to the contact line.

In Chapter 8 we found that a ring-like deposit can be obtained by varying the substrate-particle electrostatic interaction. We also found that the deposit morphology changes as particle-particle electrostatic interaction, the wettability contrast and the substrate receding contact angle. In Figure 9.1 we found that a minimum particle concentration is required to obtain a ring-like deposit. In order to examine the increase the nanoparticle concentration on the morphology of the deposits, we performed CSSD experiments with SiO2-20nm suspensions at pH2 on PMMA substrates. The concentration was increased from $\Phi_V = 1$ to 10%. The contact line dynamics presented stick-slip behaviour with concentrations from $\Phi_V = 1$ to 5%, but at $\Phi_V = 7$ and 10% the contact line remained pinned for the entire process (see Figure 9.3). The red arrow in the figure, shows that as the particle concentration increases the contact line dynamics turns from a free receding motion (pure liquid) to a total contact line pinning.

We analyzed the deposit profiles obtained with a white light confocal microscope (PLμ, Sensofar Tech S.L.). The results are shown in Figure 9.4. The width and height of the external ring increased with the concentration from $\Phi_V = 1$ to 3%. At $\Phi_V = 5\%$, instead of a wider and higher ring, two ring-like deposits were obtained. At $\Phi_V = 7\%$, a wide ring followed by a layer was found. With $\Phi_V = 10\%$ an irregular layer was obtained. We observed that ($\Phi_V \geq 3\%$

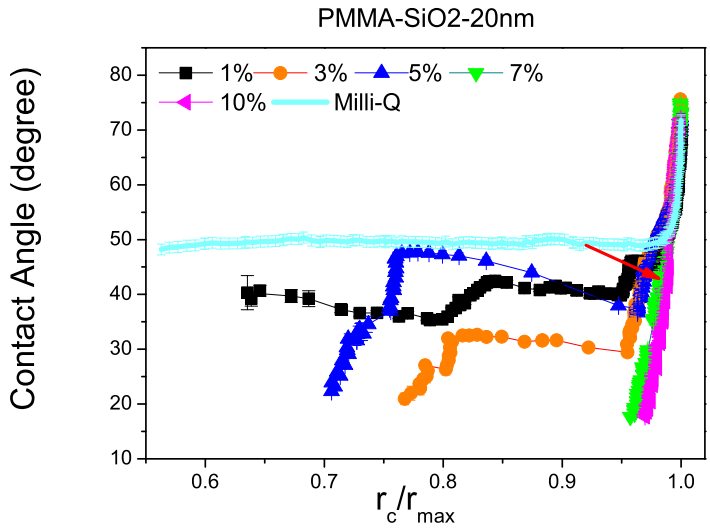

Figure 9.3: Contact line dynamics of SiO2-20nm suspensions at pH2 on PMMA substrates using the CSSD technique. The concentration value was varied from $\Phi_V = 1$ to 10%. The red arrow indicates the variation in the contact line from a free receding motion (pure liquid) to a total contact line pinning.

excluding 5%), increasing the particle concentration, the width of the ring-like deposit increased, whereas the height increased up to certain value ($\approx 16.5\mu$m). Then the particle deposits grew in the horizontal direction as a varying thickness layer.

9.2 Pinning time

Shen et al. (**?**) found that, for a free evaporating drop of nanoparticle suspensions, there are two time scales relevant for the formation of ring-like deposits. One is the related to the loss of liquid, which dictates the time allowed for the particles to accumulate within the drop. They proved that in a colloidal drop, when a fast evaporation of the liquid is induced, the particles do not have enough time to accumulate at the contact line while it remains pinned. Hence, no ring-like deposits are formed after evaporation even if there are an adequate number of particles. Another important time scale is the time necessary for two neighbor particles near the contact line to meet each other. This time is determined by the dominating transport mechanism responsible for bringing the particles into contact and forming the initial particle accumulation. During the initial particles deposition, the particles can be transported to the contact line by the induced capillary flow, diffusion, or by a combination of these two mechanisms (see Section 5.1).

According to the results obtained with the CSSD technique (see Chapter 8), we found that the particles deposition occurred at the first contact line pinning (see Figures 8.7 and 8.10). The first contact line pinning is due to the contact angle hysteresis of the substrate. The contact line

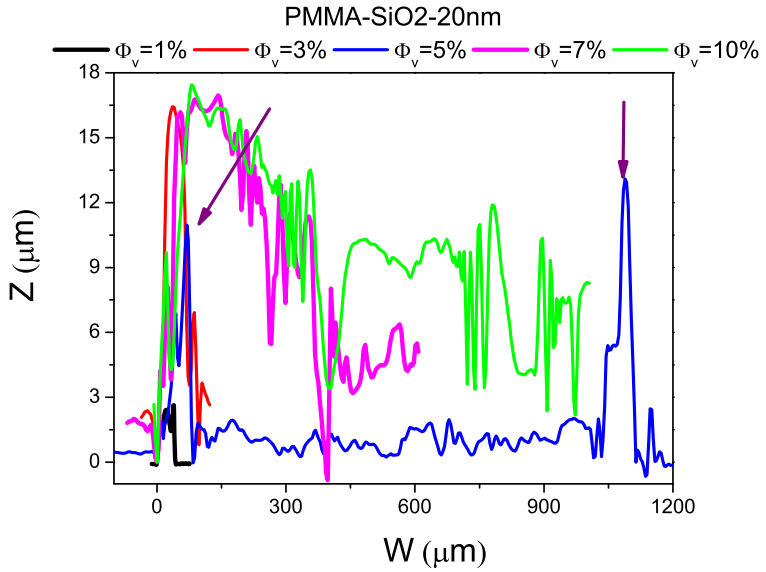

Figure 9.4: Profiles of the ring-like deposits formed with SiO2-20nm suspensions on PMMA substrates at different concentration. The arrows indicate the positions of the two rings formed at $\Phi_V = 5\%$.

remains pinned till the contact angle reaches the receding contact angle. For a freely evaporating drop, the initial contact angle [b] decreases up to the receding contact angle and then the contact line recedes. We refer to this time period as "pinning time". With the CSSD technique, the pinning time can be intentionally varied (increased or decreased see Section 2.5).

We splitter the total length of the CSSD experiments in two periods that we called pinning time (t_p) and receding time (t_r) of the contact line. The pinning time in the CSSD technique, is the time necessary to reach the receding contact angle from the advancing contact angle. In order to increase or decrease this time, the liquid withdrawal flow rate was changed accordingly. In Figure 9.5 the two time scales are arbitrary illustrated. In order to study the impact of the pinning time on the particle deposition, we carried out CSSD experiments with decreasing pinning time from t_p=140s to 30s but with constant receding time (t_r=483s). We performed CSSD experiments with Milli-Q water on PMMA substrates to examine if the contact line dynamics was affected with the reduction of the pinning time. The results showed that the contact line behaved in the same way for two different pinning times (see Figure 9.6).

To study the effect of the reduction of pinning time in CSSD experiments with complex fluids, we prepared SiO2-90nm suspension buffered at pH2 and $\Phi_V = 1\%$ on PMMA substrates. We reduced the pinning time from the standard value (140s) to 30s (as in Figure 9.6). The results are shown in Figure 9.7. As expected, the contact line remained pinned till the contact

[b] In a free evaporating drop, as the drop is placed on the substrate, the initial contact angle is lower than the advancing contact angle i.e. the maximum contact angle (see Section **??**). However, as happens with the CSSD technique, the initial contact angle reproduced with a growing drop is the advancing contact angle

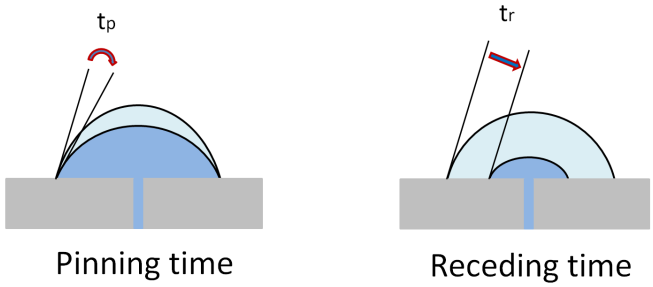

Figure 9.5: Sketch of the pinning and receding times during a CSSD experiment.

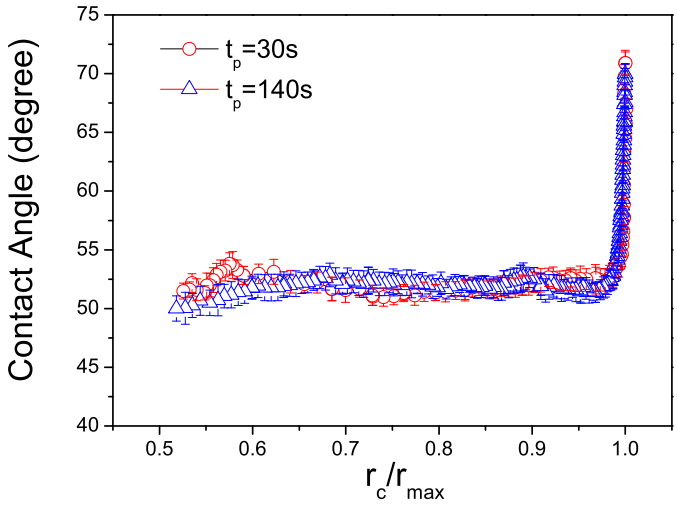

Figure 9.6: Contact line dynamics of Milli-Q water on PMMA substrates during two CSSD experiments with different pinning time.

angle reached the receding contact angle, then the contact line receded. As shown in the green rectangle, the contact line freely moved from $r_c = r_{max}$ to $r_c \approx 0.9 r_{max}$. During this receding motion, no particle deposits were obtained. From the receding motion ($r_c < 0.9 r_{max}$) till the end of the process (red rectangle), isolated nanoparticle deposits were obtained. These nanoparticle deposits produced were revealed by irregular contact line dynamics. As described in Section 8.5, the same substrate-particle system and particle concentration, the standard CSSD experiment produces ring-like deposits. On the basis of the results obtained we concluded that if the pinning time is reduced during CSSD experiments, no ring like deposits can be obtained. The results are in agreement with those obtained by Shen et al. (**?**) for free evaporating colloidal drops.

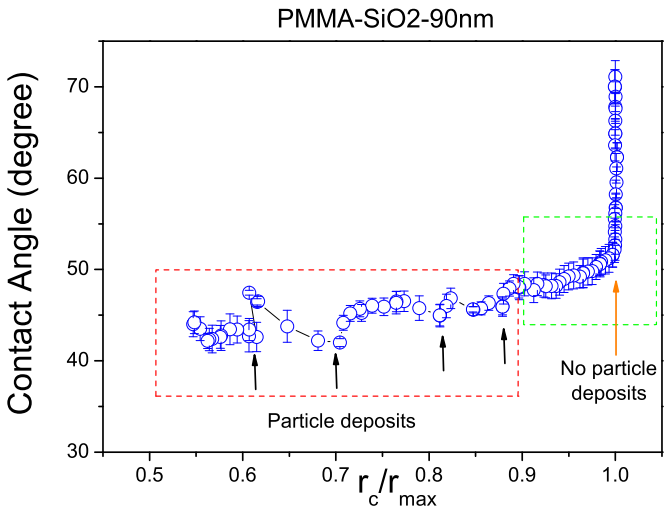

Figure 9.7: Contact line dynamics of SiO2-90nm suspensions buffered at pH2 and $\Phi_V = 1\%$ on PMMA substrates using the CSSD technique with t_p=30s. The black arrows indicate the position where nanoparticle deposits can be localized.

In order to study the relevance of the increase of pinning time in CSSD experiment for the morphology of the ring-like deposits, we performed CSSD experiments with increasing pinning times, but constant receding time. The different times are shown in Table 9.1.

Experiment	Total time (s)	Pinning time (s)	Receding time (s)
CSSD	623	140	483
CSSD-2	756	273	483
CSSD-3	810	327	483
CSSD-4	944	461	483

Table 9.1: Time intervals of different CSSD experiments where the pinning time was increased. The first row correspond to the CSSD experiments described in Section 2.5.

In order to investigate the effect of increase t_p in CSSD experiments with nanoparticle sus-

pensions, we prepared PMMA suspensions at pH2 and $\Phi_V = 1\%$. The CSSD experiments were performed on PMMA substrates. We used PMMA suspensions on PMMA substrates to eliminate the effect of the wettability contrast on the results obtained. The substrate-particle and particle-particle electrostatic interactions were weak (see Figure 6.4), the wettability contrast was zero and the results obtained were only consequence of the pinning time and the nanoparticle concentration value. The contact line dynamics of the different CSSD experiments is shown in Figure 9.8. The CSSD, CSSD-2 and CSSD-3 provided similar contact line dynamics. A first pinning was observed, the contact angle decreased up to the PMMA receding contact angle and the contact line moved back. During the receding motion of the contact line, a marked stick-slip behavior was observed and a final ring-like deposit was formed. However, with CSSD-4, the contact line remained pinned while the contact angle decreased up to $\approx 20°$. Next, the contact line receded till the process finished. During the receding motion, stick-slip behaviour was also observed. The final deposit was also a ring. We analyzed the deposits obtained with a white light confocal microscope. In Figure 9.9, the profiles of the ring-like deposits obtained for the different CSSD processes are shown. As expected, the width and height of the ring-like deposit increased as pinning time. The deposit produced with the standard CSSD was the smallest and thinner ring. The deposits obtained with CSSD-2 and CSSD-3 were similar, due to the similar pinning time of these processes. The ring-like deposit formed with the CSSD-4 was clearly the higher and wider ring.

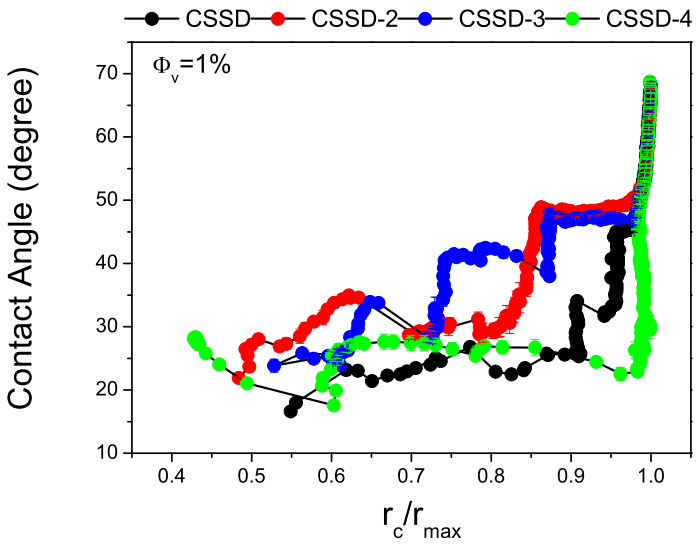

Figure 9.8: Contact line dynamics of different CSSD experiments with increasing pinning time (see Table 9.1). The experiments were performed with PMMA suspensions at $\Phi_V = 1\%$ and pH2 on PMMA substrates.

To study the relevance of the nanoparticle concentration in the ring formation when the pinning time is increased and the particle concentration is varied, we performed the CSSD experiments listed in Figure 9.1 with PMMA suspensions on PMMA substrates at Φ_V =0.1 and 5% and pH2.

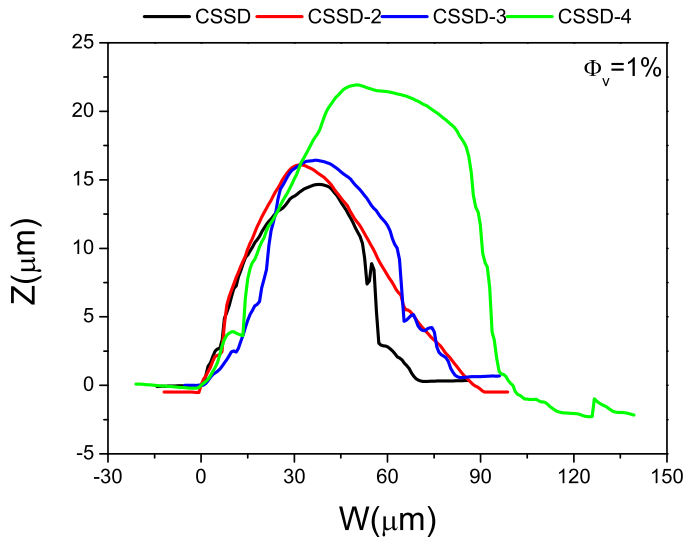

Figure 9.9: Profiles of the ring-like deposits formed with PMMA suspensions on PMMA substrates at $\Phi_V = 1\%$ and pH2, with CSSD experiments at different pinning times (see Figure 9.1).

With the standard CSSD experiment (t_p=140s) at $\Phi_V = 0.1\%$, the contact line behaved such as for pure liquids till r_c=0.62r_{max}, where a pinning event was observed. Next, the contact angle decreased while the contact line receded till the process finished. Instead of ring-like deposits, just a few deposits were formed. With the CSSD-2 process, irregularities in the contact line motion were observed during the drop receding. Alike CSSD experiments, primitive nanoparticle deposits were observed. With the CSSD-3 process, from the first pinning event, three marked pinning events were formed. The final deposit was a thin nascent ring. With the CSSD-4 process, the contact line was pinned from the beginning of the process, the contact angle decreased up to $\approx 30^\circ$ and then the contact line receded. During the receding motion, several stick-slip events were observed. The final deposit was a thin ring. The results obtained show that with a low nanoparticles concentration, the deposits appear when the pinning time is increased. When the pinning time is long enough, the nanoparticles can be transported to the contact line and they form a ring-like deposit. Due to optical limitations of our confocal microscope the profiles of the deposits formed could not be analyzed.

With $\Phi_V = 5\%$ (see Figure 9.11), the results showed that the contact line remained macroscopically pinned during the entire process except for the standard CSSD experiment in which, after the first pinning event, the contact line receded for a short time until it was strongly pinned. The contact line jumped with a very low contact angle $\approx 15^\circ$ and receded till the process finished. Alike with $\Phi_V = 1\%$, in the four CSSD experiments, ring-like deposits were obtained although they were higher and wider than the deposits obtained with $\Phi_V = 1\%$. The profiles of the ring-like deposits are plotted in Figure 9.12. With CSSD, CSSD-2 and CSSD-3, the width and height of the ring deposit increased as the pinning time, being the profiles obtained with CSSD-2 and

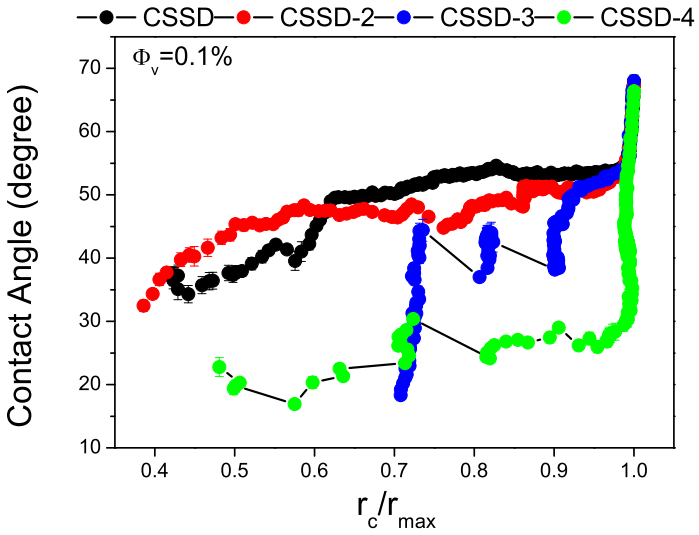

Figure 9.10: Contact line dynamics of different CSSD experiments with increasing pinning time (see Table 9.1). The experiments were performed with PMMA suspensions at $\Phi_V = 0.1\%$ and pH2 on PMMA substrates.

CSSD-3 processes very similar. Instead, with CSSD-4, the higher and wider ring was formed again but it was followed by a thick layer ($\approx 15\mu$m).

In Section 9.1 we found that as the concentration of nanoparticles in the bulk liquid increases, more nanoparticles are driven to the contact line. Furthermore, we have found that increasing the pinning time in CSSD processes the same effect can be achieved (see Figures 9.10, 9.8 and 9.11).

9.3 Particle size and binary suspensions

During the evaporation of a drop containing particles, there exists a finite empty zone between the edge of the particle monolayer and the pinned contact line (**?**). The radial length of this region remains constant over a wide range of drop sizes, but it depends on the particle size and concentration (**?** **?**) as well as the local contact angle (see the "wedge" effect in Section 8.6). Since the thickness of the drop meniscus reduces gradually toward the contact line, particles transported by the flow created inside the drop are deposited at a position where the individual particle size matches the thickness of the local meniscus. Consequently, smaller particles are expected to move closer to the contact line compared to the larger ones, which leads to size-dependent particle separation (see Figure 9.13). Hence, the "coffee ring" effect can result in size dependent nano/microparticle separation near the contact line region of an evaporating liquid drop. This enables for a simple chromatography technique for processing biological entities with minimal resource requirements (**?**).

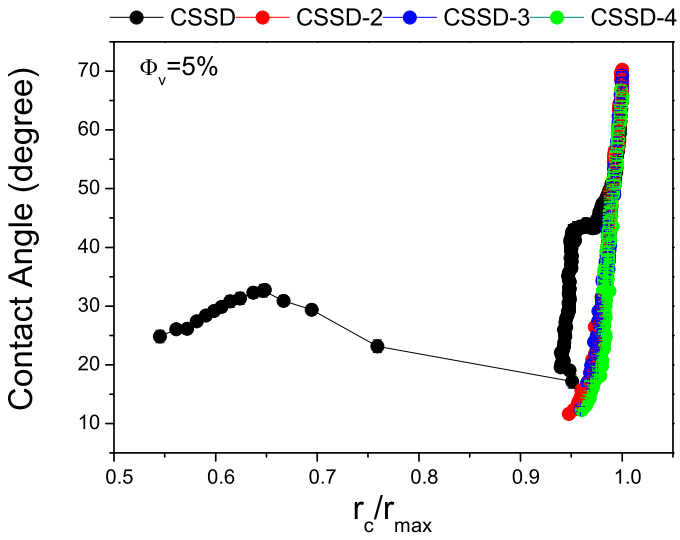

Figure 9.11: Contact line dynamics of different CSSD experiments with increasing pinning time (see Table 9.1). The experiments were performed with PMMA suspensions at $\Phi_V = 5\%$ and pH2 on PMMA substrates.

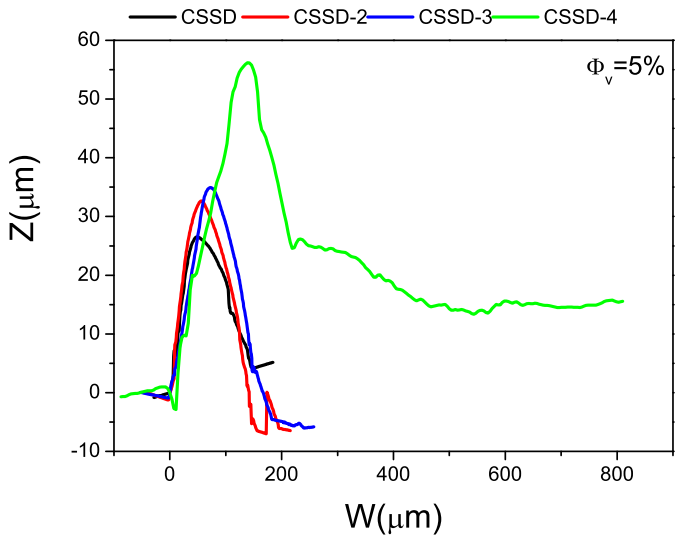

Figure 9.12: Profiles of the ring-like deposits formed with PMMA suspensions on PMMA substrates at $\Phi_V = 5\%$ and pH2, with CSSD experiments at different pinning times (see Figure 9.1).

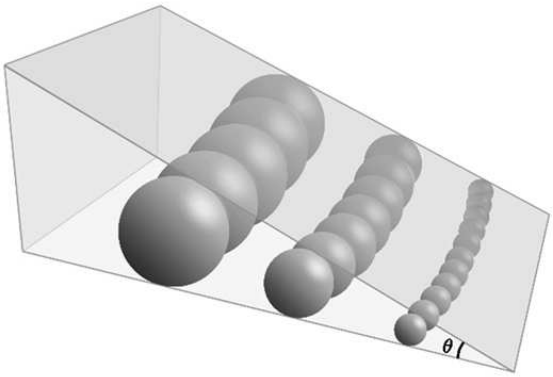

Figure 9.13: Schematic representation of the "wedge effect" where the particles are separated as sizes. The substrate contact angle is represented by θ.

As described in Chapter 8, the CSSD technique allows to standardize the contact line dynamics of an evaporating drop in a shorter time interval. Moreover, undesired effects due to the increment of the particle concentration during the loss of liquid are worded because the particle concentration in bulk during the entire CSSD process was constant. In order to test the CSSD technique with particles of different size, we performed experiments with SiO2-20nm, SiO2-120nm and SiO2-1.16μm suspensions on PMMA substrates at $\Phi_V = 1\%$ and pH2. Under these conditions, the particle deposits were not affected by substrate-particle and particle-particle electrostatic interactions, wettability contrast, receding contact angle or particle concentration. We found that ring-like deposits were obtained with the three different particle sizes. The main differences of the deposits obtained were the lengths of each deposit (the height, width and diameter of the ring). In Figure 9.14, we plot the profiles of the deposits acquired with a white ligth confocal microscope. As expected, the higher and wider ring was the formed with the SiO2-1.16μm suspensions. Thus, the height and width of the ring-like deposit directly depend on the size of the particle at fixed concentration. In consequence, the ring diameter was reduced as the size of particles increased. At the same volume fraction, smaller nanoparticles provide a greater number concentration, have a greater mobility and they accumulate closer to the contact line thanks to the "wedge effect".

For free evaporating drops, Perelaer et al. (**?**) found that for larger particles there is a greater difference between initial drop diameter and the dried drop diameter. The distance between the contact line and the deposited particles depends on the contact angle that the solvent forms with the substrate and the size of the suspended particles (see "wedge effect" in Figure 9.13). Hence, the results obtained with the CSSD technique with different particle sizes are in agreement with the behaviour of an evaporating drop. The CSSD technique enables the nano/microparticle segregation near the contact line region.

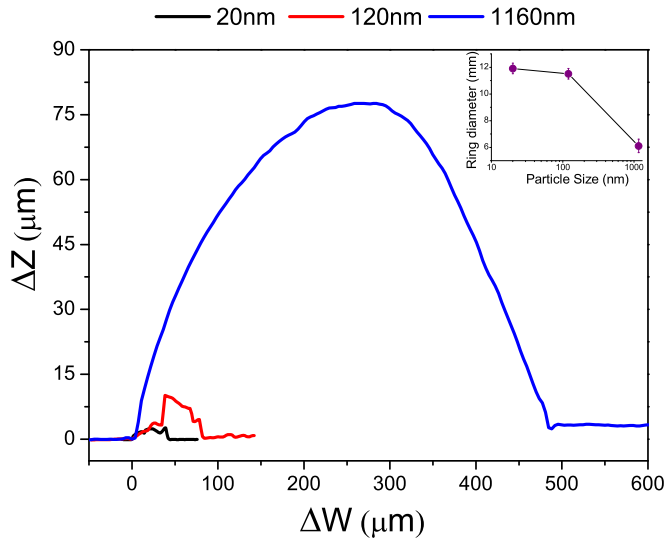

Figure 9.14: Profile of the ring-like deposits obtained with CSSD experiments using SiO2-20nm, SiO2-120nm and SiO2-1.16μm suspensions on PMMA substrates at $\Phi_V = 1\%$ and pH2. The diameter of the ring-like deposits is plotted as function of the particle size (log scale).

In order to examine the particle-size selection near the contact line of an evaporating drop, we performed free evaporation experiments of mixtures 1:1 (1%-1%) and 5:1 (5%-1%) of SiO2-120nm and SiO2-1.16μm suspensions at pH2 on PMMA substrates. The drop volume was 100μl. In Figure 9.15, top view images of the deposits obtained are shown. With the mixture 1:1, a ring-like deposit was formed followed by a layer. The ring was separated from the layer. With the mixture 5:1, a donut-like deposit was formed also followed by a layer. Due to the height of the donut-like deposit we could not analyzed it with our microscopes. In the case of the mixture 1:1, due to optical limitations, we separately analyzed the ring and the layer. To analyze the ring deposit, we used atomic force microscopy and the images of the layer were acquired using an optical microscope with a 40X objective. The images are shown in Figure 9.16. The AFM image verifies that the ring was mostly formed by SiO2-120nm nanoparticles, although a few SiO2-1.16μm particles can be observed. The image of optical microscopy shows that the layer was mainly formed by SiO2-1.16μm particles.

From the results obtained in Figure 9.14, we found that using the CSSD technique small particles are able to penetrate further into the edge of the drop. In order to test if the CSSD technique can be also used to separate mixtures of particles, we performed CSSD experiments on PMMA substrates with a mixture 1:1 of SiO2-120nm and SiO2-1.16μm suspensions at pH2. In Figure 9.17, the contact line dynamics is shown. The contact line was pinned at the beginning of the process. When the PMMA receding contact angle was reached, the contact line receded just a small distance (≈ 0.1mm) and next, it was again pinned. At r_c=5.6mm, a jump was observed right down to r_c=4.6mm where the contact line was markedly pinned till the end of the process.

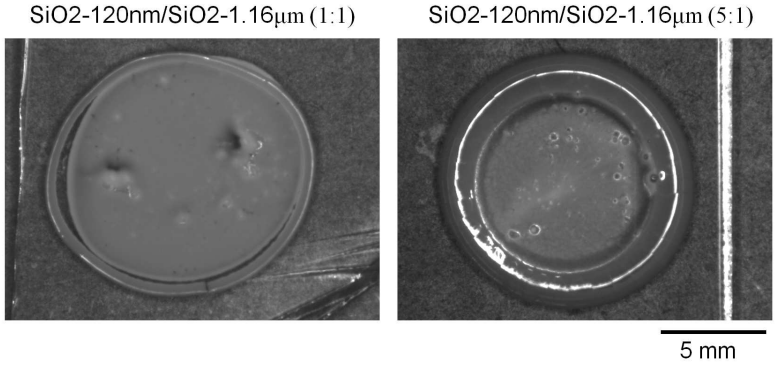

Figure 9.15: Top-view images of the deposits obtained with free evaporation experiments of mixtures 1:1 and 5:1 of SiO2-120nm and SiO2-1.16μm suspensions at pH2 on PMMA substrates. The drop volume was 100μl.

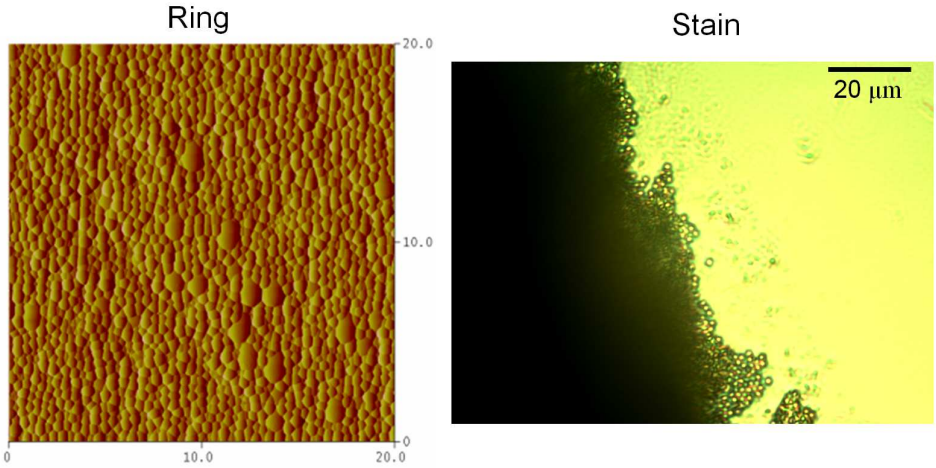

Figure 9.16: Images acquired with AFM (left) and optical microscopy (right) of the ring-like and layer deposits obtained with drop evaporation experiments of a mixture 1:1 of SiO2-120nm and SiO2-1.16μm suspension on a PMMA substrate at pH2.

These pinning events point out to the formation of a ring followed by a layer. This layer should be separated of the ring as happens in the case of drop evaporation experiments (see Figure 9.16). The first pinning event occurred at r_c=5.6mm, this means that the deposit formed should have a diameter of 11.2 mm. We found that the diameter of the ring obtained in a CSSD experiment with SiO2-120nm nanoparticles was 11.5 mm (see Figure 9.14). The next pinning event occurred at r_c=4.6mm. This means that the diameter of the layer should be 9.2mm. This estimation does not correspond to the diameter of the ring observed in CSSD experiments with SiO2-1.16μm particles. This is explained by the previous history of the contact line.

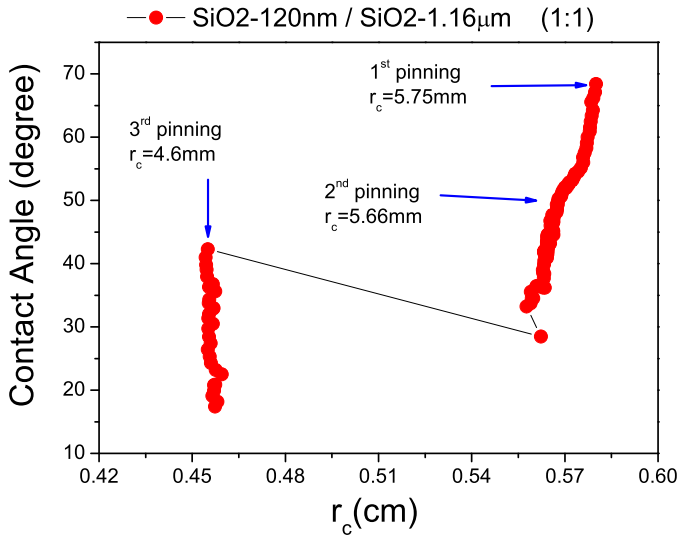

Figure 9.17: Contact line dynamics during a CSSD experiment with a mixture 1:1 of SiO2-120nm and SiO2-1.16μm suspension at pH2 on a PMMA substrate. The red arrows indicate the position of the pinning events.

In order to analyze the deposits formed, we acquired images of different sections of the deposit using an optical microscope. A sequence of images (starting from the outer part) of the deposit formed is shown in Figure 9.18. The contact line dynamics (see Figure 9.17) showed that, after the first pinning event, the receding movement of the contact line did not take place at constant contact angle. Instead, the contact angle decreased while the contact line receded a very short distance ($\approx 90\mu$m) till the second pinning event occurred. This behaviour could be due to that, during the receding motion of contact line, a few particles were deposited from Figure 9.18 a, a first deposit is created during the first pinning event. It was a very thin ring-like deposit followed by branched deposits. These deposits appear to be formed only with SiO2-120nm nanoparticles. In Figure 9.18 b, the initial part of a ring-like deposit preceded by finger-like deposits is observed. The ring seems to be formed by SiO2-1.16μm particles resting on SiO2-120nm nanoparticles deposits. In Figure 9.18 c, the last part of the ring in Figure 9.18 b is shown. The ring formed is followed by SiO2-120nm branched-like deposits. Figure 9.18 d shows the finger-like deposits of SiO2-120nm nanoparticles left during the first contact line receding. The deposit formed during

the third pining event is shown in Figure 9.18 e, where a thin ring was mostly formed by SiO2-120nm nanoparticles, with a few SiO2-1.16μm particles, followed by a stain. The stain is mainly formed by SiO2-1.16μm particles. Finally, in Figure 9.18 f, the central part of the final deposit is shown. We observed that, in the inner part, only SiO2-1.16μm particles were deposited.

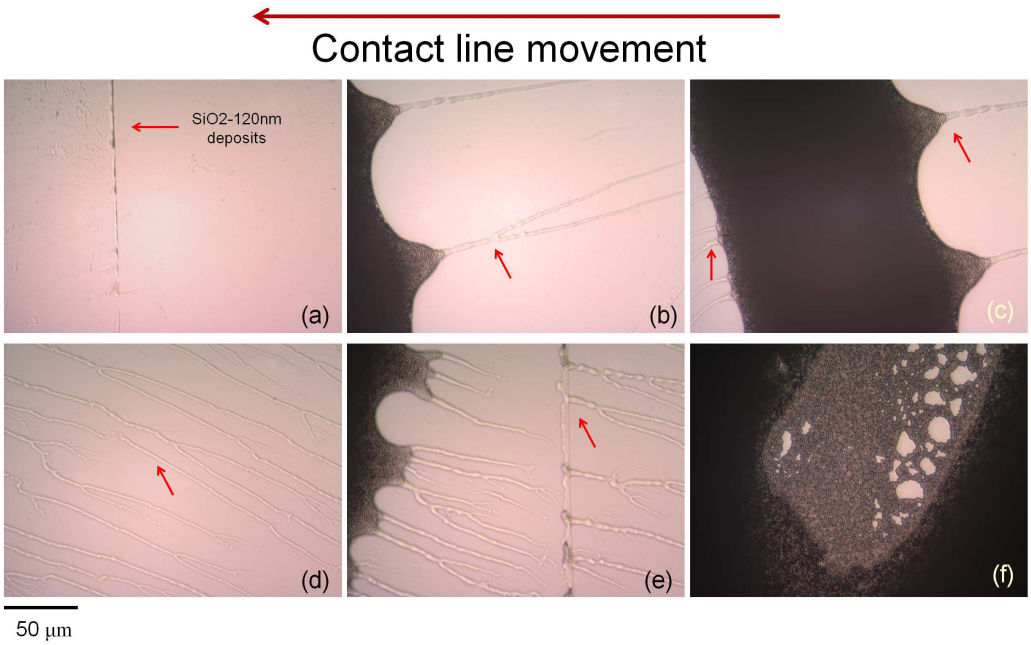

Figure 9.18: Sequence of images acquired with an optical microscope of the deposit obtained with CSSD experiments of a mixture 1:1 of SiO2-120nm and SiO2-1.16μm suspension at pH2 on PMMA substrates. The red arrows indicate some positions where the SiO2-120nm nanoparticles were deposited.

To investigate the variation in the particle deposit when the concentration of particles is changed, we prepared a mixture 5:1 of SiO2-120nm nanoparticle suspension at $\Phi_V = 5\%$ and SiO2-1.16μm particles suspensions at $\Phi_V = 1\%$ at pH2 on PMMA substrates. The contact line dynamics show (Figure 9.19) that after the first pinning event, the contact line receded just a short distance, the contact angle was decreasing during this brief receding motion. After that, a jump was observed and then the contact line again pinned (second pinning event) till the end of the process.

To study in detail the deposit obtained, we acquired images using an optical microscope. In Figure 9.20, we present a sequence of images of the particle deposit (from the outer part to the center). In Figure 9.20 a, the initial part of a ring-like deposit is observed. In the outer part, the ring is formed by a band of the SiO2-120nm nanoparticles (indicated by the red arrows), then the SiO2-1.16μm particles can be observed. From Figure 9.20 b, the ring-like deposit is followed by branched-like SiO2-120nm deposits. In Figure 9.20 c, after the branched-like SiO2-120nm deposits, we observe again a band of SiO2-120nm nanoparticles followed by a stain of SiO2-1.16μm particles. Finally in Figure 9.20 d, a section of the central part of the final deposit is

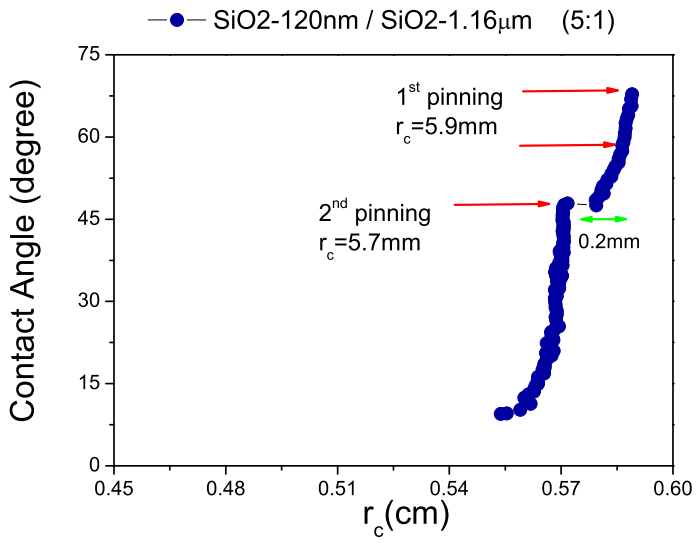

Figure 9.19: Contact line dynamics during CSSD experiments with a mixture 5:1 of SiO2-120nm and SiO2-1.16μm suspension at pH2 on PMMA substrates. The red arrows indicate the position of the pinning events and the green one indicates the distance between the first and second pinning events.

shown. A stain formed by both SiO2-120nm and SiO2-1.16μm particles is observed. The smaller particles are in the bottom of the stain and the bigger ones on the top.

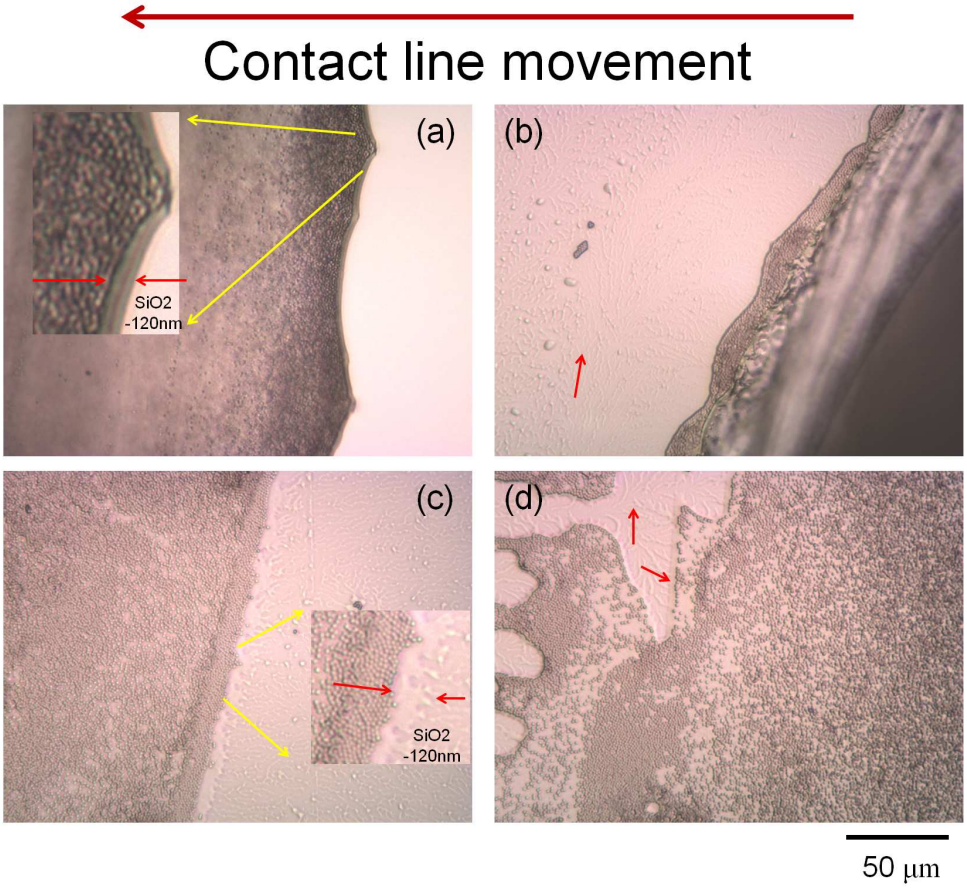

Figure 9.20: Sequence of images acquired with an optical microscope of the deposit obtained with CSSD experiments of a mixture 5:1 of SiO2-120nm and SiO2-1.16μm suspensions at pH2 on PMMA substrates. The red arrows indicate positions where SiO2-120nm nanoparticles were deposited.

CHAPTER 10

Conclusions

Receding contact lines of complex liquids

Moving drops are an efficient way of collecting nanoparticles. The activated dynamics of the contact line enables the directional drying of colloidal suspensions. The "coffee stain" effect in the deposit formation produced by driven contact lines can be suppressed on electrically charged substrates. We have found that, varying the medium pH, the "coffee stain" effect can be canceled provided that the substrate is weakly charged and the loss of drop volume is driven from the drop bulk. The deposit morphology can be modulated by the wettability contrast between substrate and particle and the pinning time. This opens up a new method of controlling deposition patterns through change of substrate electric charge and the particle-substrate wettabillity contrast.

English

The most important conclusions of the part II of this work are summarized as follows:

i. With Controlled Shrinking Dessile Drop (CSSD) experiments of nanoparticle suspensions at free pH, no deposits are obtained even by varying particle volume fraction and particle size.

ii. The weak substrate-particle and particle-particle electrostatic interactions enhance the pinning of the contact line for free evaporating drop of nanoparticle suspensions.

iii. No particle deposit is obtained with the CSSD technique when the substrate-particle electrostatic repulsion is strong.

iv. Ring-like deposits are obtained with the CSSD technique when there exist substrate-particle electrostatic attraction and weak substrate-particle interaction.

v. The morphology of the nanoparticle deposits are modulated at different degree by the following parameters: the strength of the substrate-particle interaction, the particle-particle repulsion, the substrate-particle wettability contrast and the substrate receding contact angle.

vi. A minimum particle concentration is required for ring-like deposit produced with the CSSD technique.

vii. As particle concentration increases, the ring formed with the CSSD technique increases in thickness and height till reach a maximum height. Above certain concentration, the ring becomes a particulate film.

viii. The pinning time is a relevant parameter for the deposit formation. No particle deposits are found if the pinning time is reduced. However, an increase of pinning time enables the ring formation even at low particle concentration.

ix. The CSSD technique enables the nano/microparticle segregation near the contact line region.

Español

Las conclusiones más importantes de la parte II de este trabajo están resumidas a continuación:

i. No se encontraron depositos de partículas utilizando la técnica CSSD con suspensiones de nanopartículas a pH libre, y en donde la concentración y tamaño de partícula fueron variados.

ii. En experimentos de evaporación libre donde las interacciones electrostáticas sustrato-partícula y partícula-partícula fueron debilitadas vía pH del medio, se encontró que el anclaje de la línea de contacto fué reforzado, impidiendo el retroceso de la línea de contacto.

iii. No se obtienen depositos de partículas mediante la técnica CSSD con suspensiones de nanopartículas donde las interacciones electrostáticas partícula-sustrato son altamente repulsivas.

iv. Depósitos en forma de anillo se obtienen con la técnica CSSD cuando las interacciones electrostáticas sustrato-partícula son atractivas o débiles.

v. La morfología de los depósitos pueder ser modulada a diferentes grados por parámetros como la intensidad de las interacciones electrostáticas sustrato-partícula, partícula-partícula, el contraste de mojabilidad sustrato-partícula, así como el ángulo de retroceso del sustrato.

vi. Una mínima concentración de partículas es requerida para la formación de depositos en forma de anillo con la técnica CSSD.

vii. Cuando la concentración de partícula es incrementada, el anillo formado con la técnica CSSD aumenta en grosor y altura hasta llegar a una altura límite, en la cual el incremento en concentración conlleva al engrosamiento del anillo hasta convertirse en una película.

viii. El tiempo de anclaje de la línea de contacto es un parámetro relevante en la formación de depósitos. Con la técnica CSSD se ha encontrado que reduciendo éste tiempo, se carece de formación de anillos. Sin embargo, incrementando el tiempo de anclaje se favorece a la formación de anillos aún a concentraciones bajas de partículas.

ix. La técnica CSSD es capaz de discriminar el tamaño de partícula llevando las más pequeñas cerca de la línea de contacto y transportando las más grandes al centro de la gota.

Part III

Appendices

APPENDIX A

What means hysteresis?

Hysteresis is a general phenomenon, which is encountered in many types of systems. Notable examples include magnetic, mechanical and absorption hysteresis. However, it is not obvious to explain contact angle hysteresis from the same arguments used in Magnetism. Some general definitions and comments about hysteresis may be very useful in understanding the theory of contact angle hysteresis (69).

A.1 Memory, dissipation, branching and metastability

Hysteresis represent the history dependence of physical systems. The statement that, in a system exhibiting hysteresis, future evolution depends on past history, is probably the most common way to present hysteresis. According to this viewpoint, a system with hysteresis is a system with path-dependence or *memory*.

A second definition of hysteresis is based on the existence of domains (interacting or noninteracting), each of which exhibits an irreversible transition ("jump") between two states. The correspondence between hysteresis and *dissipation* naturally arises from the idea that hysteresis is an out-of-equilibrium phenomenon, where irreversible processes take place.

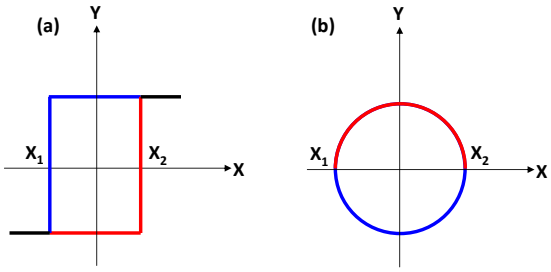

Figure A.1: (a) A simple example of hysteresis behaviour, demonstrating branching; (b) an example of a multi-valued function which is not hysteretic because it does not exhibit branching.

As third definition, a system is considered to exhibit hysteresis if the independent variable has a multibranched non-linearity relation with the dependent variable. It is clear that *branching* will be possible when the independent variable is a multi-valued function. However, a multi-valued dependence is a not sufficient condition for establishing hysteresis, since branching is the essencial point. For example, in Figure A.1a, the variable Y may branch when the variable X takes the extreme values X_1 or X_2 but this is not possible in Figure A.1b.

The presence of a multivalued property of a system implies the existence of metastable equilibrium states (*metastability*). But metastability is just a necessary condition for hysteresis. For this reason, the connection between hysteresis and metastability should be carefully used.

A.2 Adhesion hysteresis

Contact angle hysteresis is related to the more general phenomenon known as *adhesion hysteresis* (134). When two surfaces come in contact, the energy required to separate them is always greater than the energy gained by bringing them together (hysteresis), and thus the attaching-detaching cycle is a thermodynamically irreversible dissipative process. Israelachvili argued that hysteresis is a result of reorganisation of the surface in contact with the test liquid, at macroscopic, microscopic or molecular level (134). This phenomenon is observed during solid-solid and solid-liquid contacts (150), like in those AFM experiments performed in a liquid environment, where the probe tip comes into contact with the sample and then detaches from it (Figure A.2). Dissipation manifests itself as a hysteresis of the force versus displacement curve. This behaviour can be illustrated using a macroscopic analogy.

Let be two approaching magnet surfaces. The lower one is fixed and the other is subjected to the end of a spring of stiffness K (see inset of Figure A.3). Both surfaces interact via an attractive potential with a hard-wall repulsion at some cut-off separation (Figure A.3). As the two surfaces are brought together from separations x larger than x_2, the spring deflects toward contact to reach

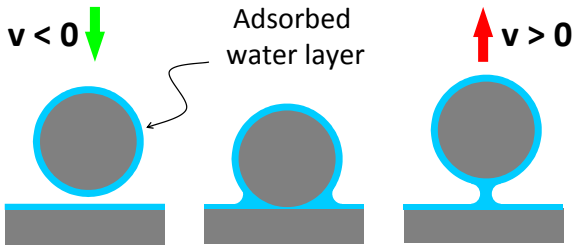

Figure A.2: Adhesion hysteresis.

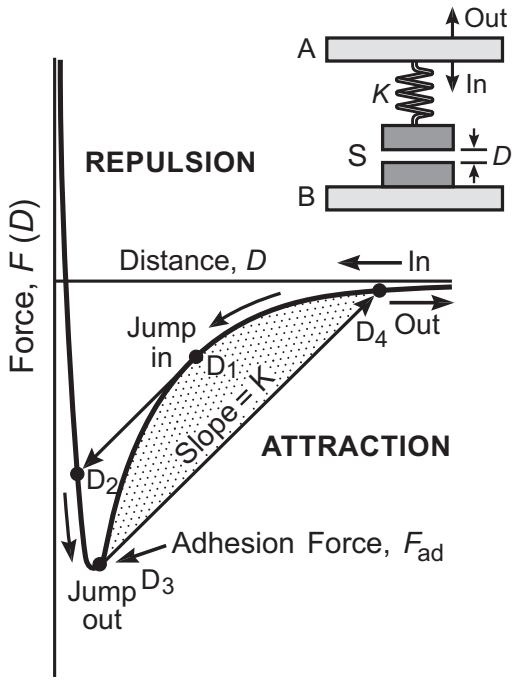

Figure A.3: Macroscopic "magnet" analogy of adhesion hysteresis.

mechanical equilibrium (i.e., the spring force matches the attractive force between the surfaces). However, beyond the point x_2 at which the gradient of the interaction force equals the spring constant K, mechanical equilibrium is no longer possible, and the separation distance jumps to x_4. When the movement is reversed, the same thing happens again and x jumps from x_3 to x_1. By using springs of different spring constant K, one can also measure the force between the surfaces for $x_2 > x > x_3$. It is worthy to point out that the elastic and Lennard-Jones forces do not provide a mechanism of energy dissipation by itself because both forces are conservative separately. Both potentials have well-defined equilibrium states at different distances. However, a nonreversible process can be visualized if both forces act simultaneously and the magnitude of one changes with time. In fact, the elastic force depends on two variables: the position of the ceiling and the relative position of the upper surface with respect to the ceiling. As the ceiling moves, the elastic force changes implicitly as time. Thus the elastic force is non-conservative (dissipative interaction) and the combined potential can have more than one minimum point (150).

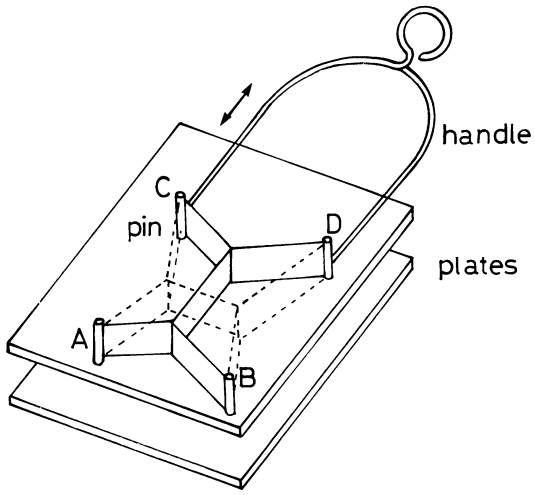

Figure A.4: Device for illustrating adhesion hysteresis.

A.3 Illustrating adhesion hysteresis using soap film patterns

Soap films provide excellent examples of patterning that arises from simple balancing of forces and minimizing of energy (151, 152). The energy of a soap film pattern is directly proportional to the total surface area of film. Hence soap films attempt to minimize their area in order to reach equilibrium.

Let be two parallel horizontal plates with four vertical pins between them (see Figure A.4). This set is inserted into and then withdrawn from a soap solution. As consequence, a film is established connecting the pins together. In Figure A.4, pins A and B are fixed while pins C and

D are moved together so that ABCD is always a rectangle. If movement of pins C and D is slow, the film alters such that it always maintains its equilibrium shape. Since the separation of the plates is constant, the total length of the film can be used as a measure of its energy and the gradient (force), a shape which corresponds to minimum length. The complete range of changes is shown in Figures A.5-A.7.

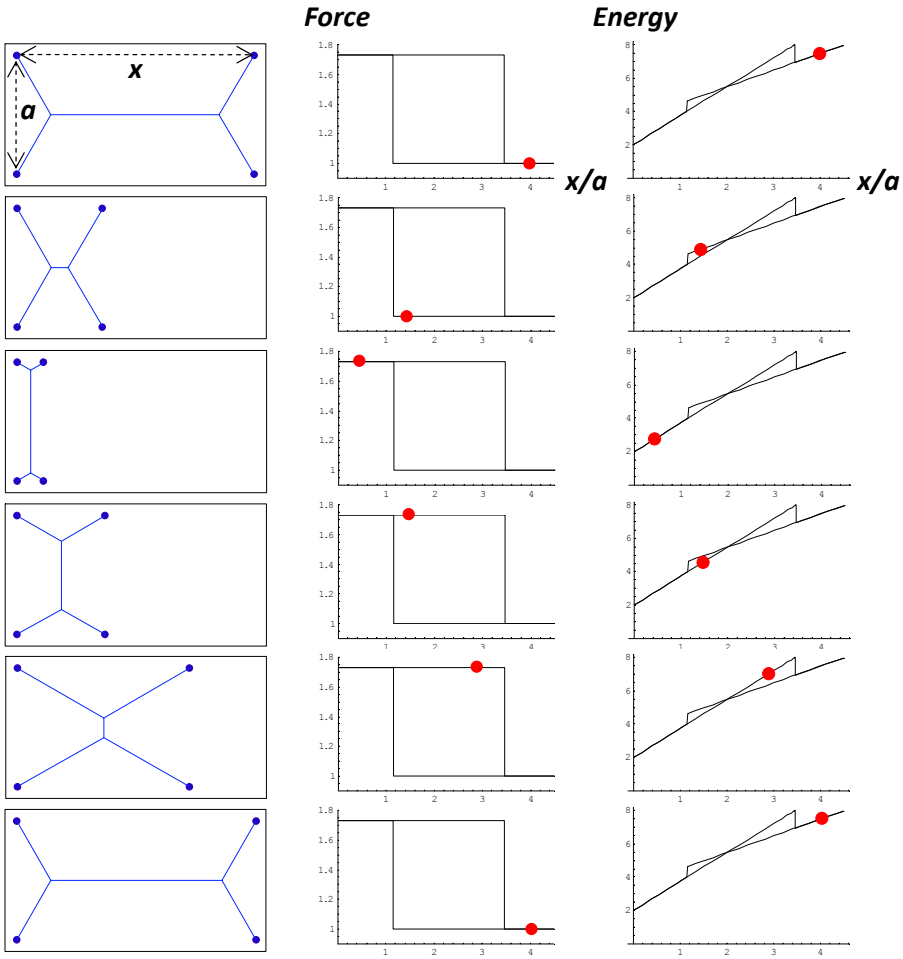

Figure A.5: Variation of film force and energy (length) with the control length x for a fixed value of a, during an approach-separation cycle.

A.4 Correlation friction-contact angle hysteresis

It is wrong to think that hysteresis arises because of some imperfection in the system such as rough or chemically heterogeneous surfaces, or because the supporting material is viscoelastic. Adhesion hysteresis can arise even between perfectly smooth and chemically homogeneous surfaces supported by perfectly elastic materials. Adhesion hysteresis may be caused by mechanical

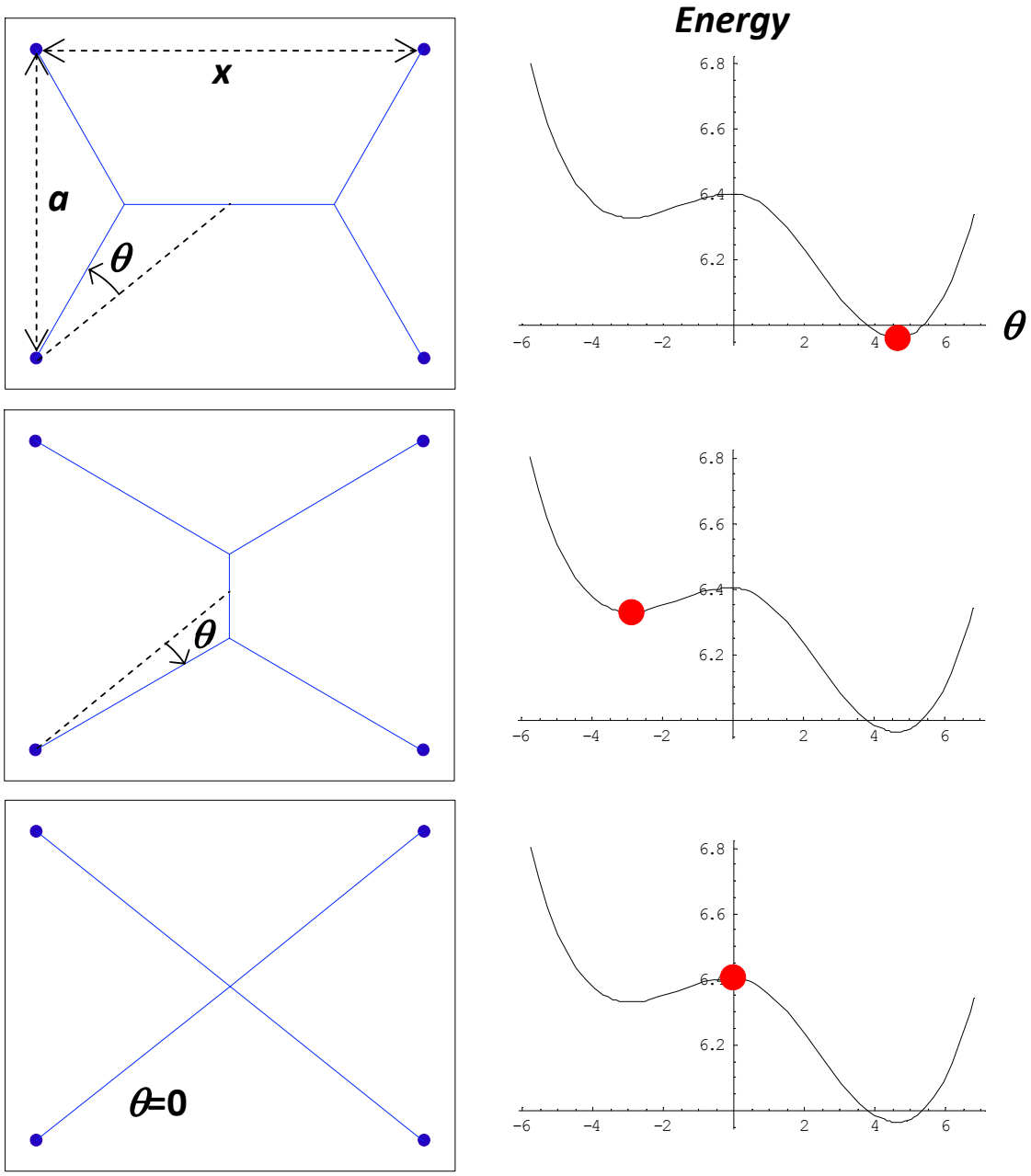

Figure A.6: Variation of film energy (length) with the configuration parameter θ for both fixed values of a and x. There are three possible metastates: two stable configurations and one unstable. From the unstable configuration, the system can relax suddenly ("jump") towards one of the stable configurations.

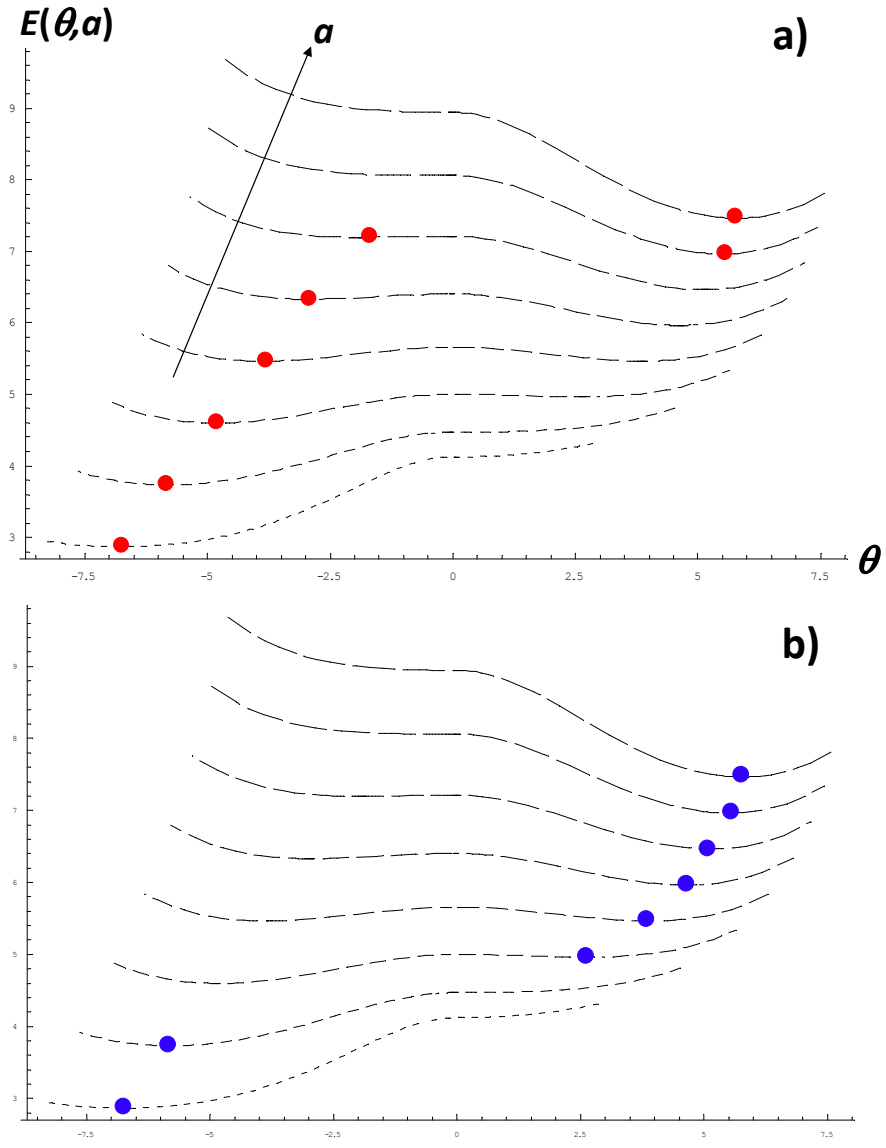

Figure A.7: Variation of film energy (length) with the configuration parameter θ for different values of a (size parameter) and a fixed value of x. The points represent the metastates occupied during the dilatation mode (a) and the shrinkage mode (b)

effects such as instabilities, or chemical effects such as interdiffusion, interdigitation, molecular reorientations and exchange processes occurring at an interface after contact. Such processes induce roughness and chemical heterogeneity even though initially (and after separation and reequilibration) both surfaces are perfectly smooth and chemically homogeneous.

Adhesion hysteresis is also observed during a solid-solid contact (150). Friction forces have been shown to be proportional to the adhesion hysteresis, as discussed by Israelachvili (153). The friction coefficient is not directly correlated with adhesion but rather with the adhesion hysteresis, which is a measure of the energy dissipated during an irreversible adhesion (e.g. approach-separate) cycle.

Contact angle hysteresis is usually illustrated as a frictional effect (e.g. the motion of a body on a tilted plane, stick-jump events...). But, in fact, friction is a consequence of adhesion hysteresis magnified by roughness accordingly. In the friction between two solids, the real microscopic contact area is considered as a constant. Unlike, in the case of a liquid drop on a solid, the real microscopic contact area can strongly change as the hygrohilicity/hygrophobicity of the surface or the imposed motion. Hence, the analogy friction-contact angle hysteresis should be carefully invoked since that the dissipative mechanisms underlying in contact angle hysteresis indeed explain the friction, not the opposite one.

Reducing the friction of liquid flows on solid surfaces has become an important issue with the development of microfluidics systems, and more generally for the manipulation of fluids at small scales.

APPENDIX B

How does the volume of a sessile drop scale with contact radius?

Many experimental and theoretical studies on wetting phenomena usually apply the spherical drop approximation. This model is valid when the gravity is negligible or for small drops, i.e. when the apex curvature radius of the drop, R_{ap}, is much lower than the *capillary length*[a], l_0, of the liquid. This regimen is referred to as capillary regime.

For a spherical cap with a contact angle θ, the volume V depends on the contact radius r_c as follows:

$$V = \frac{\pi}{6} r_c^3 \left(\tan^2 \frac{\theta}{2} + 3 \right) \tan \frac{\theta}{2} \tag{B.1}$$

But, how does the volume of a gravity-distorted drop change as the base radius? Gravity force breaks the surface-to-volume scaling of sessile drops.

Volume, contact angle and contact radius of gravity-distorted drops are related in a closed-

[a] $l_0 = \sqrt{\gamma_{LV}/(\Delta\rho g)}$, where $\Delta\rho$ stands for the density difference and g is the local gravity. For water at 25°C, l_0=2.71 mm

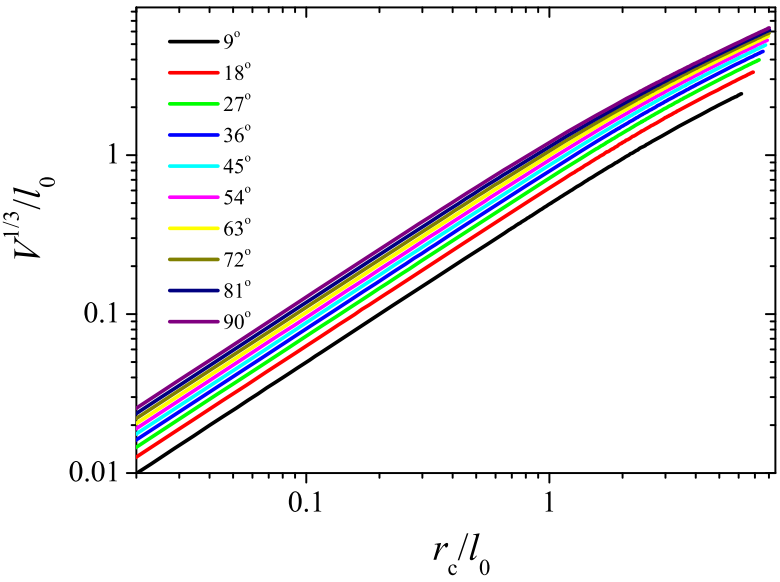

(a)

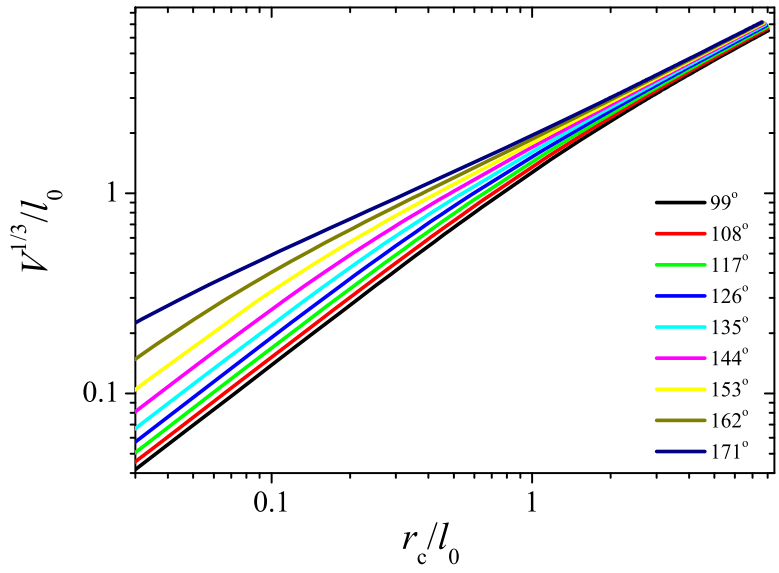

(b)

Figure B.1: Cube root of drop volume normalized by the capillary length as function of the dimensionless contact radius for contact angles (a) lower than $90°$ and (b) greater than $90°$.

form (154) as follows:

$$\frac{V}{l_0^3} = 2\pi \frac{r_c}{l_0} \left(\left(\frac{l_0}{R_{ap}} + \frac{h}{2l_0} \right) \frac{r_c}{l_0} - \sin\theta \right) \tag{B.2}$$

where the apex curvature radius and the drop height h also appear. These extra dependences complicate the behavior $V - r_c$ (see Fig. B.1).

For a wide range of (r_c/l_0)-values (nine orders of magnitude of drop volume), the data displayed in Eq. B.1 can be fitted, on average, to a power law such as:

$$\frac{V}{l_0^3} \propto f(\theta) \left(\frac{r_c}{l_0} \right)^{3\alpha\left(\theta, \frac{r_c}{l_0}\right)} \tag{B.3}$$

where f is a unknown function of the contact angle and the α-exponent is an effective parameter that depends on the contact angle and the dimensionless contact radius.

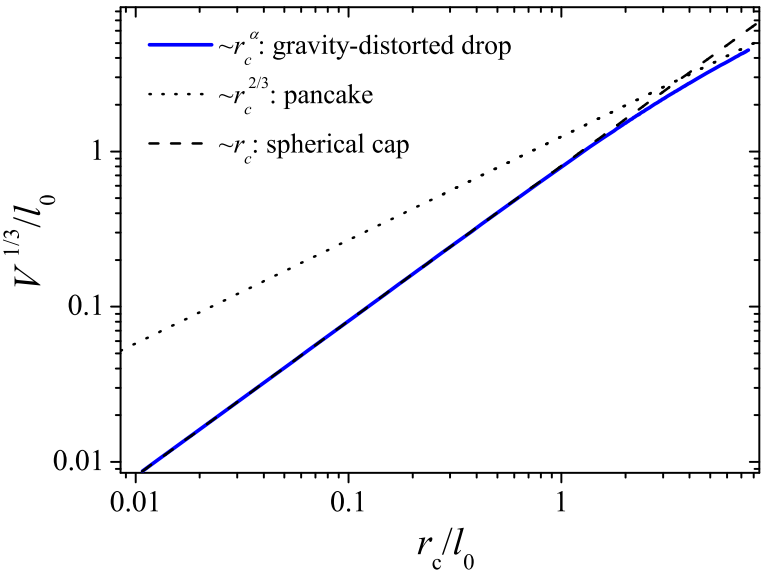

Figure B.2: Cube root of drop volume normalized by the capillary length as function of the dimensionless contact radius for $\theta = 36°$. Three cases were plotted: a gravity-distorted drop (solid line), a pancake (dotted line) and a spherical drop (dashed line).

For the case of a "pancake" drop ($R_{ap}/l_0 \gg 1$ and $r_c/l_0 \gg 1$), where gravity force dominates over surface tension[b], Eq. B.2 can be simplified to:

$$\frac{V}{l_0^3} \approx 2\pi \frac{r_c^2}{l_0^2} \sin\frac{\theta}{2} \tag{B.4}$$

[b]This regimen is referred to as gravity regime

where the well-known formula of meniscus height (45) was invoked:

$$h = 2l_0 \sin\frac{\theta}{2} \tag{B.5}$$

As shown in Fig. B.2, sessile drops behave as spherical drops (Eq. B.1) when the contact radius is lower than the capillary length ($r_c/l_0 \leq 1$). Instead, drops are considered as "pancakes" (Eq. B.4) when the contact radius is much greater than the capillary length ($r_c/l_0 \gg 1$). Otherwise, Eq. B.3 applies.

Bibliography

(1) *Handbook of Industrial Drying*; Mujumdar, A. S., Ed.; CRC Press, 2006; Vol. 125, p 1286.

(2) Stannard, A. Dewetting-mediated pattern formation in nanoparticle assemblies. *J. Phys.: Condens. Matter* **2011**, *23*, 083001.

(3) Sommer, A. P.; Ben-Moshe, M.; Magdassi, S. Size-Discriminative Self-Assembly of Nanospheres in Evaporating Drops. *J. Phys. Chem. B* **2004**, *108*, 8–10.

(4) Trantum, J. R.; Wright, D. W.; Haselton, F. R. Biomarker-Mediated Disruption of Coffee-Ring Formation as a Low Resource Diagnostic Indicator. *Langmuir* **2012**, *28*, 2187–2193.

(5) Deegan, R. D.; Bakajin, O.; Dupont, T. F.; Huber, G.; Nagel, S. R.; Witten, T. A. Capillary flow as the cause of ring stains from dried liquid drops. *Nature* **1997**, *389*, 827–829.

(6) Deegan, R. D.; Bakajin, O.; Dupont, T. F.; Huber, G.; Nagel, S. R.; Witten, T. A. Contact line deposits in an evaporating drop. *Phys. Rev. E* **2000**, *62*, 756–765.

(7) Deegan, R. D. Pattern formation in drying drops. *Phys. Rev. E* **2000**, *61*, 475–485.

(8) Ludwig, I.; Schabel, W.; Kind, M.; Castaing, J.-C.; Ferlin, P. Drying and film formation of industrial waterborne latices. *AIChE Journal* **2007**, *53*, 549–560.

(9) Derby, B. Inkjet Printing of Functional and Structural Materials: Property Requirements, Feature Stability, and Resolution. *Annu. Rev. Mater. Sci.* **2010**, *40*, 395–414.

(10) Biswas, S.; Gawande, S.; Bromberg, V.; Sun, Y. Effects of Particle Size and Substrate Surface Properties on Deposition Dynamics of Inkjet-Printed Colloidal Drops for Printable Photovoltaics Fabrication. *J. Sol. Energ. Eng.* **2010**, *132*, 021010–7.

(11) Nellimoottil, T. T.; Rao, P. N.; Ghosh, S. S.; Chattopadhyay, A. Evaporation-Induced Patterns from Droplets Containing Motile and Nonmotile Bacteria. *Langmuir* **2007**, *23*, 8655–8658.

(12) Baughman, K. F.; Maier, R. M.; Norris, T. A.; Beam, B. M.; Mudalige, A.; Pemberton, J. E.; Curry, J. E. Evaporative Deposition Patterns of Bacteria from a Sessile Drop: Effect of Changes in Surface Wettability Due to Exposure to a Laboratory Atmosphere. *Langmuir* **2010**, *26*, 7293–7298.

(13) Abramchuk, S. S.; Khokhlov, A. R.; Iwataki, T.; Oana, H.; Yoshikawa, K. Direct observation of DNA molecules in a convection flow of a drying droplet. *Europhys. Lett.* **2001**, *55*, 294–300.

(14) Smalyukh, I. I.; Zribi, O. V.; Butler, J. C.; Lavrentovich, O. D.; Wong, G. C. L. Structure and dynamics of liquid crystalline pattern formation in drying droplets of DNA. *Phys. Rev. Lett.* **2006**, *96*, 177801–4.

(15) Kim, J.-H.; Ahn, S. I.; Kim, J. H.; Zin, W.-C. Evaporation of Water Droplets on Polymer Surfaces. *Langmuir* **2007**, *23*, 6163–6169.

(16) Méndez-Vilas, A.; Jódar-Reyes, A.; Díaz, J.; González-Martín, M. Nanoscale aggregation phenomena at the contact line of air-drying pure water droplets on silicon revealed by atomic force microscopy. *Curr. Appl Phys.* **2009**, *9*, 48–58.

(17) Yakhno, T.; Kazakov, V.; Sanina, O.; Sanin, A.; Yakhno, V. Drops of biological fluids drying on a hard substrate: Variation of the morphology, weight, temperature, and mechanical properties. *Technical Physics* **2010**, *55*, 929–935.

(18) Tarasevich, Y.; Pravoslavnova, D. Segregation in desiccated sessile drops of biological fluids. *Eur. Phys. J. E* **2007**, *22*, 311–314.

(19) Brutin, D.; Sobac, B.; Loquet, B.; Sampol, J. Pattern formation in drying drops of blood. *J. Fluid Mech.* **2011**, *667*, 85–95.

(20) Denkov, N. D.; Velev, O. D.; Kralchevsky, P. A.; Yoshimura, I. B. I. H.; Nagayama, K. Two-dimensional crystallization. *Nature* **1993**, *361*, 26.

(21) Fustin, C. A.; Glasser, G.; Spiess, H. W.; Jonas, U. Parameters Influencing the Templated Growth of Colloidal Crystals on Chemically Patterned Surfaces. *Langmuir* **2004**, *20*, 9114–9123.

(22) Vyawahare, S.; Craig, K. M.; Scherer, A. Patterning Lines by Capillary Flows. *Nano Lett.* **2006**, *6*, 271–276.

(23) Kuncicky, D. M.; Bose, K.; Costa, K. D.; Velev, O. D. Sessile droplet templating of miniature porous hemispheres from colloid crystals. *Chem. Mater.* **2007**, *19*, 141–143.

(24) Kuncicky, D. M.; Velev, O. D. Surface-guided templating of particle assemblies inside drying sessile Droplets. *Langmuir* **2008**, *24*, 1371–1380.

(25) Rabani, E.; Reichman, D. R.; Geissler, P. L.; Brus, L. E. Drying-mediated self-assembly of nanoparticles. *Nature* **2003**, *426*, 271–274.

(26) Bigioni, T. P.; Lin, X.-M.; Nguyen, T. T.; Corwin, E. I.; Witten, T. A.; Jaeger, H. M. Kinetically driven self assembly of highly ordered nanoparticle monolayers. *Nature Materials* **2006**, *5*, 265–270.

(27) Vancea, I.; Thiele, U.; Pauliac-Vaujour, E.; Stannard, A.; Martin, C. P.; Blunt, M. O.; Moriarty, P. J. Front instabilities in evaporatively dewetting nanofluids. *Phys. Rev. E* **2008**, *78*, 041601.

(28) Marín, A. G.; Gelderblom, H.; Lohse, D.; Snoeijer, J. H. Order-to-Disorder Transition in Ring-Shaped Colloidal Stains. *Phys. Rev. Lett.* **2011**, *107*, 085502–4.

(29) Marin, A. G.; Gelderblom, H.; Lohse, D.; Snoeijer, J. H. Rush-hour in evaporating coffee drops. *Phys. Fluids* **2011**, *23*, 091111–1.

(30) Hu, H.; Larson, R. G. Marangoni Effect Reverses Coffee-Ring Depositions. *J. Phys. Chem. B* **2006**, *110*, 7090–7094.

(31) Majumder, M.; Rendall, C. S.; Eukel, J. A.; Wang, J. Y. L.; Behabtu, N.; Pint, C. L.; Liu, T.-Y.; Orbaek, A. W.; Mirri, F.; Nam, J.; Barron, A. R.; Hauge, R. H.; Schmidt, H. K.; Pasquali, M. Overcoming the Coffee-Stain Effect by Compositional Marangoni-Flow-Assisted Drop-Drying. *J. Phys. Chem. B* **2012**, *116*, 6536–6542.

(32) Yunker, P. J.; Still, T.; Lohr, M. A.; Yodh, A. G. Suppression of the coffee-ring effect by shape-dependent capillary interactions. *Nature* **2011**, *476*, 308–311.

(33) Eral, H. B.; Augustine, D. M.; Duits, M. H. G.; Mugele, F. Suppressing the coffee stain effect: How to control colloidal self-assembly in evaporating drops using electrowetting. *Soft Matter* **2011**, *7*, 4954–4958.

(34) Weon, B. M.; Je, J. H. Capillary force repels coffee-ring effect. *Phys. Rev. E* **2010**, *82*, 015305–4.

(35) Li, H.; Fowler, N.; Struck, C.; Sivasankar, S. Flow triggered by instabilities at the contact line of a drop containing nanoparticles. *Soft Matter* **2011**, *7*, 5116–5119.

(36) Whitehill, J.; Neild, A.; Ng, T. W.; Stokes, M. Collection of suspended particles in a drop using low frequency vibration. *Appl. Phys. Lett.* **2010**, *96*, 053501–3.

(37) Bhardwaj, R.; Fang, X.; Somasundaran, D., Ponisseriland Attinger Self-Assembly of Colloidal Particles from Evaporating Droplets: Role of DLVO Interactions and Proposition of a Phase Diagram. *Langmuir* **2010**, *26*, 7833–7842.

(38) Byun, M.; Wang, J.; Lin, Z. Massively ordered microstructures composed of magnetic nanoparticles. *J. Phys.: Condens. Matter* **2009**, *21*, 264014–6.

(39) Burnett, H.; Shedd, T.; Nellis, G.; El-Morsi, M.; Engelstad, R.; Garoff, S.; Varanasi, K. Control of the receding meniscus in immersion lithography. *J. Vac. Sci. Technol. B* **2005**, *23*, 2611 –2616.

(40) Winkels, K.; Peters, I.; Evangelista, F.; Riepen, M.; Daerr, A.; Limat, L.; Snoeijer, J. Receding contact lines: From sliding drops to immersion lithography. *Eur. Phys. J. Special Topics* **2011**, *192*, 195–205.

(41) Dimitrov, A. S.; Nagayama, K. Steady-state unidirectional convective assembling of fine particles into two-dimensional arrays. *Chem. Phys. Lett.* **1995**, *243*, 462–468.

(42) Ghosh, M.; Fan, F.; Stebe, K. J. Spontaneous Pattern Formation by Dip Coating of Colloidal Suspensions on Homogeneous Surfaces. *Langmuir* **2007**, *23*, 2180–2183.

(43) Rio, E.; Daerr, A.; Lequeux, F.; Limat, L. Moving contact lines of a colloidal suspension in the presence of drying. *Langmuir* **2006**, *22*, 3186–3191.

(44) Bodiguel, H.; Doumenc, F.; Guerrier, B. Stick-Slip Patterning at Low Capillary Numbers for an Evaporating Colloidal Suspension. *Langmuir* **2010**, *26*, 10758–10763.

(45) Adamson, A. W. *Physical Chemistry of Surfaces*, 5th ed.; John Wiley & Sons, Inc., 1990.

(46) de Gennes, P.-G.; Brochard-Wyart, F.; Quéré, D. *Capillarity and Wetting Phenomena. Drops, Bubbles, Pearls, Waves*; Springer, 2004.

(47) Marmur, A. From hygrophilic to superhygrophobic: Theoretical conditions for making high-contact-angle surfaces from low-contact-angle materials. *Langmuir* **2008**, *24*, 7573–7579.

(48) Vogler, E. A. In *Water in Biomaterials Science*; John Wiley, 2001; Chapter 6, pp 149–182.

(49) Gaydos, J.; Boruvka, L.; Rotenberg, Y.; Chen, P.; Neumann, A. W. In *The Generalized Theory of Capillarity*; Marcel Dekker, Inc.: 270 Madison Avenue, New York, NW 10016, 1996; Chapter 1, pp 1–52.

(50) Young, T. An Essay on the Cohesion of Fluids. *Phil. Trans. R. Soc.* **1805**, *95*, 65–87.

(51) Rusanov, A. I. Problems of surface thermodynamics. *Pure & App. Chem.* **1992**, *64*, 111–124.

(52) Roura, P.; Fort, J. Local thermodynamic derivation of Young's equation. *J. Colloid Interface Sci.* **2004**, *272*, 420–429.

(53) Eustathopolous, N.; Nicholas, M.; Drevet, B. In *Fundamental Equations of Wetting*; Elsevier Science: Oxford, 1999; Chapter 1, pp 16–17.

(54) Edgeworth, R.; Dalton, B. J.; Parnell, T. The pitch drop experiment. *European Journal of Physics* **1984**, *5*, 198.

(55) Decker, E. L.; Frank, B.; Suo, Y.; Garoff, S. Physics of contact angle measurement. *Colloids Surf., A* **1999**, *156*, 177–189.

(56) Marmur, A. Solid-Surface Characterization by Wetting. *Annu. Rev. Mater. Sci.* **2009**, *39*, 473–489.

(57) Montes-Ruiz-Cabello, F. J.; Kusumaatmaja, H.; Rodriguez-Valverde, M. A.; Yeomans, J. M.; Cabrerizo-Vilchez, M. Modeling the Corrugation of the Three-Phase Contact Line Perpendicular to a Chemically Striped Substrate. *Langmuir* **2009**, *25*, 8357–8361.

(58) Rodriguez-Valverde, M. A.; Montes-Ruiz-Cabello, F. J.; Cabrerizo-Vilchez, M. A. Wetting on axially-patterned heterogeneous surfaces. *Adv. Colloid Interface Sci.* **2008**, *138*, 84–100.

(59) Neumann, A. W.; Good, R. J. In *Techniques of Measuring Contact Angles*; Plenum Press: New York, 1997; Vol. 11, pp 31–91.

(60) Johnson, R.; Dettre, R. Contact Angle Hysteresis. Study of an Idealized Heterogeneous Surface. *J. Phys. Chem.* **1964**, *68*, 1744–1750.

(61) Huh, C.; Mason, S. Effects of Surface-Roughness on Wetting (Theoretical). *J. Colloid Interface Sci.* **1977**, *60*, 11–38.

(62) Joanny, J. F.; de Gennes, P.-G. A model for contact-angle hysteresis. *J. Chem. Phys.* **1984**, *81*, 552–562.

(63) Nadkarni, G.; Garoff, S. An investigation of microscopic aspects of contact-angle hysteresis pinning of the contact line on a single defect. *Europhys. Lett.* **1992**, *20*, 523–528.

(64) Drelich, J. Static contact angles for liquids at heterogeneous rigid solid surfaces. *Polish. J. Chem.* **1997**, *71*, 525–549.

(65) Rangwalla, H.; Schwab, A. D.; Yurdumakan, B.; Yablon, D. G.; Yeganeh, M. S.; Dhinojwala, A. Molecular structure of an alkyl-side-chain polymer-water interface: Origins of contact angle hysteresis. *Langmuir* **2004**, *20*, 8625–8633.

(66) Neumann, A. W.; Good, R. J. Thermodynamics of contact angles. I. Heterogeneous solid surfaces. *J. Colloid Interface Sci.* **1972**, *38*, 341–358.

(67) Eick, J. D.; Good, R. J.; Neumann, A. W. Thermodynamics of contact angles. II. Rough solid surfaces. *J. Colloid Interface Sci.* **1975**, *53*, 235–238.

(68) Schwartz, L.; Garoff, S. Contact-angle hysteresis on heterogeneous surfaces. *Langmuir* **1985**, *1*, 219–230.

(69) Marmur, A. Thermodynamic aspects of contact angle hysteresis. *Adv. Colloid Interface Sci.* **1994**, *50*, 121.

(70) Rodriguez-Valverde, M. A.; Ruiz-Cabello, F. J. M.; Gea-Jodar, P. M.; Kamusewitz, H.; Cabrerizo-Vilchez, M. A. A new model to estimate the Young contact angle from contact angle hysteresis measurements. *Colloids Surf., A* **2010**, *365*, 21–27.

(71) Shuttleworth, R.; Bailey, G. L. J. The Spreading of a Liquid over a Rough Solid. *Discuss. Faraday Soc.* **1948**, *3*, 16–22.

(72) Marmur, A. Soft contact: Measurement and interpretation of contact angles. *Soft Matter* **2006**, *2*, 12–17.

(73) Kwok, D.; Gietzelt, T.; Grundke, K.; Jacobasch, H.; Neumann, A. Contact angle measurements and contact angle interpretation .1. Contact angle measurements by axisymmetric drop shape analysis and a goniometer sessile drop technique. *Langmuir* **1997**, *13*, 2880–2894.

(74) Krishnan, A.; Liu, Y. H.; Cha, P.; Woodward, R.; Allara, D.; Vogler, E. A. An evaluation of methods for contact angle measurement. *Colloids Surf., B* **2005**, *43*, 95–98.

(75) Bormashenko, E.; Bormashenko, Y.; Whyman, G.; Pogreb, R.; Musin, A.; Jager, R.; Barkay, Z. Contact Angle Hysteresis on Polymer Substrates Established with Various Experimental Techniques, Its Interpretation, and Quantitative Characterization. *Langmuir* **2008**, *24*, 4020–4025.

(76) Rodriguez-Valverde, M. A.; Montes Ruiz-Cabello, F. J.; Cabrerizo-Vilchez, M. A. A new method for evaluating the most-stable contact angle using mechanical vibration. *Soft Matter* **2011**, *7*, 53–56.

(77) Ruiz-Cabello, F. J. M.; Rodriguez-Valverde, M. A.; Cabrerizo-Vilchez, M. A new method for evaluating the most stable contact angle using tilting plate experiments. *Soft Matter* **2011**, *7*, 10457–10461.

(78) *Handbook of Surface and Colloid Chemistry*; Birdi, K., Ed.; CRC Press: LLC 2000 Corporate Blvd., N.W., Boca Raton, Florida 33431, 1997.

(79) Cwikel, D.; Zhao, Q.; Liu, C.; Su, X.; Marmur, A. Comparing Contact Angle Measurements and Surface Tension Assessments of Solid Surfaces. *Langmuir* **2010**, *26*, 15289–15294.

(80) Erbil, H. Y.; McHale, G.; Rowan, S. M.; Newton, M. I. Determination of the Receding Contact Angle of Sessile Drops on Polymer Surfaces by Evaporation. *Langmuir* **1999**, *15*, 7378–7385.

(81) Mognetti, B. M.; Yeomans, J. M. Modeling Receding Contact Lines on Superhydrophobic Surfaces. *Langmuir* **2010**, *26*, 18162–18168.

(82) Chibowski, E. Apparent Surface Free Energy of Superhydrophobic Surfaces. *J. Adhes. Sci. Technol.* **2011**, *25*, 1323–1336.

(83) Meuler, A. J.; Smith, J. D.; Varanasi, K. K.; Mabry, J. M.; McKinley, G. H.; Cohen, R. E. Relationships between Water Wettability and Ice Adhesion. *ACS Applied Materials and Interfaces* **2010**, *2*, 3100–3110.

(84) Brugnara, M.; Degasperi, E.; Della-Volpe, C.; Maniglio, D.; Penati, A.; Siboni, S.; Toniolo, L.; Poli, T.; Invernizzi, S.; Castelvetro, V. The application of the contact angle in monument protection: new materials and methods. *Colloids Surf., A* **2004**, *241*, 299–312.

(85) Strobel, M.; Lyons, C. S. An Essay on Contact Angle Measurements. *Plasma Process. Polym.* **2011**, *8*, 8–13.

(86) Erbil, H. Y. In *Surface Chemistry of Solid and Liquid Interfaces*; Wiley-Blackwell, 2006; Chapter 9, pp 308–337.

(87) Kietzig, A.-M. Comments on 'An Essay on Contact Angle Measurements'. An Illustration of the Respective Influence of Droplet Deposition and Measurement Parameters. *Plasma Process. Polym.* **2011**, *8*, 1003–1009.

(88) Pierce, E.; Carmona, F.; Amirfazli, A. Understanding of sliding and contact angle results in tilted plateexperiments. *Colloids Surf., A* **2008**, *323*, 73–82.

(89) Brutin, D.; Zhu, Z.; Rahli, O.; Xie, J.; Liu, Q.; Tadrist, L. Sessile Drop in Microgravity: Creation, Contact Angle and Interface. *Microgravity Sci. Tech.* **2009**, *21*, 67–76.

(90) Blake, T. D. The physics of moving wetting lines. *J. Colloid Interface Sci.* **2006**, *299*, 1–13.

(91) Kwok, D.; Lin, R.; Mui, M.; Neumann, A. Low-rate dynamic and static contact angles and the determination of solid surface tensions. *Colloids Surf., A* **1996**, *116*, 63–77.

(92) Long, J.; Chen, P. On the role of energy barriers in determining contact angle hysteresis. *Adv. Colloid Interface Sci.* **2006**, *127*, 55–66.

(93) Ruiz-Cabello, F. J. M.; Rodriguez-Valverde, M. A.; Cabrerizo-Vilchez, M. A. Contact Angle Hysteresis on Polymer Surfaces: An Experimental Study. *J. Adhes. Sci. Technol.* **2011**, *25*, 2039–2049.

(94) Lee, S. H.; Ruckenstein, E. Surface restructuring of polymers. *J. Colloid Interface Sci.* **1987**, *120*, 529–536.

(95) Ramos, S.; Charlaix, E.; Benyagoub, A. Contact angle hysteresis on nano-structured surfaces. *Surf. Sci.* **2003**, *540*, 355–362.

(96) Ramos, S.; Tanguy, A. Pinning-depinning of the contact line on nanorough surfaces. *Eur. Phys. J. E* **2006**, *19*, 433–440.

(97) Langbein, D. In *Canthotaxis/Wetting Barriers/Pinning Lines*; Springer, 2002; Vol. 178, Chapter 7, pp 149–177.

(98) Marmur, A. Contact-angle hysteresis on heterogeneous smooth surfaces: Theoretical comparison of the captive bubble and drop methods. *Colloids Surf., A* **1998**, *136*, 209–215.

(99) Zhang, X.; Mi, Y. Dynamics of a Stick-Jump Contact Line of Water Drops on a Strip Surface. *Langmuir* **2009**, *25*, 3212–3218.

(100) Ruiz-Cabello, F. J. M.; Rodriguez-Valverde, M. A.; Marmur, A.; Cabrerizo-Vilchez, M. A. Comparison of Sessile Drop and Captive Bubble Methods on Rough Homogeneous Surfaces: A Numerical Study. *Langmuir* **2011**, *27*, 9638–9643.

(101) Good, R. A thermodynamic derivation of Wenzel's modification of Young's equation for contact angles together with a theory of hysteresis. *J. Am. Chem. Soc.* **1952**, *74*, 5041–5042.

(102) Bourgks-Monnier, C.; Shanahan, M. E. R. Influence of Evaporation on Contact Angle. *Langmuir* **1995**, *11*, 2820–2829.

(103) Hegseth, J. J.; Rashidnia, N.; Chai, A. Natural convection in droplet evaporation. *Phys. Rev. E* **1996**, *54*, 1640–1644.

(104) Erbil, H. Y. Evaporation of pure liquid sessile and spherical suspended drops: A review. *Adv. Colloid Interface Sci.* **2012**, *170*, 67–86.

(105) Siboni, S. Determination of the Kelvin equation in the presence of an arbitrary gravitational/inertial field. *Am. J. Phys.* **2006**, *74*, 565–568.

(106) Butt, H.-J.; Golovko, D. S.; Bonaccurso, E. On the Derivation of Young's Equation for Sessile Drops: Nonequilibrium Effects Due to Evaporation. *J. Phys. Chem. B* **2007**, *111*, 5277–5283.

(107) Sokuler, M.; Auernhammer, G. K.; Liu, C. J.; Bonaccurso, E.; Butt, H.-J. Dynamics of condensation and evaporation: Effect of inter-drop spacing. *Europhys. Lett.* **2010**, *89*, 36004.

(108) Tavana, H.; Neumann, A. On the question of rate-dependence of contact angles. *Colloids Surf., A* **2006**, *282*, 256–262.

(109) Oliver, J. F.; Huh, C.; Mason, S. G. Resistance to spreading of liquids by sharp edges. *J. Colloid Interface Sci.* **1977**, *59*, 568–581.

(110) Amirfazli, A.; Neumann, A. Status of the three-phase line tension: a review. *Adv. Colloid Interface Sci.* **2004**, *3*, 110.

(111) Kim, J.-H.; Ahn, S. I.; Kim, J. H.; Kim, J. S.; Cho, K.; Jung, J. C.; Chang, T.; Ree, M.; Zin, W.-C. Evaporation of sessile droplets of dilute aqueous solutions containing sodium n-alkylates from polymer surfaces: Influences of alkyl length and concentration of solute. *Langmuir* **2008**, *24*, 11442–11450.

(112) Lam, C. N. C.; Wu, R.; Li, D.; Hair, M. L.; Neumann, A. W. Study of the advancing and receding contact angles: Liquid sorption as a cause of contact angle hysteresis. *Adv. Colloid Interface Sci.* **2002**, *96*, 169–191.

(113) Lam, C. N. C.; Kim, N.; Hui, D.; Kwok, D. Y.; Hair, M. L.; Neumann, A. W. The effect of liquid properties to contact angle hysteresis. *Colloids Surf., A* **2001**, *189*, 265–278.

(114) Erickson, D.; Blackmore, B.; Li, D. An energy balance approach to modeling the hydrodynamically driven spreading of a liquid drop. *Colloids Surf., A* **2001**, *182*, 109–122.

(115) Dussan, E. B. On the Spreading of Liquids on Solid Surfaces: Static and Dynamic Contact Lines. *Annu. Rev. Fluid Mech.* **1979**, *11*, 371–400.

(116) Blake, T. D.; Ruschak, K. J. A maximum speed of wetting. *Nature* **1979**, *282*, 489–491.

(117) Rupp, F.; Scheideler, L.; Geis-Gerstorfer, J. Effect of Heterogenic Surfaces on Contact Angle Hysteresis: Dynamic Contact Angle Analysis in Material Sciences. *Chem. Eng. Technol.* **2002**, *25*, 877–882.

(118) Rupp, F.; Scheideler, L.; Olshanska, N.; de Wild, M.; Wieland, M.; Geis-Gerstorfer, J. Enhancing surface free energy and hydrophilicity through chemical modification of microstructured titanium implant surfaces. *J. Biomed. Mater. Res. A* **2006**, *76A*, 323–334.

(119) Bhardwaj, R.; Fang, X.; Attinger, D. Pattern formation during the evaporation of a colloidal nanoliter drop: a numerical and experimental study. *New J. Phys.* **2009**, *11*, 075020–33.

(120) Park, J.; Moon, J. Control of Colloidal Particle Deposit Patterns within Picoliter Droplets Ejected by Ink-Jet Printing. *Langmuir* **2006**, *22*, 3506–3513.

(121) Keseroglu, K.; ulha, M. Assembly of nanoparticles at the contact line of a drying droplet under the influence of a dipped tip. *J. Colloid Interface Sci.* **2011**, *360*, 8–14.

(122) Huang, M. H.; Lin, P.-H. Shape-Controlled Synthesis of Polyhedral Nanocrystals and Their Facet-Dependent Properties. *Adv. Funct. Mater.* **2012**, *22*, 14–24.

(123) Dushkin, C.; Yoshimura, H.; Nagayama, K. NUCLEATION AND GROWTH OF 2-DIMENSIONAL COLLOIDAL CRYSTALS. *Chem. Phys. Lett.* **1993**, *204*, 455–460.

(124) Sommer, A. P. Suffocation of Nerve Fibers by Living Nanovesicles: A Model Simulation. *J. Proteome Res.* **2004**, *3*, 667–669.

(125) Truskett, V. N.; Stebe, K. J. Influence of Surfactants on an Evaporating Drop: Fluorescence Images and Particle Deposition Patterns. *Langmuir* **2003**, *19*, 8271–8279.

(126) Yan, Q.; Gao, L.; Sharma, V.; Chiang, Y.-M.; Wong, C. C. Particle and Substrate Charge Effects on Colloidal Self-Assembly in a Sessile Drop. *Langmuir* **2008**, *24*, 11518–11522.

(127) Ristenpart, W. D.; Kim, P. G.; Domingues, C.; Wan, J.; Stone, H. A. Influence of Substrate Conductivity on Circulation Reversal in Evaporating Drops. *Phys. Rev. Lett.* **2007**, *99*, 234502–4.

(128) Denkov, N. D.; Kralchevsky, P. A.; Ivanov, I. B. Lateral capillary forces and two-dimensional arrays of colloid particles and protein molecules. *J. Disper. Sci. Technol.* **1997**, *18*, 577–591.

(129) Gelderblom, H.; Marín, A. G.; Nair, H.; van Houselt, A.; Lefferts, L.; Snoeijer, J. H.; Lohse, D. How water droplets evaporate on a superhydrophobic substrate. *Phys. Rev. E* **2011**, *83*, 026306–6.

(130) Perelaer, J.; Smith, P. J.; Hendriks, C. E.; van den Berg, A. M. J.; Schubert, U. S. The preferential deposition of silica micro-particles at the boundary of inkjet printed droplets. *Soft Matter* **2008**, *4*, 1072–1078.

(131) Chhasatia, V. H.; Sun, Y. Interaction of bi-dispersed particles with contact line in an evaporating colloidal drop. *Soft Matter* **2011**, *7*, 10135–10143.

(132) Das, S.; Chakraborty, S.; Mitra, S. K. Ring stains in the presence of electrokinetic interactions. *Phys. Rev. E* **2012**, *85*, 046311–8.

(133) Jung, J.-y.; Kim, Y. W.; Yoo, J. Y.; Koo, J.; Kang, Y. T. Forces Acting on a Single Particle in an Evaporating Sessile Droplet on a Hydrophilic Surface. *Anal. Chem.* **2010**, *82*, 784–788.

(134) Chen, Y. L.; Helm, C. A.; Israelachvili, J. N. Molecular Mechanisms Associated with Adhesion and Contact Angle Hysteresis of Monolayer Surfaces. *J. Phys. Chem.* **1991**, *95*, 10736–10747.

(135) Kobayashi, M.; Nanaumi, H.; Muto, Y. Initial deposition rate of latex particles in the packed bed of zirconia beads. *Colloids Surf., A* **2009**, *347*, 2–7.

(136) Wong, T.-S.; Chen, T.-H.; Shen, X.; Ho, C.-M. Nanochromatography Driven by the Coffee Ring Effect. *Anal. Chem.* **2011**, *83*, 1871–1873.

(137) Hodges, C. S.; Ding, Y.; Biggs, S. The influence of nanoparticle shape on the drying of colloidal suspensions. *J. Colloid Interface Sci.* **2010**, *352*, 99 – 106.

(138) Sandu, I.; Fleaca, C. T. The influence of gravity on the distribution of the deposit formed onto a substrate by sessile, hanging, and sandwiched hanging drop evaporation. *J. Colloid Interface Sci.* **2011**, *358*, 621 – 625.

(139) Sangani, A. S.; Lu, C.; Su, K.; Schwarz, J. A. Capillary force on particles near a drop edge resting on a substrate and a criterion for contact line pinning. *Phys. Rev. E* **2009**, *80*, 011603–15.

(140) Shmuylovich, L.; Shen, A. Q.; ; Stone, H. A. Surface morphology of drying latex films: Multiple ring formation. *Langmuir* **2002**, *18*, 3441–3445.

(141) Zhang, X.; Zhang, J.; Zhu, D.; Li, X.; Zhang, X.; Wang, T.; Yang, B. A Universal Approach To Fabricate Ordered Colloidal Crystals Arrays Based on Electrostatic Self-Assembly. *Langmuir* **2010**, *26*, 17936–17942.

(142) Delgado, Á. *Interfacial Electrokinetics and Electrophoresis*; Surfactant Science Series; Marcel Dekker, 2002.

(143) Mengual, O.; Meunier, G.; Cayre, I.; Puech, K.; Snabre, P. Characterisation of instability of concentrated dispersions by a new optical analyser: the TURBISCAN MA 1000. *Colloids Surf., A* **1999**, *152*, 111 – 123.

(144) Mohammadi, R.; Amirfazli, A. Contact Angle Measurement for Dispersed Microspheres Using Scanning Confocal Microscopy. *J. Dispersion Sci. Technol.* **2005**, *25*, 567–574.

(145) Cousins, B. G.; Zekonyte, J.; Doherty, P. J.; Garvey, M. J.; Williams., R. L. Manufacturing a nanometre scale surface topography with varying surface chemistry to assess the combined effect on cell behaviour. *Int. J. Nano and Biomaterials* **2008**, *1*, 320–338.

(146) Tosatti, S.; Michel, R.; Textor, M.; Spencer, N. D. Self-Assembled Monolayers of Dodecyl and Hydroxy-dodecyl Phosphates on Both Smooth and Rough Titanium and Titanium Oxide Surfaces. *Langmuir* **2002**, *18*, 3537–3548.

(147) van Zwol, P. J.; Palasantzas, G.; De Hosson, J. T. M. Influence of roughness on capillary forces between hydrophilic surfaces. *Phys. Rev. E* **2008**, *78*, 031606–6.

(148) Fischer, B. J. Particle Convection in an Evaporating Colloidal Droplet. *Langmuir* **2002**, *18*, 60–67.

(149) Vogel, N.; Weiss, C. K.; Landfester, K. From soft to hard: the generation of functional and complex colloidal monolayers for nanolithography. *Soft Matter* **2012**, *8*, 4044–4061.

(150) Nosonovsky, M. Model for solid-liquid and solid-solid friction of rough surfaces with adhesion hysteresis. *J. Chem. Phys.* **2007**, *126*, 224701–6.

(151) Tilley, J.; Lovett, D. Illustrating phase changes using graphics modelling of soap film patterns. *Phys. Educ.* **1995**, *30*, 74–79.

(152) Isenberg, C. *The Science of Soap Films and Soap Bubbles*; Dover Publications Inc.: New York, 1992.

(153) Israelachvili, J. N. *Intermolecular and Surface Forces*, 3rd ed.; Academic Press: London, 2011.

(154) Behroozi, F.; Macomber, H. K.; Dostal, J. A.; Behroozi, C. H.; Lambert, B. K. The profile of a dew drop. *Am. J. Phys.* **1996**, *64*, 1120–1125.